

Stabilities of Parallel Flow and Horizontal Convection

Liang SUN

Report of Postdoc Research

Academic Advisor Prof. Yun-Fei Fu

LSRSCE, School of Earth and Space Sciences,
University of Science and Technology of China,
November, 2007



Abstract

In the first part, the stability of two-dimensional parallel flow is discussed. A more restrictively general stability criterion for inviscid parallel flow is obtained analytically. First, a sufficient criterion for stability is found as either $-\mu_1 < \frac{U''}{U-U_s} < 0$ or $0 < \frac{U''}{U-U_s}$ in the flow, where U_s is the velocity at the inflection point, and μ_1 is the eigenvalue of Poincaré's problem. Second, this criterion is generalized to barotropic geophysical flows in the β plane. Based on the stability criteria, the necessary condition for wave-mean flow interaction is also obtained.

Then, the general stability criteria of two-dimensional inviscid rotating flow with angular velocity $\Omega(r)$ are obtained analytically. First, a necessary instability criterion for centrifugal flows is derived as $\xi'(\Omega - \Omega_s) < 0$ (or $\xi'/(\Omega - \Omega_s) < 0$) somewhere in the flow field, where ξ' is the vorticity of profile and Ω_s is the angular velocity at the inflection point $\xi' = 0$. Second, a criterion for stability is found as $-(\mu_1 + 1/r_2) < f(r) = \frac{\xi'}{\Omega - \Omega_s} < 0$, where μ_1 is an eigenvalue. The new criteria are the analogues of the criteria for parallel flows, which are special cases of Arnol'd's nonlinear criteria. Specifically, Pedley's criterion is proved to be a special case of Rayleigh's criterion. Moreover, the criteria for parallel flows can also be derived from those for the rotating flows. The analogy between rotation and stratification in inviscid flow is also addressed. These results extend the previous theorems and would intrigue future research on the mechanism of hydrodynamic instability.

Besides, the essence of shear instability is fully revealed within the linear context. The mechanism of shear instability is explored by combining the mechanisms of both the Kelvin-Helmholtz instability (K-H instability) and resonance of waves. The shear instability requires both a concentrated vortex (with speed of U_s) in the flow and resonant waves to interact with the concentrated vortex. Physically, the standing waves (with phase speed $c_r = U_s$) can interact with the concentrated vortex, so they can trigger instability via K-H instability in the flows. While the travelling waves (with $c_r \neq U_s$) have no interaction with the concentrated vortex, so that they can not trigger instability in the flows. The resonance of waves are totally within the linear context.

In consequence, the above criteria would be helpful for understanding the wave-mean flow interaction, especially the Rossby wave-mean flow interaction in barotropic flows. According to the stable criteria, the necessary condition for wave-mean flow interaction can be obtained. And why the disturbed waves can't take energy from the mean flow in the stable flow is revealed. If the flow is stable, there is no wave-mean flow interaction at all. This explains why the disturbed waves can't take energy from the mean flow in the stable flow.

In the second part, we report the numerical simulations of the partial-penetrating flow in horizontal convection within a square cavity tank at high Rayleigh numbers $10^7 < Ra < 10^{10}$. The partial-penetrating flow was first reported in the experiment by Wang and Huang (2005), which is thought of an important material to understand ocean circulation energy budget. The fast established but slowly steadied flow is simulated, where a shallow and closed circulation cell is obtained numerically.

ically as partial-penetrating flow for the first time, which is consistent with the experiment. As the partial-penetrating flow is shallow, it is seldom affected by the bottom boundary. The depth of partial-penetrating circulation satisfies minus 1/5-power law of Rayleigh number. The larger the Rayleigh number is, the shallower the partial-penetrating flow is. An objective definition of partial-penetrating is given based on this power law. Then, further investigation points out that the Prandtl number governs the partial-penetrating flows. As $Pr \geq 6$, there are always partial-penetrating flows. While $Pr \leq 4$, the flows tend to be full-penetrating.

Then, the horizontal convection at high Rayleigh number (Ra) in a rectangle cavity with aspect ratio of 1 : 10 is numerically simulated. According to the results within the regime of $10^4 < Ra < 10^{11}$, three continuous regimes are obtained: linear regime ($10^4 < Ra < 10^6$), transition regime ($10^6 < Ra < 10^8$) and 1/5-power law regime ($10^8 < Ra < 10^{11}$). For the flow strength, a 1/3-power law of Ra is fitted when Ra is not high enough ($10^7 < Ra < 10^8$). However, a 1/5-power law is obtained as Ra is high enough ($10^8 < Ra < 10^{11}$). The 1/5-power law confirms Rossby's analysis and implies that 1/3-power law of Ra for Nusselt number by Siggers et al. is over estimation.

Finally, the critical Rayleigh number for onset of the horizontal convection is also addressed. The flow is found to be unsteady at high Rayleigh numbers. There is a Hopf bifurcation of Ra from steady solutions to periodic solutions, and the critical Rayleigh number Ra_c is obtained as $Ra_c = 5.5377 \times 10^8$ for the middle plume forcing at $Pr = 1$, which is much larger than the formerly obtained value. Besides, the unstable perturbations are always generated from the central jet, which implies that the onset of instability is due to velocity shear (shear instability) other than thermally dynamics (thermal instability). Finally, Paparella and Young's (2000) second hypotheses about the destabilization of the flow is numerically proved, i.e. the middle plume forcing can lead to a destabilization of the flow.

The report was supported by the National Foundation of Natural Science (No. 40705027) and the National Science Foundation for Post-doctoral Scientists of China (No. 20070410213).

Contents

Abstract	3
1 General Stability Criteria	1
§ 1.1 Two-Dimensional Problem	1
§ 1.1.1 Introduction	1
§ 1.1.2 Stable criterion	2
§ 1.1.3 Discussion	4
§ 1.1.4 Conclusion	7
§ 1.2 Longwave Instability	7
§ 1.2.1 Introduction	7
§ 1.2.2 Model and Analysis	8
§ 1.2.3 Discussion	9
§ 1.3 Mechanism of Shear Instability	11
§ 1.3.1 Introduction	11
§ 1.3.2 Stable Criterion	12
§ 1.3.3 Physical explanation	14
§ 1.4 Rotating Flow	16
§ 1.4.1 Introduction	16
§ 1.4.2 Howard-Gupta Equation	17
§ 1.4.3 Stable Criterion	17
§ 1.4.4 Discussion	20
§ 1.5 General Barotropic Wave	21
2 Horizontal Convection	23
§ 2.1 Establishment of Horizontal Convection	23
§ 2.1.1 Introduction	23
§ 2.1.2 Model and Scheme	24
§ 2.1.3 Results	25
§ 2.2 Partial-Penetrating Flow	31

CONTENTS

§ 2.2.1 Introduction	31
§ 2.2.2 Model and Scheme	32
§ 2.2.3 Results	33
§ 2.2.4 Conclusion	39
§ 2.3 Power Laws	40
§ 2.3.1 Introduction	40
§ 2.3.2 Results	40
§ 2.3.3 Power laws	41
§ 2.3.4 Summary	42
§ 2.4 Onset of Instability	43
§ 2.4.1 Introduction	43
§ 2.4.2 Results	44
§ 2.4.3 Conclusion	48
Reference	51

List of Figures

1-1	Sketch of parallel flow.	2
1-2	Vorticity profiles within the interval $-1 \leq y \leq 1$. Profile 2 ($\xi = \cos(\pi y/2)$, dashed) is neutrally stable, while profile 1 ($\xi = \cos(y)$, solid) and profile 3 ($\xi = \cos(2y)$, dash dotted) are stable and unstable, respectively.	5
1-3	Growth rate ω_i as an function of wavenumber k , (a) for $U_1 = \tanh(1.1y)$, (b) for $U_2 = \tanh(1.3y)$, both within the interval $-1 \leq y \leq 1$	5
1-4	Diagram of stable velocity profiles.....	6
1-5	Sketch of shear instability: physical interpretation. Left parts depict the profiles of velocity $U(y)$ and vorticity $\xi(y)$, right ones depict the disturbance of vorticities. The unstable velocity profile $U(y)$ has a local maximum in vorticity $\xi(y)$ (a). If the vortices (A, B and C) disturbed from their original positions (dashed line) to new places (solid curve), they will be taken away from their original positions due to pressure difference. The stable velocity profile $U(y)$ has a local minimum in vorticity $\xi(y)$ (b). The disturbed vortices (A', B' and C') will be brought back to their original positions due to pressure difference.	15
1-6	Angular velocity Ω (solid line) and corresponding vorticity ξ (dashed line) versus r . .	20
2-1	Snapshots of the flow fields (streamfunction Ψ), with solid counter curves for $\Psi > 0$ and dashed counter lines for $\Psi < 0$	26
2-2	Snapshots of the temperature fields corresponding to these in Fig.2-1, with counter intervals being 0.1.....	26
2-3	Snapshots of the flow fields (streamfunction Ψ), with solid counter curves for $\Psi > 0$ and dashed counter lines for $\Psi < 0$. The counter intervals are 8 and -1 for $\Psi > 0$ and $\Psi < 0$, respectively.	27
2-4	Snapshots of the temperature fields corresponding to these in Fig.2-3, with counter intervals being 0.1.....	28
2-5	Snapshots of the flow fields (streamfunction Ψ) for $Pr = 8$ and $Ra = 5 \times 10^8$, with solid counter curves for $\Psi > 0$ and dashed counter lines for $\Psi < 0$. The counter intervals are 10 for $\Psi > 0$	29
2-6	Snapshots of the temperature fields corresponding to these in Fig.2-5.....	29
2-7	The time evolution of the flow field for total kinetic energy E_k (a) and maximum flow Ψ_{\max} (b) at $Pr = 8$ and $Ra = 5 \times 10^8$	30

LIST OF FIGURES

2-8	The flow streamfunction Ψ_{\max} (a) and the heat flux Nu (b) vs. Rayleigh number, where $Ra_p = RaPr^{1/2}$ in (a).	31
2-9	(a) The maximum of streamfunction Ψ_{\max} vs time t for $Ra = 2 \times 10^8$. The solid, dashed and dash-dotted curves are solutions with $N = 40$, $N = 64$ and $N = 80$, respectively. (b) The stable and unstable regime on the plot of Rayleigh number Ra vs N .	34
2-10	The flow fields (streamfunction Ψ) at four different time steps: $t = 0.5$ (a), $t = 1.0$ (b), $t = 1.5$ (c) and $t = 2.5$ (d) at $Pr=8$ and $Ra = 5 \times 10^8$, solid curves for clockwise flow ($\Psi > 0$) and dashed curves for anticlockwise flow ($\Psi < 0$), respectively. The partial-penetrating cells ($\Psi > 20$) are shadowed and the counter intervals are 10 for $\Psi > 0$ in each figures.	35
2-11	The flow fields (streamfunction Ψ) near the forcing surface of three respective aspect ratios: $A = 1$ (a), $A = 0.5$ (b) and $A = 0.25$ (c) at $Pr=8$ and $Ra = 5 \times 10^8$. The partial-penetrating cells are shadowed and the counter intervals are 10 in each figures.	37
2-12	The flow fields (streamfunction Ψ) for full-penetrating flow at $Pr=1$ and $Ra = 5 \times 10^8$. The counter interval is 5, and $\Psi > 35$ is shadowed.	38
2-13	The flow fields (streamfunction Ψ) near the forcing surface of three respective aspect ratios: $A = 1$ (a), $A = 0.5$ (b) and $A = 0.25$ (c) at $Pr=1$ and $Ra = 5 \times 10^8$. The streamfunction $\Psi > 35$ are shadowed and the counter intervals are 5 in each figures.	38
2-14	D_c vs. Ra . The solid, dashed and dash dotted lines are power laws of Ra respectively for D_c at $Pr = 6$, $Pr = 4$ and $Pr = 2$.	39
2-15	The flow stream function (a) and temperature field (b) of $Ra = 10^7$. It is steady and stable and symmetric with middle plume forcing, solid and dashed curves for positive and negative values, respectively.	40
2-16	The flow stream function (a) and temperature field (b) of $Ra = 10^{10}$. It is steady and stable and symmetric with middle plume forcing, solid and dashed curves for positive and negative values, respectively.	41
2-17	The flow stream function Ψ_{max} (a) and heat flux (b) vs. Ra .	42
2-18	The flow stream function (a) and temperature field (b) of $Ra = 5 \times 10^8$. It is steady and stable and symmetric with middle plume forcing, solid and dashed curves for positive and negative values, respectively.	45
2-19	The horizontal (a) and vertical (b) velocity fields of $Ra = 5 \times 10^8$. It is steady and stable and symmetric with middle plume forcing, solid and dashed curves for positive and negative values, respectively.	45
2-20	Growth rate σ_r (solid) and σ_i (dashed) vs. Ra , respectively.	46
2-21	The perturbational vorticity fields at $t = 0$ (a), $t = T/8$ (b), $t = T/4$ (c) and $t = 3T/8$ of $Ra = 5.54 \times 10^8$, solid and dashed curves for positive and negative values, respectively.	47
2-22	The perturbational vorticity fields at $t = T/2$ (a), $t = 5T/8$ (b), $t = 6T/8$ (c) and $t = 7T/8$ of $Ra = 5.54 \times 10^8$, solid and dashed curves for positive and negative values, respectively.	47
2-23	The vorticity of $Ra = 5.54 \times 10^8$ with vertical velocity w (shadowed as $w > 1800$), solid and dashed curves for positive and negative values, respectively.	48

LIST OF FIGURES

2-24 The flow field (a) and temperature field (b) of $Ra = 5 \times 10^8$, which are steady and stable and symmetric with sidewall plume forcing. 48

LIST OF FIGURES

Chapter 1 1

General Stability Criteria

§ 1.1 Two-Dimensional Problem

§ 1.1.1 Introduction

The instability due to shear in the flow is one of the fundamental and the most attracting problems in many fields, such as fluid dynamics, astrophysical fluid dynamics, oceanography, meteorology, etc. More generally, shear instability is also referred as barotropic instability in geophysical flows, where the gravitational and buoyancy effects are ignored. Shear instability has been intensively investigated, which is to the greatly helpful understanding of other instability mechanisms in complex shear flows. Rayleigh investigated the growth of linear disturbances by means of normal mode expansion, which leads to Rayleigh's equation [1]. Using this equation, Rayleigh first proved a necessary criterion for instability, i.e., Inflection Point Theorem, which is also called Rayleigh-Kuo theorem [e.g. 2] for Kuo's generalization to barotropic geophysical flows in the β plane [3]. Then, Fjørtoft found a stronger necessary criterion for instability [4]. Besides, Tollmien gave a heuristic result that the criteria are also sufficient for instability if the velocity profiles are the symmetrical or monotonic [5]. These criteria are well known and have been widely used in various applications [e.g. 2, 6, 7].

On the other hand, Arnol'd considered the shear instability in a totally different way [8, 9, 10]. He studied the conservation law of the inviscid flow via Euler's equations and found two nonlinear stability theorems by means of variational principle. Arnol'd's first stability theorem corresponds to Fjørtoft's criterion [6, 11]. However, Arnol'd's second nonlinear stability theorem, has no such corresponding linear criterion. Though Arnol'd's second nonlinear theorem is more useful in the geophysical flows [11], is seldom known by the scientists in other fields. Dowling suggested that Arnol'd's idea should need to be added to the general fluid-dynamics curriculum [11]. Yet his suggestion has not been followed until now [e.g. 2, 6, 7, 12], since the proofs of Arnol'd's theorems are very advanced and complex in mathematics.

The aim of this section is to find the elementary proofs for Arnol'd's theorems, which could be used to teach undergraduate students. As the variational method is too advanced and complex for undergraduate students. The new proofs are obtained in a totally different way, where the linear stability problem is considered by using Rayleigh's equation.

§ 1.1.2 Stable criterion

To find the criteria, Rayleigh's equation for an inviscid parallel flow is employed [1, 2, 6, 7, 13], which is the vorticity equation of the disturbance [6, 7]. For a parallel flow with mean velocity $U(y)$ in Fig.1-1, the vorticity is conserved along pathlines. The amplitude of disturbed flow streamfunction, namely ϕ , satisfies

$$(\phi'' - k^2\phi) - \frac{U''}{U - c}\phi = 0, \quad (1-1)$$

where k is the nonnegative real wavenumber and $c = c_r + ic_i$ is the complex phase speed and double prime $''$ denotes d^2/dy^2 . The real part of complex phase speed c_r is the wave phase speed, and $\omega_i = kc_i$ is the growth rate of the wave. This equation is to be solved subject to homogeneous boundary conditions

$$\phi = 0 \text{ at } y = a, b. \quad (1-2)$$

There are three main categories of boundaries: (i) open channels with both a and b being finite, (ii) boundary layers with either a or b being infinite, and (iii) free shear flows with both a and b being infinite.

It is obvious that the criterion for stability is $\omega_i = 0$ ($c_i = 0$), for that the complex conjugate quantities ϕ^* and c^* are also a physical solution of Eq.(1-1) and Eq.(1-2).

Multiplying Eq.(1-1) by the complex conjugate ϕ^* and integrating over the domain $a \leq y \leq b$, we get the following equations

$$\int_a^b [(\|\phi'\|^2 + k^2\|\phi\|^2) + \frac{U''(U - c_r)}{\|U - c\|^2}\|\phi\|^2] dy = 0, \quad (1-3)$$

and

$$c_i \int_a^b \frac{U''}{\|U - c\|^2} \|\phi\|^2 dy = 0. \quad (1-4)$$

Rayleigh used only Eq.(1-4) to prove his theorem, i.e., a necessary condition for instability is $U''(y_s) = 0$, where y_s is the inflection point and $U_s = U(y_s)$ is the velocity at y_s . Fjørtoft noted that Eq.(1-3) should also be satisfied, then he obtained his necessary criterion. To find a more restrictive criterion, we shall investigate the conditions for $c_i = 0$. Unlike the former investigations, we consider this

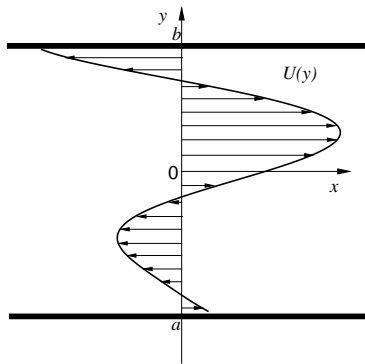


Figure 1-1: Sketch of parallel flow.

problem in a totally different way: if the velocity profile is stable ($c_i = 0$), then the hypothesis $c_i \neq 0$ should result in contradictions in some cases. Following this, some more restrictive criteria can be obtained.

To find a stronger criterion, we need to estimate the ratio of $\int_a^b \|\phi'\|^2 dy$ to $\int_a^b \|\phi\|^2 dy$. This is known as Poincaré's problem:

$$\int_a^b \|\phi'\|^2 dy = \mu \int_a^b \|\phi\|^2 dy, \quad (1-5)$$

where the eigenvalue μ is positive definite for any $\phi \neq 0$. The smallest eigenvalue value, namely μ_1 , can be estimated as $\mu_1 > (\frac{\pi}{b-a})^2$, like what Tollmien have done [5].

Then using Poincaré's relation Eq.(1-5), a new stability criterion may be found: the parallel flow is stable if $-\mu_1 < \frac{U''}{U-U_s} < 0$ everywhere.

To get this criterion, we introduce an auxiliary function $f(y) = \frac{U''}{U-U_s}$, where $f(y)$ is finite at the inflection point. We will prove the criterion by two steps. First, we will prove proposition 1: if the velocity profile is subject to $-\mu_1 < f(y) < 0$, then $c_r \neq U_s$.

Proof: Since $-\mu_1 < f(y) < 0$, then

$$-\mu_1 < \frac{U''}{U-U_s} = \frac{U''(U-U_s)}{(U-U_s)^2} \leq \frac{U''(U-U_s)}{(U-U_s)^2 + c_i^2}. \quad (1-6)$$

Substitution of $c_r = U_s$ and Eq.(1-6) into Eq.(1-3) results in

$$\int_a^b [\|\phi'\|^2 + k^2 \|\phi\|^2 + \frac{U''(U-U_s)}{\|U-c\|^2} \|\phi\|^2] dy > 0. \quad (1-7)$$

This contradicts Eq.(1-3). So proposition 1 is proved.

Then, we will prove proposition 2: if $-\mu_1 < f(y) < 0$ and $c_r \neq U_s$, there must be $c_i^2 = 0$.

Proof: If $c_i^2 \neq 0$, then multiplying Eq.(1-4) by $(c_r - U_t)/c_i$, where the arbitrary real constant U_t does not depend on y , and adding the result to Eq.(1-3), yields

$$\int_a^b [(\|\phi'\|^2 + k^2 \|\phi\|^2) + \frac{U''(U-U_t)}{\|U-c\|^2} \|\phi\|^2] dy = 0. \quad (1-8)$$

But the above Eq.(1-8) does not hold for some special U_t . For example, if $U_t = 2c_r - U_s$, then there is $(U-U_s)(U-U_t) < \|U-c\|^2$, and

$$\frac{U''(U-U_t)}{\|U-c\|^2} = f(y) \frac{(U-U_s)(U-U_t)}{\|U-c\|^2} > -\mu_1. \quad (1-9)$$

This yields

$$\int_a^b \{\|\phi'\|^2 + [k^2 + \frac{U''(U-U_t)}{\|U-c\|^2}] \|\phi\|^2\} dy > 0, \quad (1-10)$$

which also contradicts Eq.(1-8). So proposition 2 is also proved.

Using "proposition 1: if $-\mu_1 < f(y) < 0$ then $c_r \neq U_s$ " and "proposition 2: if $-\mu_1 < f(y) < 0$ and $c_r \neq U_s$ then $c_i = 0$ ", we find a stability criterion. If the velocity profile satisfies $-\mu_1 < \frac{U''}{U-U_s} < 0$ everywhere, the parallel flow is stable. Moreover, the above proof is still valid for $0 < f(y)$, which is equivalent to Fjørtoft's criterion. Thus we have the following theorem.

Theorem 1: If the velocity profile satisfies either $-\mu_1 < \frac{U''}{U-U_s} < 0$ or $0 < \frac{U''}{U-U_s}$, the flow is stable.

This criterion covers Rayleigh's and Fjørtoft's criteria. And the proofs here are very simple and easy to understand comparing to Arnol'd's proofs. As mentioned above, we have investigated the stable criterion via Rayleigh's equation, while Arnol'd [14] considered the hydrodynamic stability in a totally different way. Is there any relationship between these proofs? Two points are outlined here. First, this criterion is essentially the same as Arnol'd's second stability theorem and is more restrictive than Fjørtoft's criterion. Second, the proofs here are similar to Arnol'd's variational principle method. For the arbitrary real number U_t , which is like a Lagrange multiplier in variational principle method, plays a key role in the proofs.

§ 1.1.3 Discussion

One may note that the criterion above is something different from Fjørtoft's criterion. Why are the functions of $U''/(U-U_s)$ used in Arnol'd's theorems and present theorems, unlike $U''(U-U_s)$ in Fjørtoft's theorem? This is due to the property of Rayleigh's equation. It can be seen from Eq.(1-1) that the stability of profile $U(y)$ is not only Galilean invariant, but also independent from the the magnitude of $U(y)$ due to the linearity. So the stability of $U(y)$ is the same as that of $AU(y) + B$, where A and B are any arbitrary nonzero real numbers. As the value of $U''(U-U_s)$ is only Galilean invariant but not magnitude free, it satisfies only part of the Rayleigh's equation's properties. On the other hand the value of $U''/(U-U_s)$ satisfies both conditions, this is the reason why the criteria in both Arnol'd's theorems and present theorems are the functions of $U''/(U-U_s)$. Since the stability of inviscid parallel flow depends only on the velocity profile's geometry shape, namely $f(y)$, and the magnitude of the velocity profile can be free, then the instability of inviscid parallel flow could be called "geometry shape instability" of the velocity profile. This distinguishes from the viscous instability associated with the magnitude of the velocity profile.

Moreover, the above theorem is essentially associated with vorticity distribution in the flow field. As known from Fjørtoft's criterion, the necessary condition for instability is that the base vorticity profile $\xi = -U'$ has a local maximum. Note that $U''/(U-U_s) \approx \xi_s''/\xi_s$ near the inflection point, where ξ_s is the vorticity at the inflection point, that means that the base vorticity ξ must be convex enough near the local maximum for instability, i.e., the vorticity should be concentrated somewhere in the flow for instability. Otherwise, the flow is stable if the vorticity distribution is smooth enough near the inflection point at y_s . A simple example can be obtained by following Tollmien's way [5]. Fig.1-2 depicts three vorticity profiles within the interval $-1 \leq y \leq 1$, which have local maximal at $y = 0$. Profile 2 ($U = -2 \sin(\pi y/2)/\pi$) is neutrally stable, while profile 1 ($U = -\sin(y)$) and profile 3 ($U = -\sin(2y)/2$) are stable and unstable, respectively.

To show the advantage of the criteria obtained above, we consider the stability of velocity profile $U = \tanh(\alpha y)$ within the interval $-1 \leq y \leq 1$, where α is a constant. This velocity profile is an classical model of mixing layer, and has been investigated by many researchers (see [2, 7, 13] and references therein). Since $U''(U-U_s) = -2\alpha^2 \tanh^2(\alpha y)/\cosh^2(\alpha y) < 0$ for $-1 \leq y \leq 1$, it might be unstable for any α according to both Rayleigh's and Fjørtoft's criteria. But it can be derived from Theorem 1 that the flow is stable for $\alpha^2 < \pi^2/8$. For example, we choose $\alpha_1 = 1.1$ and $\alpha_2 = 1.3$ for velocity profiles $U_1(y)$ and $U_2(y)$. The growth rate of the profiles can be obtained by Chebyshev spectral collocation method [13] with 100 collocation points, as shown in Fig.1-3. It is obvious that $c_i = 0$ for U_1 and $c_i > 0$ for U_2 , which agrees well with the criteria obtained above. This is also

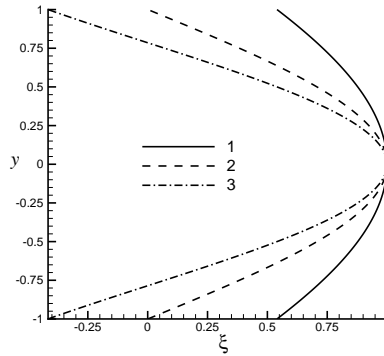


Figure 1-2: Vorticity profiles within the interval $-1 \leq y \leq 1$. Profile 2 ($\xi = \cos(\pi y/2)$, dashed) is neutrally stable, while profile 1 ($\xi = \cos(y)$, solid) and profile 3 ($\xi = \cos(2y)$, dash dotted) are stable and unstable, respectively.

a counterexample that Fjørtoft's criterion is not sufficient for instability. So this new criterion for stability is more useful in real applications.

Then, recalling the proof of theorem 1, we will find that the following Rayleigh's quotient $I(f)$ plays a key role in determining the stability of parallel flows.

$$I(f) = \min_{\phi} \frac{\int_a^b [\|\phi'\|^2 + f(y)\|\phi\|^2] dy}{\int_a^b \|\phi\|^2} \quad (1-11)$$

Note that the proof of theorem 1 is still valid in the case of $I(f) > 0$. We have such a result: parallel flows are stable if $I(f) > 0$. Although this criterion is more restrictive than that in theorem 1, it is inconvenient for the real applications due to the unknown Rayleigh's quotient $I(f)$. Theorem 1 is more convenient for the real applications in different research fields.

The present stability criteria give a affirmative answer to the questions at the beginning, i.e., there are some stable flows if $U''(U - U_s) < 0$. Based on the former criteria, the velocity profiles can be categorized as follows: (i) without inflection point (Reyleigh's criterion), (ii) $f(y) > 0$ (Fjørtoft's

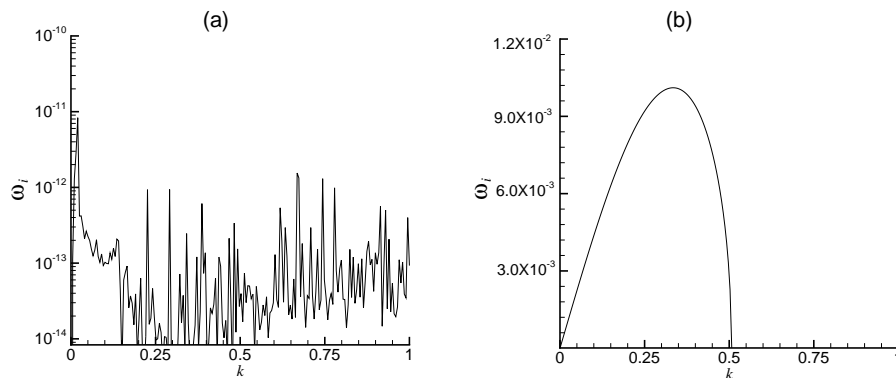


Figure 1-3: Growth rate ω_i as an function of wavenumber k , (a) for $U_1 = \tanh(1.1y)$, (b) for $U_2 = \tanh(1.3y)$, both within the interval $-1 \leq y \leq 1$.

$U'' > 0$ or $U'' < 0$	$U_s'' = 0$
A stable	B $f(y) > 0$ stable
	C $f(y) > -\mu_1$ stable
	D $f(y) < -\mu_1$ unstable

Figure 1-4: Diagram of stable velocity profiles.

criterion), and (iii) $-\mu_1 < f(y) < 0$ (present criterion), which are shown in Fig.1-4. Then the parallel flow might be unstable only for $f(y) < -\mu_1$ and $f(y)$ changing sign within the interval. However, if $f(y)$ changes sign somewhere within the interval $[a, b]$, then the parallel flow is stable. For that $f(y)$ changing sign implies $U_s''' = 0$ but $U_s'''' \neq 0$, so U'' does not change sign near the inflection point. Thus c_i must vanish in Eq.(1-4), i.e., the parallel flow is stable for $f(y)$ changing sign within the interval. In this way, the parallel flow might be unstable only for $f(y) < \mu_1$ somewhere, which will intrigue further studies on this problem. In fact, there are still stable flows if $\mu_1 < f(y)$ is violated.

Finally, the stable criterion for the parallel inviscid flows can be applied to the barotropic geophysical flows in a differentially rotating system. Considering the barotropic plane flows in a rotating frame, which are the approximations of barotropic geophysical flows [2, 3, 11], Eq.(1-1) changes to

$$(\phi'' - k^2\phi) - \frac{U'' - \beta}{U - c}\phi = 0, \quad (1-12)$$

where β is the gradient of the Coriolis parameter with respect to y . Eq.(1-12) is a generalized Rayleigh's equation, and there is a generalized stability criterion for these flows.

Theorem 2: The flow is stable, if the velocity profile satisfies either $-\mu_1 < \frac{U'' - \beta}{U - U_s} < 0$ or $0 < \frac{U'' - \beta}{U - U_s}$, where U_s is the velocity at the point $U''(y_s) = \beta$.

The above criteria would be helpful for understanding the wave-mean flow interaction, especially the Rossby wave-mean flow interaction in barotropic flows. According to the stable criteria, the necessary condition for wave-mean flow interaction can be obtained. And why the disturbed waves can't take energy from the mean flow in the stable flow is revealed. If the flow is stable, there is no wave-mean flow interaction at all.

First, when the velocity profile has no inflection point, then the speeds of barotropic waves $c_r - U \neq 0$. According to Eq.(1-3), $U - c_r > 0$ holds for $U'' < 0$, i.e., the barotropic waves are always west-propagation relative to the mean flow U if the vortex gradient is positive. This extends the west-propagation theory of Rossby waves. And $U - c_r < 0$ holds for $U'' > 0$, i.e., the barotropic waves are always east-propagation relative to the mean flow U if the vortex gradient is negative. Second, when the velocity profile has an inflection point $U_s'' = 0$, the speed of most favorite wave which might have interaction with the mean flow should be $c_r = U_s$. However, the wave speed $c_r \neq U_s$ holds for $-\mu_1 < \frac{U''}{U - U_s} < 0$, as has been pointed out in proposition 1. In short, the waves have no interaction with the mean flows whatever there is an inflection point or not. This conclusion can be easily generated to the flows in β plane. Thus, the waves have no interaction with the stable flows. This is the reason why the disturbed waves can't take energy from the stably mean flow.

On the other hand, [15] pointed out that c_r of a unstable wave must lie between the minimum and the maximum values of the mean velocity profile. Thus, the unstable wave is stationary relative to the mean flow, and can take energy from the mean flow. So there are wave-mean flow interactions in unstable flows.

§ 1.1.4 Conclusion

In summary, the general stability criteria are obtained for inviscid parallel flow. Both the criteria and the proofs are remarkably simple and easy to understand, comparing to Arnol'd's nonlinear theorems. The new criteria extend the former theorems proved by Rayleigh, Tollmien and Fjørtoft. This may shed light on the flow control and investigation of the vortex dynamics. Based on the stability criteria, the reason why the disturbed waves can't take energy from the stably mean flow is explained that there is no wave-mean flow interaction at all.

§ 1.2 Longwave Instability

§ 1.2.1 Introduction

Shear instability, caused by the velocity shear, is one of most important instabilities in the flows. Although the mechanism of shear instability is not full revealed yet, it is applied to explain the instability of mixing layer, jets in pipe, wakes behind cylinder, etc. Some simple models were employed to study the shear instability, including Kelvin-Helmholtz (K-H) model, piecewise linear velocity profile [16] and continued velocity profiles [1], etc. To reveal the mechanism of shear instability, the stability of perturbation waves should be understood. In K-H model, the growth rate of the disturbance wave is proportion to the product of wavenumber and velocity shear, thus the shortwaves are more unstable than longwaves in K-H model. However, Rayleigh [16] found that the piecewise linear profile is linearly unstable only in a finite range of wavenumbers $0 \leq k < k_c$, which means the shortwaves are stable in this case [2, 7, 16, 17]. A contradiction [2, 7] emerges as shortwave and longwave dominate the shear instability in K-H model and piecewise linear profiles, respectively. This was explained either as viscous effect must be considered for shortwave [2] or as longwaves do not "feel" the finite thickness of the layer [2, 7].

To dispel the contradiction, we should find out which dominates the shear instability, shortwave or longwave? It is from the numerical simulation (see [2, 7, 13] and references therein) and some theoretical analysis (e.g. Tollmien [5] and Lin [18]) that longwave might be more unstable than shortwave. They also proved the long-wave instability subject to the velocity profile U is either symmetric or monotone. We will investigate this problem following the way by Sun [19].

Moreover, a prior estimation of growth rate, which may be obtained from the investigation, is useful for unstable flows. For example, Howard's semicircle theorem [15] has been used to validate the numerical calculations [13]. Another useful result was found by Høiland [20] and Howard [15] that the growth rate ω_i must less equate to half of the maxim of vorticity, i.e., $\omega_i \leq |U'|_{\max}/2$. But this estimation is too cursory to use in applications. For example, U' is always great than zero even the velocity profile has no inflection point. So this estimation is trivial for these cases. Here we will show a refinement estimation of growth rate, which can be applied to general velocity profiles in parallel flows.

The motivation of this short letter is to investigate these problems within the context of inviscid parallel flow. The aim here is to find out some general characters for unstable waves.

§ 1.2.2 Model and Analysis

To this purpose, long-wave instability in shear flows is investigated via Rayleigh's equation [1, 2, 7, 17]. For a parallel flow with mean velocity $U(y)$, where y is the cross-stream coordinate. The streamfunction of the disturbance expands as series of waves (normal modes) with real wavenumber k and complex frequency $\omega = \omega_r + i\omega_i$, where ω_i relates to the grow rate of the waves. The flow is unstable if and only if $\omega_i > 0$. We study the stability of the disturbances by investigating the growth rate of the waves, this method is known as normal mode method. The amplitude of waves, namely ϕ , holds

$$(\phi'' - k^2\phi) - \frac{U''}{U - c}\phi = 0, \quad (1-13)$$

where $c = \omega/k = c_r + ic_i$ is the complex phase speed. The real part of complex phase speed $c_r = \omega_r/k$ is the wave phase speed. This equation is to be solved subject to homogeneous boundary conditions

$$\phi = 0 \text{ at } y = a, b. \quad (1-14)$$

From Rayleigh's equation, we get the following equations:

$$\int_a^b [(\|\phi'\|^2 + k^2\|\phi\|^2) + \frac{U''(U - c_r)}{\|U - c\|^2}\|\phi\|^2] dy = 0, \quad (1-15)$$

and

$$c_i \int_a^b \frac{U''}{\|U - c\|^2} \|\phi\|^2 dy = 0. \quad (1-16)$$

Before the further discussion, we need estimate the rate of $\int_a^b \|\phi'\|^2 dy$ to $\int_a^b \|\phi\|^2 dy$, as Sun did [19]. This is known as Poincaré's problem:

$$\int_a^b \|\phi'\|^2 dy = \mu \int_a^b \|\phi\|^2 dy, \quad (1-17)$$

where the eigenvalue μ is positive definition for $\phi \neq 0$. The smallest eigenvalue value, namely μ_1 , can be estimated as $\mu_1 > (\frac{\pi}{b-a})^2$. And an auxiliary function $f(y) = \frac{U''}{U - U_s}$ is also introduced, where $f(y)$ is finite at inflection point.

With the preparation above, we have such consequence. If $-f(y) < Q < \infty$, where Q is a positive constant, then the disturbances with shortwaves $k > k_c$ are always stable, where k_c is a critical wavenumber subject to $k_c^2 = Q - \mu_1$. We will prove the consequence by two steps. At first, we prove proposition 1: if $c_r = U_s$, the disturbances with shortwaves $k > k_c$ are always stable.

Proof: Since $U'' = f(y)(U - U_s)$ and $c_r = U_s$, this yields to

$$\frac{U''(U - U_s)}{\|U - c\|^2} > f(y) \frac{U''}{U - U_s} > -Q, \quad (1-18)$$

and

$$\int_a^b [(\|\phi'\|^2 + k^2\|\phi\|^2) + \frac{U''(U - U_s)}{\|U - c\|^2}\|\phi\|^2] dy \geq \int_a^b [(\mu_1 + k_c^2 + \frac{U''(U - U_s)}{\|U - c\|^2})\|\phi\|^2] dy > 0. \quad (1-19)$$

This contradicts Eq.(1-15). So proposition 1 is proved.

Then, we prove proposition 2: if $c_r \neq U_s$, there must be $c_i^2 = 0$ with $k > k_c$.

Proof: Otherwise if $c_i^2 \neq 0$, so according to Eq.(1-15) and Eq.(1-16), for any arbitrary real number U_t which does not depend on y , it holds

$$\int_a^b [(\|\phi'\|^2 + k^2\|\phi\|^2) + \frac{U''(U - U_t)}{\|U - c\|^2}\|\phi\|^2] dy = 0. \quad (1-20)$$

But the above Eq.(1-20) can not be hold for some special U_t . For example, let $U_t = 2c_r - U_s$, then there is $(U - U_s)(U - U_t) < \|U - c\|^2$, and

$$\frac{U''(U - U_t)}{\|U - c\|^2} = f(y) \frac{(U - U_s)(U - U_t)}{\|U - c\|^2} > -Q. \quad (1-21)$$

For $k > k_c$, this yields to

$$\int_a^b \{ \|\phi'\|^2 + [k^2 + \frac{U''(U - U_t)}{\|U - c\|^2}] \|\phi\|^2 \} dy > 0, \quad (1-22)$$

which also contradicts Eq.(1-20). So proposition 2 is also proved. These two propositions are natural generalization of stable criterion proved by Sun [19].

From the above two propositions, we can draw a conclusion that the disturbances with shortwaves $k > k_c$ are always stable. This means that the shear instability in flows must be long-wave instability. Furthermore, the short-wave stability means that without any viscous effect, the shortwaves can also be damped by shear flow. This mechanism is unlike the viscous mechanism that the viscosity has a damping effect on especially the shortwaves. It implies that the shear flow itself can damp the shortwaves. This is very general and important conclusion, which explains why the instabilities found in shear flows are mostly long-wave instabilities.

§ 1.2.3 Discussion

This result is also very important for numerical calculation, which means shortwaves can be truncated in the calculations without changes the stability of shear flow. So the growth rates of longwaves have enough information for judging the stability of shear flow. On the other hand, the truncation of longwaves would probably change the instability of the shear flow. So the streamwise length scale must be longer enough to have longwaves for the numerical simulations in shear flows, such as plane parallel flow and pipe flow. Otherwise the instability of shear flow would be damped without long-wave perturbations.

Then the growth rate of unstable waves can be estimated here by following the former investigation. Similar to the assumption above, $-f(y) < Q = p^2\mu_1 < \infty$, where $1 < p < 2$, we will show that the growth rate is subject to $\omega_i \leq (p - 1)\sqrt{\mu_1}|U_{\max} - U_{\min}|$.

Proof: It is from Eq.(1-15) that gives

$$\int_a^b k^2 \|\phi\|^2 dy = \int_a^b -[\|\phi'\|^2 + \frac{U''(U - c_r)}{\|U - c\|^2} \|\phi\|^2] dy. \quad (1-23)$$

Substituting Eq.(1-17) to Eq.(1-23) and recalling that $\mu_1 < \mu$, this yields

$$\int_a^b k^2 \|\phi\|^2 dy \leq \int_a^b -[\frac{U''(U - c_r)}{\|U - c\|^2} + \mu_1] \|\phi\|^2 dy. \quad (1-24)$$

Multiplying above inequality (1-24) by c_i^2 , we get

$$\omega_i^2 \int_a^b \|\phi\|^2 dy \leq \int_a^b h(y) \|\phi\|^2 dy, \quad (1-25)$$

where

$$h(y) = -[\frac{U''(U - c_r)}{\|U - c\|^2} + \mu_1] c_i^2. \quad (1-26)$$

Suppose the maxim of $h(y)$ is P^2 , then the growth rate is subject to

$$\omega_i^2 \leq P^2. \quad (1-27)$$

This follows

$$h(y) \leq -[\frac{U''(U - c_r)}{(U - c_r)^2 + c_i^2} + \mu_1] c_i^2. \quad (1-28)$$

Substitution of $f(y)$ into Eq.(1-28), gives

$$h(y) \leq \mu_1 [\frac{(p^2 - 1)(U - c_r)^2 - c_i^2}{(U - c_r)^2 + c_i^2}] c_i^2. \quad (1-29)$$

When

$$c_i^2 = (p - 1)(U - c_r)^2, \quad (1-30)$$

the right hand of Eq.(1-29) get its largest value

$$P^2 = (p - 1)^2 \mu_1 (U - c_r)^2. \quad (1-31)$$

Then the growth rate must be subject to

$$\omega_i \leq (p - 1) \sqrt{\mu_1} |U_{\max} - U_{\min}|, \quad (1-32)$$

where U_{\min} and U_{\max} are minimum and maximum of $U(y)$, respectively. And the wavenumber k_{\max} corresponding to the largest growth rate is

$$k_{\max} = \sqrt{(p - 1)\mu_1}. \quad (1-33)$$

So the result is proved. One should note that the fast growth rate ω_i is only an approximation, but not a precision one, so as to wavenumber k_{\max} .

Comparing with the previous one by Høiland and Howard, the above estimation includes not only a more precision estimation about the the growth rate of unstable waves but also the regime of unstable wavenumbers. This would be much helpful for validation in numerical calculations.

As well known, the instability due to velocity shear is always associated to Kelvin-Helmholtz instability (K-H instability), in which the disturbances of all wavelengths are amplified. According

to K-H instability, the shorter the wavelength is, the faster the perturbation wave amplifies. As the above investigation points out that the shortwaves are always more unstable than longwaves in this case, the contradiction at the beginning can be dispelled.

An physical explanation [2, 7] to the contradiction is that the K-H instability model has no intrinsic length scale, while Rayleigh's model has width of shear layer as length scale of waves. This can be noted from that Rayleigh's case reduces to the Kelvin-Helmholtz vortex sheet model in the long-wave limit $k \ll 1$ [2, 7], which is dramatically explained as longwave do not "feel" the finite thickness of the shear layer [7]. Here we will show that this explanation can be extend to shear flows. It is from Eq.(1-33) that the fastest growing wavenumber k_{\max} is proportion to $\sqrt{\mu_1}$, then the corresponding wave length λ_{\max} is approximately $2(b-a)/\sqrt{p-1}$. So the thinner the shear layer is, the lager the fastest growing wavenumber is. It can be seen that the asymptotic case of infinite small shear layer leads to K-H instability. This is another evidence that K-H instability is in essence of long-wave instability. In this case, the K-H instability is an approximation of shear instability when the wave length of perturbation is much longer than the width of shear layer.

In summary, two general properties of shear instability are obtained in the investigations. Firstly, the shortwaves are always stable in the continued profile flows and the shear instability is due to long-wave instability. This implies that the shear flow itself can damp the shortwaves and that K-H instability is in essence of long-wave instability in shear flow. The result can be used to understand the phenomena in hydrodynamics instabilities. Secondly, the growth rate of unstable flow can be estimated as $\omega_i \leq (p-1)\sqrt{\mu_1}(U_{\max} - U_{\min})$. This estimation extend the previous result obtained by Høiland and Howard. Both results are important in numerical applications. The first one provides the estimation of unstable wavenumbers, and the second one provides the estimation of growth rate of unstable waves. These results may be useful on both numerical calculation and stability analysis.

§ 1.3 Mechanism of Shear Instability

§ 1.3.1 Introduction

The hydrodynamic instability is a fundamental problem in many fields, such as fluid dynamics, astrodynamics, oceanography, meteorology, etc. There are many kinds of hydrodynamic instabilities, e.g., shear instability due to velocity shear, thermal instability due to heating, viscous instability due to viscosity and centrifugal instability due to rotation, etc. Among them, the shear instability (inviscid) is the most important and the simplest one, which has been intensively explored (see [2, 6, 7] and references therein). Both linear and nonlinear stabilities of shear flow have been considered, and some important conclusions have also be obtained from the investigations.

On the one hand, the nonlinear stability of shear flow has been investigated via variational principles. Kelvin [21] and Arnol'd [9, 10, 14] have developed variational principles for two-dimensional inviscid flow [22]. They showed that the steady flows are the stationary solutions of the energy H . And if the second variation $\delta^2 H$ is definite, then the steady flow is nonlinearly stable. Moreover, Arnol'd proved two nonlinear stability criteria, and that the flow is linearly stable as $\delta^2 H$ is positive definite [10, 14, 22, 23]. However, Arnol'd's theorem is not convenient to use as $\delta^2 H$ is always indefinite in sign, except for two special cases (see [23] and references therein). Due to the lack of the explicit expressions in both H and the stability criteria the variational principle is inconvenient for real applications.

On the other hand, the linear stability of shear flow has also been investigated via Rayleigh's equation. Within the linear context, there are three important general stability criteria, namely Rayleigh's criterion [1], Fjørtoft's criterion [4] and Sun's criterion [19]. As all the criteria have explicit expressions, they are more convenient in real applications, and are widely used in many fields. Based on the previous investigations, Sun [19] also pointed out that the flow is stable for Rayleigh's quotient $I(f) > 0$ (see Eq.(1-11) behind). However, the sufficient criterion for instability still lacks.

To understand the shear instability, some mechanisms were suggested. Among them, Kelvin-Helmholtz instability (K-H instability) is always taken as a prototype, which is physically explained as the instability of a sheet vortex [24]. Another mechanism of instability is due to the resonance of waves [2, 25, 26, 27, 28]. Butler and Farrell [26] clearly showed with numerical simulations that the resonance introduces an algebraic growth term into the temporal development of a disturbance. Baines and Mitsudera [27] also used broken-line profile velocity as a prototype to explain the interaction of waves. Their explanation is so brilliant that it can explain why the instability occurs for a finite range of wavenumber and how the waves amplify each other. However, both mechanisms are independent of the basic flows, for that Kelvin-Helmholtz model deals only with vortex and resonance mechanism only considers the waves. Thus the relationships between those mechanisms and the shear flows are still covered.

Overview the previous investigations, the essence of the shear instability is remained to be elucidated. Yet both the explicit expression and the meaning of H have not been revealed before, although it is very important in variational principles. The connection between linear and nonlinear stability criteria should be retrieved explicitly. The relationships between instability mechanisms and the physical explanation for shear instability are needed. The aim of this paper is to reveal the essence of the shear instability by investigating the inviscid shear flows in a channel. And this would lead to a more comprehensive understanding on shear instabilities.

§ 1.3.2 Stable Criterion

For the two-dimensional inviscid flows with the velocity of U , the vorticity $\xi = \nabla \times U$ is conserved along pathlines [7, 22, 24]:

$$\frac{d\xi}{dt} = \frac{\partial \xi}{\partial t} + (U \cdot \nabla)\xi = 0. \quad (1-34)$$

Its linear disturbance reduces to Rayleigh's equation provided the basic flow U being parallel. Considers an shear flow with parallel horizontal velocity $U(y)$ in a channel, as shown in Fig.1-5. The amplitude of disturbed flow streamfunction ψ , namely ϕ , satisfies [2, 6, 7]:

$$(\phi'' - k^2\phi) - \frac{U''}{U - c}\phi = 0, \quad (1-35)$$

where k is the nonnegative real wavenumber and $c = c_r + ic_i$ is the complex phase speed and double prime $''$ denotes the second derivative with respect to y . The real part c_r is the phase speed of wave, and $c_i \neq 0$ denotes instability. This equation is to be solved subject to homogeneous boundary conditions $\phi = 0$ at $y = a, b$.

Considers that the velocity profile $U(y)$ has an inflection point y_s at which $U_s'' = U''(y_s) = 0$ and $U_s = U(y_s)$. As Sun [19] has pointed out, the following Rayleigh's quotient $I(f) > 0$ implies the

flow is stable.

$$I(f) = \min_{\phi} \frac{\int_a^b [\|\phi'\|^2 + f(y)\|\phi\|^2] dy}{\int_a^b \|\phi\|^2 dy} \quad (1-36)$$

where $f(y) = \frac{U''}{U-U_s}$. While if $I(f) < 0$, then there is a neutral stable model with $k_N^2 = -I(f)$ and $c_r = U_s$. Moreover, there are unstable modes with $c_r = U_s$ and $c_i \neq 0$ if $I(f) < 0$ and $0 \leq k < k_N$. This can also be proved by following the way by Tollmien [5], Friedrichs [6, 29, 30] and Lin [18]. Thus $I(f) = 0$ means the flow is neutrally stable. And there is only one neutral mode with $k = 0$ and $c_r = U_s$ in the flow. These conclusions can be summarized as a new theorem.

Tollmien-Fridrichs-Lin theorem: The flows are neutrally stable, if $I(f) = 0$. The flows are stable and unstable for $I(f) > 0$ and $I(f) < 0$, respectively.

From the above proof, it is obvious that the shortwaves (e.g. $k \gg k_N$) are always more stable than longwaves (e.g. $k \ll k_N$) in the inviscid shear flows [30, 31]. So the shear instability is due to long-wave instability, and the disturbances of shortwaves can be damped by the shear itself without any viscosity [31].

As mentioned above, the linear stability criterion can be derived from the nonlinear one [14]. Moreover, the nonlinear stability criterion can also be obtained from the linear one. To illuminate this, the nonlinear criterion is retrieved explicitly via the above theorem, which is briefly proved as follows.

Similar to Arnol'd's definition, the general energy H here is defined as

$$H = \frac{1}{2} \int_a^b [\frac{1}{2} \|\nabla \Psi\|^2 + h(\Psi)] dy \quad (1-37)$$

where $\Psi(y)$ is the streamfunction of the flow with $\frac{\partial \Psi}{\partial y} = U(y) - U_s$, and $h(\Psi)$ is a function of Ψ . The variation of $\delta H = 0$ gives

$$\Delta \Psi = h'(\Psi). \quad (1-38)$$

So Arnol'd's variational principle is retrieved. And the function $h = \|\nabla \Psi\|^2/2$ can also be obtained by solving Eq.(1-38). Then, the second variation $\delta^2 H$ holds

$$\delta^2 H = \frac{1}{4} \int_a^b [\|\nabla \psi\|^2 + h''(\Psi)\psi^2] dy, \quad (1-39)$$

where ψ denotes the variation $\delta \Psi$. Noting that $h''(\Psi)$ remains unknown, Arnol'd's nonlinear criteria have not be extensively used. Fortunately, we can obtain the explicit expression of $h''(\Psi)$ here via the investigation on the linear stability criterion. For $\frac{\partial \Psi}{\partial y} = U - U_s$,

$$h''(\Psi) = \frac{dh'}{d\Psi} = \frac{dh'}{dy} \frac{dy}{d\Psi} = \frac{U''}{(U - U_s)} = f(y). \quad (1-40)$$

As $h''(\Psi)$ is solved explicitly, $\delta^2 H$ has an explicit expression, which is greatly helpful for real applications.

Let the streamfunction of the perturbation expands as travelling waves $\psi(x, y, t) = \phi(y)e^{i(kx - \omega t)}$, where ω is the frequency. The averages of $\|\nabla \psi\|^2$ and $\|\psi\|^2$ are $(\|\phi'\|^2 + k^2\|\phi\|^2)/2$ and $\|\phi\|^2/2$ along the flow direction x , respectively. So Eq.(1-39) reduces to

$$\delta^2 H = \frac{1}{8} \int_a^b [\|\phi'\|^2 + k^2\|\phi\|^2 + f(y)\|\phi\|^2] dy. \quad (1-41)$$

The sign of $\delta^2 H$ is then associated with $I(f)$ in Eq.(1-36). If $I(f) < 0$, the second variation $\delta^2 H$ can be both negative and positive, i.e., the stationary solution is a saddle point. And $I(f) > 0$ implies $\delta^2 H$ is positive definite and vice versa. So the stable flow has the minimum value of the total kinetic energy H . The physical meaning of H can also be revealed, as the explicit expressions of H , $\frac{\partial \Psi}{\partial y} = U - U_s$ and $h''(\Psi) = f(y)$ have been obtained.

First, according to the expressions, the velocity U in vorticity conservation law Eq.(1-34) can be decomposed to two parts: the rotational flow $U - U_s$ and the irrotational advection flow U_s . The vorticity ξ in Eq.(1-34) depends only on $U - U_s$, and U_s is only advection velocity. Then $U - U_s$ and U_s are associated with the dynamics and kinetics of the flow, respectively. Eq.(1-34) physically shows that the vorticity field is advected by U_s , which can also known from the conservation of vorticity in the inviscid flows. A similar example is the dynamics of vortex in the wake behind cylinder, where the vortices dominate the dynamics of the flow and they are advected by mean flow (see Fig.2 in [32]). The decomposition of velocity may be useful in vortex dynamics, for that our investigation clearly shows that the dynamics of the flow is dominated by vorticity distribution.

Then the physical meaning of H can also be understood from the above investigation. It is not U but $U - U_s$ that is associated with the general energy H , so $H = \frac{1}{2} \int_a^b (U - U_s)^2 dy$ is not the total kinetic energy but the kinetic energy of flow with vorticity. Thus the stable steady states are always minimizing the kinetic energy of the flow associated with vorticity. This is also the reason why the flow with maximum vorticity might be unstable, as Fjørtoft's criterion shows. We would like to restate it as a theorem and to name it after Kelvin [21] and Arnol'd [14] for their contributions on this field [22].

Kelvin-Arnol'd theorem: the stable flow minimizes the kinetic energy of flow associated with vorticity.

Both Tollmien-Fridrichs-Lin theorem and Kelvin-Arnol'd theorem are equivalent to the following simple principle [33]: The flow is stable, if and only if all the disturbances with $c_r = U_s$ are neutrally stable.

§ 1.3.3 Physical explanation

We have obtained the sufficient and necessary conditions for instability, then the physical mechanism of instability can be understood from them. According to Fjørtoft's and Sun's criteria [19], the necessary conditions for instability require that the base vorticity must be concentrated enough (e.g. sheet vortex). We call it "concentrated vortex" for latter convenience. The following investigation will reveal that the essence of shear instability is due to the interaction between the "concentrated vortex" and the corresponding resonant waves.

As mentioned above, the concentrated vortex is a general model of sheet vortex in the Kelvin-Helmholtz model, for that the sheet vortex can be recovered as the concentrated vortex $\xi(y_s) \rightarrow \infty$ (see [12] for a comprehensive discussion about the Kelvin-Helmholtz model and continued shear profiles). Then how the shear flow becomes unstable, if there is a concentrated vortex? As the sufficient condition for instability is $I(f) < 0$, the normal modes in the regime of $0 \leq k < k_N$ with $c_r = U_s$ are unstable. These modes are stationary or standing waves, comparing to the velocity at inflection point. So that the shear instability is due to the disturbance of concentrated vortex by the standing waves with $c_r = U_s$. In this case, the resonance mechanism is valid. The interaction waves propagate at the same speed with the concentrated vortex, so that they are locked together and amplified by simple advection [27]. In short, the disturbances on concentrated vortex is amplified like that in

Kelvin-Helmholtz model.

This instability mechanism combines both K-H instability and resonance mechanism. Physically, the standing waves (with $c_r = U_s$) can interact with the concentrated vortex, so they can trigger instability in the flows. While the travelling waves (with $c_r \neq U_s$) have no interaction with the concentrated vortex, so that they can not trigger instability in the flows. This is the mechanism of shear instability. As pointed out above, the inviscid shear instability is due to long-wave instability. If the longwaves are unstable, they can obtain the energy from background flows. Thus, the energy within small scales transfer to and concentrate on large scales. In a word, the shear instability itself provides a mechanism to inverse energy cascade and to maintain the large structures or coherent structures in the complex flows.

To illuminate the mechanism of shear instability, a physical diagram is also presented here by following the way of interpreting the K-H instability [24]. Fig.1-5 sketches the mechanism of shear instability in terms of wave disturbances of vortices. The mean velocity profile $U(y)$ has an inflection point at $y_s = 0$ with $U_s = 0$, and the corresponding vorticity is $\xi(y) = -U'(y)$. There is a local maximum at y_s in the unstable vorticity profile in Fig.1-5a. According to Eq.(1-34), the vorticity is conserved in the inviscid flows. If the vortices at the local maximum (A, B and C) are sinusoidally disturbed from their original positions (dashed line) to new places (solid curve), they have negative vorticities with respect to the undisturbed ones. The vortices will induce cyclone flows around them in consequence. The flows around the vortices become faster (slower) in the upper (lower) of vortex A referred to the basic flow $U(y)$. The pressures at upper and lower decrease (indicated by - signs) and increase (indicated by + signs) according to Bernoulli's theorem, respectively. Then vortex A gets a upward acceleration due to the disturbed pressure difference as the uparrow shows. This tends to take the vortex away from its original position, so the flow is unstable. On the other hand, Fig.1-5b depicts the disturbances in a stable velocity profile, where a local minimum is in the vorticity profile. The disturbed vortices have positive vorticities with respect to the undisturbed ones. The vortices

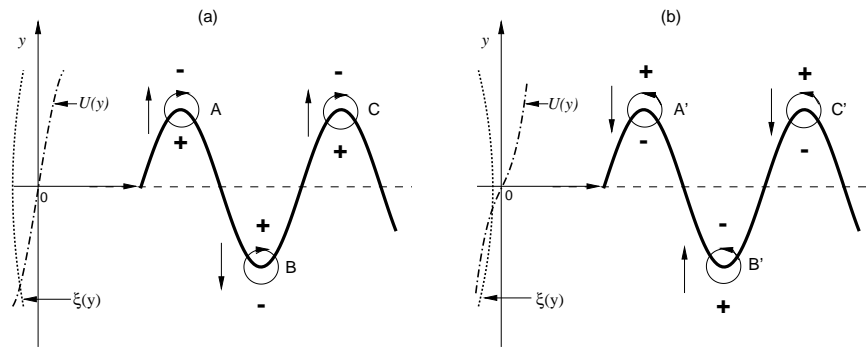


Figure 1-5: Sketch of shear instability: physical interpretation. Left parts depict the profiles of velocity $U(y)$ and vorticity $\xi(y)$, right ones depict the disturbance of vorticities. The unstable velocity profile $U(y)$ has a local maximum in vorticity $\xi(y)$ (a). If the vortices (A, B and C) disturbed from their original positions (dashed line) to new places (solid curve), they will be taken away from their original positions due to pressure difference. The stable velocity profile $U(y)$ has a local minimum in vorticity $\xi(y)$ (b). The disturbed vortices (A', B' and C') will be brought back to their original positions due to pressure difference.

will induce anticyclone flows around them in consequence. So vortex A' get a downward acceleration due to the disturbed pressure difference as the downarrow shows. This tends to bring the vortex back from its original position, so the flow is stable. In this interpretation, the advection of U_s is independent of the shear instability, only the flow field of $U - U_s$ and the corresponding vorticity ξ are the dominations. The unstable disturbances in Fig. 1-5 have $c_r = U_s$, which consists with the above discussions. This physically explains why the maximum and minimum vorticities have different stable aspects.

Though Tollmien-Fridrichs-Lin theorem is a sufficient and necessary condition for stability, the unknown ϕ in the theorem restricts its application. So some simple criteria may be more useful. For the parallel flows within interval $a \leq y \leq b$, there are two simple criteria.

Corollary 1: The flow is stable for $f(y) > -(\frac{\pi}{b-a})^2$ [19, 33].

Corollary 2: The flow is unstable for $f(y) < -(\frac{\pi}{b-a})^2$ [33].

In summary, the general stability and instability criteria are retrieved for inviscid parallel flow within linear context, which are associated with the nonlinear stability criteria, i.e., minimizing the kinetic energy of flow. Then the mechanism of shear instability is explained as the resonance of standing waves with the concentrated vortex at $c_r = U_s$. The physical process is also sketched by extending the way of interpreting K-H instability. Finally, some useful criteria are given. These results would lead to a more comprehensive understanding on shear instabilities, especially for undergraduate students.

§ 1.4 Rotating Flow

§ 1.4.1 Introduction

The instability of the rotating flows is one of the most attractive problems in many fields, such as fluid dynamics, astrophysical hydrodynamics, oceanography, meteorology, etc. Among them, the simplest one is the instability of pure rotation flow between coaxial cylinders, i.e., Rayleigh-Taylor problem, which has intensively been explored [6, 17].

Two kinds of instabilities in inviscid rotating flow have been theoretically addressed in the literatures. One is centrifugal instability, which was first investigated by Rayleigh [1, 6]. He derived the circulation criterion for the inviscid rotating flows that a necessary and sufficient condition for stability to axisymmetric disturbances is that the square of the circulation does not decrease anywhere. This criterion is also be stated as the Rayleigh discriminant $\Phi \geq 0$ (see Eq.(1-46) behind), and is always be used in astrophysical hydrodynamics [34]. It is also generalized to non-axisymmetric flows [35]. The other is known as instability due to two-dimensional disturbances in rotating flows, which is similar to the shear instability in parallel flow. We call this instability as the shear instability in rotating flow hereafter. For this instability, Rayleigh also obtained a criterion, i.e., inflection point theorem in inviscid rotating flows, which is the analogue of the theorem in parallel flows [1]. Following this way, Howard and Gupta [36] found a stability criterion for two-dimensional disturbance in inviscid rotating flow. However, the theoretical results remains scarce, due to the complexity of rotating flow.

Comparing this to shear instability in parallel flows, the criteria for parallel flows are much more abundant. Fjørtoft [4] and Sun [19] proved some more strict criteria. And the stability of two-dimensional in a rotating frame was also addressed by Pedley [37], which seems to be more complex than the stability problem in the pure rotation flows.

Motivated, then, by the theoretical criteria for parallel flows [4, 19], our study focuses on the instability due to shear in inviscid rotating flows. The aim of this letter is to obtain such criteria for the inviscid rotating flows, and the relationship between previous criteria is also discussed. Thus other instabilities may be understood via the investigation here.

§ 1.4.2 Howard-Gupta Equation

For this purpose, Howard-Gupta equation (hereafter H-G equation) [36] is employed. To obtain H-G equation, Euler's equations [2, 6, 17, 24] for incompressible barotropic flow in cylindrical polar coordinates (r, θ) are then given by

$$\frac{\partial u_r}{\partial t} + u_r \frac{\partial u_r}{\partial r} + \frac{u_\theta}{r} \frac{\partial u_r}{\partial \theta} - \frac{u_\theta^2}{r} = -\frac{1}{\rho} \frac{\partial p}{\partial r}, \quad (1-42)$$

and

$$\frac{\partial u_\theta}{\partial t} + u_r \frac{\partial u_\theta}{\partial r} + \frac{u_\theta}{r} \frac{\partial u_\theta}{\partial \theta} + \frac{u_r u_\theta}{r} = -\frac{1}{\rho r} \frac{\partial p}{\partial \theta}. \quad (1-43)$$

Under the condition of incompressible barotropic flow, the evolution equation for the vorticity can be obtained from Eq.(1-42) and Eq.(1-43),

$$\frac{\partial \xi}{\partial t} + u_r \frac{\partial \xi}{\partial r} + \frac{u_\theta}{r} \frac{\partial \xi}{\partial \theta} = 0, \quad (1-44)$$

where $\xi = \frac{1}{r} \frac{\partial}{\partial r}(r u_\theta) - \frac{1}{r} \frac{\partial u_r}{\partial \theta}$ is the vorticity of the background flow. Eq.(1-44) can also be derived from Fridman's vortex dynamics equation [22, 24]. And it admits a steady basic solution,

$$u_r = 0, u_\theta = V(r) = \Omega(r)r, \quad (1-45)$$

where $\Omega(r)$ is the mean angular velocity. And Rayleigh discriminant is defined by

$$\Phi = \frac{1}{r^3} \frac{d}{dr}(\Omega r^2)^2. \quad (1-46)$$

§ 1.4.3 Stable Criterion

Then, consider the evolution of two-dimensional disturbances. The disturbances $\psi'(r, \theta, t)$, which depend only on r , θ and t , expand as series of waves,

$$\psi'(r, \theta, t) = \phi(r)e^{i(n\theta - \omega t)}, \quad (1-47)$$

where $\phi(r)$ is the amplitude of disturbance, n is real wavenumber and $\omega = \omega_r + i\omega_i$ is complex frequency. Unlike the wavenumber in Rayleigh's equation for inviscid parallel flows, the wavenumber n here must be integer for the periodic condition of θ . The flow is unstable if and only if $\omega_i > 0$. In this way, the amplitude ϕ satisfies

$$(n\Omega - \omega)[D^* D - \frac{n^2}{r^2}]\phi - \frac{n}{r}(D\xi)\phi = 0, \quad (1-48)$$

where $D = d/dr$, $D^* = d/dr + 1/r$. This equation is known as H-G equation and to be solved subject to homogeneous boundary conditions

$$D\phi = 0 \text{ at } r = r_1, r_2. \quad (1-49)$$

By multiplying $\frac{r\phi^*}{\omega - \Omega n}$ to H-G equation Eq.(1-48), where ϕ^* is the complex conjugate of ϕ , and integrating over the domain $r_1 \leq r \leq r_2$, we get the following equation

$$\int_{r_1}^{r_2} r \{ \phi^* (D^* D) \phi - [\frac{n^2}{r^2} + \frac{nD(\xi)}{r(n\Omega - \omega)}] \|\phi\|^2 \} dr = 0. \quad (1-50)$$

Then the integration gives

$$\int_{r_1}^{r_2} r \{ \|\phi'\|^2 + [\frac{n^2}{r^2} + \frac{n(\Omega n - \omega^*)\xi'}{r\|\Omega n - \omega\|^2}] \|\phi\|^2 \} dr = 0, \quad (1-51)$$

where $\phi' = D\phi$, $\xi' = D(\xi)$ and ω^* is the complex conjugate of ω . Thus the real part and image part are

$$\int_{r_1}^{r_2} r \{ \|\phi'\|^2 + [\frac{n^2}{r^2} + \frac{(\Omega - c_r)\xi'}{r\|\Omega - c\|^2}] \|\phi\|^2 \} dr = 0, \quad (1-52)$$

and

$$\int_{r_1}^{r_2} \frac{c_i \xi'}{\|\Omega - c\|^2} \|\phi\|^2 dr = 0, \quad (1-53)$$

where $c = \omega/n = c_r + ic_i$ is the complex angular phase speed. Rayleigh used only Eq.(1-53) to prove his theorem: The necessary condition for instability is that the gradient of the basic vorticity ξ' must change sign at least once in the interval $r_1 < r < r_2$. The point at $r = r_s$ is called the inflection point with $\xi'_s = 0$, at which the angular velocity of $\Omega_s = \Omega(r_s)$. This theorem is the analogue of Rayleigh's inflection point theorem for parallel flow [1, 6].

Similar to the proof of Fjørtoft theorem [4] in the parallel flow, we can prove the following criterion.

Theorem 1: A necessary condition for instability is that $\xi'(\Omega - \Omega_s) < 0$ (or $\xi'/(\Omega - \Omega_s) < 0$) somewhere in the flow field.

The proof of Theorem 1 is trivial, and is omitted here. This criterion is more restrictive than Rayleigh's. Moreover, some more restrictive criteria may also be found, if we follow the way given by Sun [19]. If the velocity profile $\Omega(r)$ is stable ($c_i = 0$), then the hypothesis $c_i \neq 0$ should result in contradictions in some cases. So that a more restrictive criterion can be obtained.

To find the criterion, we need estimate the rate of $\int_{r_1}^{r_2} r \|\phi'\|^2 dr$ to $\int_{r_1}^{r_2} \|\phi\|^2 dr$,

$$\int_{r_1}^{r_2} r \|\phi'\|^2 dr = \mu \int_{r_1}^{r_2} \|\phi\|^2 dr, \quad (1-54)$$

where the eigenvalue μ is positive definition for $\phi \neq 0$. According to boundary condition Eq.(1-49), ϕ can expand as Fourier series. So the smallest eigenvalue value, namely μ_1 , can be estimated as $\mu_1 > r_1 \pi^2 / (r_2 - r_1)^2$.

Then there is a criterion for stability using relation (1-54), a new stability criterion may be found: the flow is stable if $-(\mu_1 + 1/r_2) < \frac{\xi'}{\Omega - \Omega_s} < 0$ everywhere.

To get this criterion, we introduce an auxiliary function $f(r) = \frac{\xi'}{\Omega - \Omega_s}$, where $f(r)$ is finite at inflection point. We will prove the criterion by two steps. At first, we prove proposition 1: if the velocity profile is subject to $-(\mu_1 + 1/r_2) < f(r) < 0$, then $c_r \neq \Omega_s$.

Proof: Since $-(\mu_1 + 1/r_2) < f(r) < 0$, then

$$-(\mu_1 + 1/r_2) < \frac{\xi'}{\Omega - \Omega_s} \leq \frac{\xi'(\Omega - \Omega_s)}{(\Omega - \Omega_s)^2 + c_i^2}, \quad (1-55)$$

and if $c_r = \Omega_s$ and $1 \leq n$, this yields to

$$\begin{aligned} & \int_{r_1}^{r_2} r \|\phi'\|^2 + \left[\frac{n^2}{r} + \frac{\xi'(\Omega - \Omega_s)}{\|\Omega - c\|^2} \right] \|\phi\|^2 dr \geq \\ & \int_{r_1}^{r_2} \left[(\mu_1 + \frac{1}{r_2}) + \frac{1}{r} + \frac{\xi'}{(\Omega - \Omega_s)} \right] \|\phi\|^2 dr > 0. \end{aligned} \quad (1-56)$$

This contradicts Eq.(1-52). So proposition 1 is proved.

Then, we prove proposition 2: if $-(\mu_1 + 1/r_2) < f(r) < 0$ and $c_r \neq \Omega_s$, there must be $c_i^2 = 0$.

Proof: If $c_i^2 \neq 0$, then multiplying Eq.(1-53) by $(c_r - c_t)/c_i$, where the arbitrary real number c_t does not depend on r , and adding the result to Eq.(1-52), it satisfies

$$\int_{r_1}^{r_2} r \{ \|\phi'\|^2 + \left[\frac{n^2}{r^2} + \frac{\xi'(\Omega - c_t)}{r \|\Omega - c\|^2} \right] \|\phi\|^2 \} dr = 0. \quad (1-57)$$

But the above Eq.(1-57) can not be hold for some special c_t . For example, let $c_t = 2c_r - \Omega_s$, then there is $(\Omega - \Omega_s)(\Omega - c_t) < \|\Omega - c\|^2$, and

$$\frac{\xi'(\Omega - c_t)}{\|\Omega - c\|^2} = f(r) \frac{(\Omega - \Omega_s)(\Omega - c_t)}{\|\Omega - c\|^2} > -(\mu_1 + \frac{1}{r_2}). \quad (1-58)$$

This yields

$$\int_{r_1}^{r_2} \left[r \|\phi'\|^2 + \left(\frac{n^2}{r} + \frac{\xi'(\Omega - c_t)}{\|\Omega - c\|^2} \right) \|\phi\|^2 \right] dr > 0, \quad (1-59)$$

which also contradicts Eq.(1-57). So the second proposition is also proved.

Using 'proposition 1: if $-(\mu_1 + 1/r_2) < f(r) < 0$ then $c_r \neq \Omega_s$ ' and 'proposition 2: if $-(\mu_1 + 1/r_2) < f(r) < 0$ and $c_r \neq \Omega_s$ then $c_i = 0$ ', we find a stability criterion.

Theorem 2: If the velocity profile satisfy $-(\mu_1 + 1/r_2) < f(r) < 0$ everywhere in the flow, it is stable.

This criterion is the analogue of the theorem proved by Sun [19]. Both theorem 1 and theorem 2 here are more restrictive than Rayleigh's theorem for the inviscid rotating flows. The theorems indicate the probability that a vorticity profile with local maximum or minimum would be stable, if it satisfies the stable criteria. Theorem 2 implies that the rotating flow is stable, if the distribution of vorticity is relatively smooth. As shown by Sun [19], the instability of inviscid parallel flows must have vortices concentrated enough. This is also the shear instability in rotating flows. Since several stable criteria for inviscid rotating flows have been obtained, it is convenient to explore the relationship among them, as discussed followed.

The criteria for rotating flow can be applied to parallel flows, given narrow-gap approximation. First, Pedley's criterion is covered by the centrifugal instability criteria. As mentioned above, Pedley [37] considered the stability of two-dimensional flows U in a frame rotating with angular velocity Ω . A criterion is found that instability occurs locally when $2\Omega(2\Omega - U') < 0$, where $U' = dU/dr$ represents radial shear of horizontal velocity. Pedley's criterion, which is recovered by later researches [38, 39], is in essence the special case of Rayleigh's circulation criterion, i.e., $\frac{d}{dr}(\Omega^2 r^4) < 0$ for instability.

Here the proof is briefly given. Considering the narrow-gap approximation $r_2 - r_1 = d \ll r_1$ and the large radii approximation $1/r_1 \rightarrow 0$ in Rayleigh's circulation criterion, there is $\Omega' r \approx -U'$. So $\Phi = d(\Omega^2 r^4)/dr/r^3 = 2\Omega(2\Omega - U') < 0$, which is exactly Pedley's criterion. Thus Pedley's criterion is covered by Rayleigh's circulation criterion. Second, the stable criteria for parallel flows, such as Rayleigh's theorem [1] and Fjrtfot's theorem [4], can be derived from those for rotating flows, given the narrow-gap approximation $r_2 - r_1 = d \ll r_1$ and the large radii approximation $1/r_1 \rightarrow 0$. Following this way, the results of the Taylor-Couette system can also be applied to the plane Couette system [40]. The proof is omitted here, as the approach is trivial too. As pointed out by Sun [19], all of the shear instability criteria for two-dimensional flows are the special cases of Arnol'd's nonlinear criteria [14], which are much more complex yet not widely used. In general, all the known stability criteria for parallel flows (even in a rotating frame) can be derived from the stability criteria for rotating flows.

§ 1.4.4 Discussion

As well known, these two kinds of instabilities are independent with each other. Howard [6, 36, 41] has given an example which is stable to axisymmetric disturbances but unstable to two-dimensional (shear) disturbances. Here another example is given that the flow is unstable to axisymmetric disturbances but stable to two-dimensional disturbances according the stability criteria above. To illuminate this, a simple example is given as $\Omega(r) = 1 - r$ with the vorticity $\xi = 2 - 3r$. As shown in Fig. 1-6, both Ω (solid line) and ξ (dashed line) are plotted within the interval $r_1 \leq r \leq r_2$. It is from Rayleigh's inflection point criterion that the flow is always stable to two dimensional disturbances. While the flow is unstable for the axisymmetric disturbances, if $2/3 < r_1 < 1$ or $2/3 < r_2 < 1$. Then, a shear stable flow may be unstable due to centrifugal instability. Considering that there are three-dimensional disturbances, the flow might be unstable, even it is centrifugal stable and shear stable. This might be the reason why there is no general criterion known for H-G equation when non-axisymmetric disturbances are considered [36].

And the relationship between rotation and stratification is also noted. As "Rayleigh observed that there is an analogy between the stability of rotating flows and the stability of a stratified fluid at rest in a gravitational field" [6], the criteria between them can also be analogy with each other. For the stratified flow with vertical velocity shear, Howard [15] obtained a stability criterion, i.e., the flow is stable if $N^2 > U'^2/4$, where N is known as Brunt-Visl frequency, U is horizontal velocity

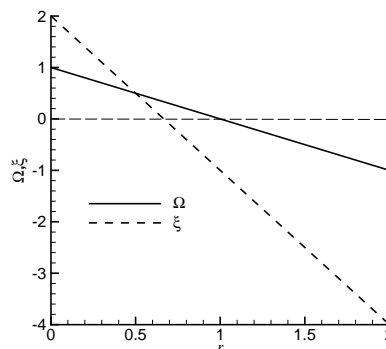


Figure 1-6: Angular velocity Ω (solid line) and corresponding vorticity ξ (dashed line) versus r .

and $U' = dU/dz$ represents vertical shear of horizontal velocity. This criterion is then an analogue of the following criterion by Howard and Gupta [36]: The rotating flow is stable for axisymmetric disturbances if Eq.(1-60) holds,

$$\Phi \geq \frac{1}{4} \left(\frac{dW}{dr} \right)^2, \quad (1-60)$$

where W is the axis velocity, and it vanishes in the pure rotating flows, as in Rayleigh's criteria. Comparing the two stability criteria, the analogues of Φ and dW/dr are N^2 and V' , respectively. Physically the rotating establishes a potential distribution along the ratio, which is denoted by Rayleigh discriminant Φ . Similarly, the stratification establishes a potential distribution along the gravity, which is denoted by Brunt-Väisälä frequency. And the analogue of the radial shear in rotating flow is right the vertical shear in stratified flow. So the criteria between rotation and stratification can also be analogy with each other in this way.

In short, the general stability criterion is obtained for inviscid rotating flow. Then Pedley's criterion is proved to be an special case of Rayleigh's criterion. These results extend Rayleigh's inflection point theorem for curved and rotating flows, and they are analogues of the theorems proved by Fjørtoft and Sun for the two-dimensional inviscid parallel flows.

§ 1.5 General Barotropic Wave

Barotropic waves are widely existed in the flow with shear. However, the general theory for barotropic waves still lacks though the stability of linear waves (e.g. Rossby wave) are always the most concerned. The theory of wave-mean flow interaction points out that the flow is unstable, the disturbed waves can grow by taking energy from the mean flow. However, why the disturbance waves can't take energy from the mean flow in the stable flow is not known. Nevertheless, the general criterion can be great helpful to understand these problems. As Arnol'd's criteria deal with the total energy, they can not provide such kind of information. In this way, a simply linear criterion corresponding to Arnol'd's second nonlinear stability theorem is necessary for considering the stability of waves. It also provides a new way to investigate shear instability. The aim of this short paper is to find such a stability criterion from Rayleigh's equation in normal mode way, through which the shear instability may be understood.

The above criteria would be helpful for understanding the wave-mean flow interaction, especially the Rossby wave-mean flow interaction in barotropic flows. According to the stable criteria, the necessary condition for wave-mean flow interaction can be obtained. And why the disturbed waves can't take energy from the mean flow in the stable flow is revealed. If the flow is stable, there is no wave-mean flow interaction at all.

First, when the velocity profile has no inflection point, then the speeds of barotropic waves $c_r - U \neq 0$. According to Eq.(1-3), $U - c_r > 0$ holds for $U'' < 0$, i.e., the barotropic waves are always west-propagation relative to the mean flow U if the vortex gradient is positive. This extends the west-propagation theory of Rossby waves. And $U - c_r < 0$ holds for $U'' > 0$, i.e., the barotropic waves are always east-propagation relative to the mean flow U if the vortex gradient is negative. Second, when the velocity profile has an inflection point $U_s'' = 0$, the speed of most favorite wave which might have interaction with the mean flow should be $c_r = U_s$. However, the wave speed $c_r \neq U_s$ holds for $-\mu_1 < \frac{U''}{U - U_s} < 0$, as has been pointed out in proposition 1. In short, the waves have no interaction with the mean flows whatever there is an inflection point or not. This conclusion

can be easily generated to the flows in β plane. Thus, the waves have no interaction with the stable flows. This is the reason why the disturbed waves can't take energy from the stably mean flow.

On the other hand, [15] pointed out that c_r of a unstable wave must lie between the minimum and the maximum values of the mean velocity profile. Thus, the unstable wave is stationary relative to the mean flow, and can take energy from the mean flow. So there are wave-mean flow interactions in unstable flows.

In summary, the general stability criterion is obtained for inviscid both parallel and rotating flows. Then Pedley's criterion is proved to be an special case of Rayleigh's criterion. These results extend Rayleigh's inflection point theorem for curved and rotating flows, and they are analogues of the theorems proved by Rayleigh, Tollmien and Fjørtoft for the two-dimensional inviscid parallel flows. Besides, this would intrigue future research on the mechanism of hydrodynamic instability.

Chapter 2 2

Horizontal Convection

§ 2.1 Establishment of Horizontal Convection

§ 2.1.1 Introduction

The abyssal ocean circulation is thought of an important energy conveyor belt, which has great impact to climate change [42, 43, 44]. As former investigators noted the fact that density water sinks by surface cooling at North Atlantic Ocean, this is so called density-driven flow. Horizontal convection, in which the flow is uneven heated at the horizontal surface, was taken as a model of such circulation. However, a novel idea emerges when the ocean energy balance is considered [45, 46, 47]. The horizontal convection become a key model to exam the theories. Two classes of flows are often used. The first one, named as two-basin forcing flows hereafter, has symmetric surface forcing like that of South and North Atlantic Ocean basins. The multiple equilibria and bifurcation phenomena of such flows are often discussed, especially in numerical way [48, 49, 50, 51]. The second one, named as one-basin forcing flows hereafter, has monotone forcing from one side to another like that of North Atlantic Ocean basin. This kind of flow is more conveniently used in the experiments [52, 53, 54].

Some general properties of horizontal convection have been obtained by theoretic studies. Above all, [52] found the 1/5-power laws of Rayleigh number Ra for flow strength Ψ_{\max} and the Nusselt number Nu , which are consistent with experiments and numerical simulations. This 1/5-power law of Ra is generally valid no mater what the flow is steady or non-steady [e.g. 48, 52, 53, 54, 55, 56]. Thus it is useful to consider what the horizontal convection would be as $Ra \rightarrow \infty$. [51] focused on the energy dissipation under the conditions of the viscosity ν and thermal diffusivity κ being lowered to zero with Prandtl number Pr fixed. They proved that the horizontal convection is non-turbulent under certain definition of turbulence. Motivated by above results, [56] claimed Nu is bounded by $Ra^{1/3}$ as $Ra \rightarrow \infty$.

On the other hand, numerical simulations and experiments were also used to find details of the flows. [52, 55] found by both experiment and numerical simulations that the flows are steady and stable in one-basin circulation. Comparing to Rossby's one-basin forcing, [48] studied the multiple equilibria under symmetric two-basin forcing numerically. They also claimed that the flow is always symmetric if only theromal or salt forcing at least for their parameter regimes. If both kinds of forcing are considered, there will be symmetry breaking and even unsteady flows [e.g. 48, 49, 50, 57]. For one-basin circulation, it was thought that horizontal convection must be steady and stable even for

$Ra \rightarrow \infty$, according to Sandstörms's theorem [e.g. 46, 58, 59].

But this scenario seems to be violated in recent investigations. [51] studied the horizontal convection under the symmetric two-basin forcing. The smaller the Prandtl number is, the more unstable the flow is. As the Prandtl number increases to 10, the circulation tends to be a shallow cell. They also obtained the thresholds for the transition from steady flows to unstable and steady flows. These unsteady flows then also were reported in experiments [53]. However, such unsteady convective mixing and turbulent interior motion in the experiments are nonturbulent according to the definition of turbulence [51]. As the plume rises from bottom to top and through the full depth of the tank, this kind of flows are referred as full-penetrating flows. While [54] showed in their experiments a totally different result. The motion of the circulation, though being visible to the naked eye, is vanishingly small. The convection cells, shallow and near the heating surface, are steady and stable. This kind of flows are quite different from those in [53], and they were referred as partial-penetrating flows [54].

Though lots of numerical simulations on the horizontal convection, none of them have obtained such partial-penetrating flow and the onset of such flow needs to reveal yet. The main purpose of this paper is to investigate the partial-penetrating flow by numerical simulation, thus resulting in a more comprehensive view on this issue. The model and the scheme are sketched in § 2.1.2, in which a benchmark solution is included. The establishment of the circulation and the partial-penetrating cell of horizontal convection are depicted in § 2.1.3, with the onset of the partial-penetrating flow being discussed.

§ 2.1.2 Model and Scheme

We consider the the horizontal convection flows within the two-dimensional domain, and Boussinesq approximation is assumed to these flows. The horizontal (y) and vertical (z) regimes are $0 \leq y \leq L$ and $0 \leq z \leq D$, respectively. Similar to [51], the depth D is taken as reference length scale and $A = D/L$ denotes the aspect ratio. We use $A = 1$ in present work, which is consistent with the experiments by [54]. Taking account of nondivergence of velocity filed in Boussinesq approximation, the lagrangian streamfunction Ψ and the corresponding vorticity ω are introduced. The velocity $\vec{u} = (v, w)$, where horizontal velocity $v = \frac{\partial \Psi}{\partial z}$ and vertical velocity $w = -\frac{\partial \Psi}{\partial y}$, respectively. The governing equations [48, 49, 50, 51, 56] in vorticity-streamfunction formulation are

$$\frac{\partial T}{\partial t} + J(\Psi, T) = \left(\frac{\partial^2 T}{\partial y^2} + \frac{\partial^2 T}{\partial z^2} \right) \quad (2-1a)$$

$$\frac{\partial \omega}{\partial t} + J(\Psi, \omega) = -\text{Pr}(\nabla^2 \omega + \text{Ra} \frac{\partial T}{\partial y}) \quad (2-1b)$$

$$\nabla^2 \Psi = -\omega \quad (2-1c)$$

where $J(\Psi, \phi) = \frac{\partial \Psi}{\partial y} \frac{\partial \phi}{\partial z} - \frac{\partial \phi}{\partial y} \frac{\partial \Psi}{\partial z}$ denotes the nonlinear advection term. There are two important dimensionless parameter in Eq.(2-1), i.e. Rayleigh number $\text{Ra} = \alpha_T \Delta T g L^3 / (\kappa \nu)$ and Prandtl number $\text{Pr} = \nu / \kappa$, where g , α_T , ΔT , L , κ and ν are gravity acceleration, thermal expansion coefficient, surface temperature difference, length of horizontal domain, thermal diffusivity and kinematic viscosity, respectively. The surface buoyancy forcing is $T = \sin(\frac{\pi}{2}y)$, so that only one-basin flows instead of symmetric two-basin flows can be obtained.

There are two important quantity describing the circulation, i.e. the non-dimensional streamfunction maximum and the non-dimensional heat flux. The non-dimensional streamfunction maxi-

mum $\Psi_{\max} = \Psi_{\max}^*/\nu$, where Ψ_{\max}^* is the maximum of the dimensional streamfunction. For the non-dimensional heat flux is defined as $f_T = \partial T/\partial z$ at the heated surface.

The above Eq.(2-1) is solved with Arakawa scheme [e.g. 60, 61] and non-uniform grids. Comparing to the other schemes, Arakawa scheme is more accuracy but more expensive, and it has also been applied to horizontal convection flows at high Rayleigh number [62].

To validate the scheme, we calculate the nature convection problem with the resolution of 80×80 meshes. Table 2-1 compares the present solutions with bench mark solutions from [63], who solved the problems using a pseudo-spectral Chebyshev algorithm and [64], who used fourth-order compact finite difference scheme. It is obvious that the our scheme is very accuracy for such flows.

§ 2.1.3 Results

1. the establishment of circulation

Similar to the experiments by [54], we use $A = 1$ for the numeric simulations, the circulations are obtained for $Ra > 10^7$. The dimensionless time $t = t^*/\tau$, where t^* and $\tau = D^2/\kappa$ are the dimensional and the unit scaling times, respectively. A typical value of $t = 1$ is about 80 hours in the dimensional time, given $D = 20\text{ cm}$ and $\kappa = 1.4 \times 10^{-3}\text{ cm}^2/\text{s}$, which are approximate to the values used in the experiments by [53, 54]. According to the flow pattern, the establishment of the circulation can be divided into three stages: (1) startup of circulation, (2) damp of secondary circulation, (3) amplification of primary circulation. The former two stages are relatively short, while the third one is very long. At the end of last stage, the circulation is fully established.

To illuminate this, the circulation of $Pr = 8$ and $Ra = 5 \times 10^8$ is taken as an example. During the first stage, the circulation is established as soon as the surface forcing is superposed (Fig.2-1a). The gradient of horizontal buoyancy drives the water like a lid, so that a very energetic primary circulation ($\Psi_{\max} > 56$) generates (Fig.2-1b), which was also observed by the experimentalist [54]. But this process is much more faster, and soon the secondary circulation emerges below the primary circulation at $t = 3.2 \times 10^{-4}$ (Fig.2-1c). The secondary circulation becomes stronger and stronger, and the primary circulation becomes weaker and weaker. At the end of the stage, the primary

author	Ra	Ψ_{mid}	Ψ_{\max}	$u_{\max}(y)$	$v_{\max}(x)$	Nu
Present	10^6	16.430	16.863	64.47(0.85)	219.17 (0.038)	8.828
[63]	10^6	16.386	16.811	64.83(0.85)	220.56 (0.038)	8.822
[64]	10^6	16.386	16.811	64.83(0.85)	220.57 (0.038)	8.825
Present	10^7	29.586	30.426	146.05(0.886)	687.17 (0.022)	16.535
[63]	10^7	29.361	30.165	148.59(0.879)	699.17 (0.021)	16.523
[64]	10^7	29.356	30.155	148.57(0.879)	699.17 (0.021)	16.511

Table 2-1: Comparison of the bench mark solutions from Le Quéré and [64], $Pr = 0.71$. Ψ_{mid} , Ψ_{\max} are the values in the midpoint and the maximum of streamfunction, respectively. u_{\max} and v_{\max} are the maximum of horizontal and vertical velocity component on the vertical midplane $x = 0.5$ and $y = 0.5$, together with its position y and x , respectively. And Nu is average Nusselt number at the heated wall. The resolution is 80×80 meshes for present results.

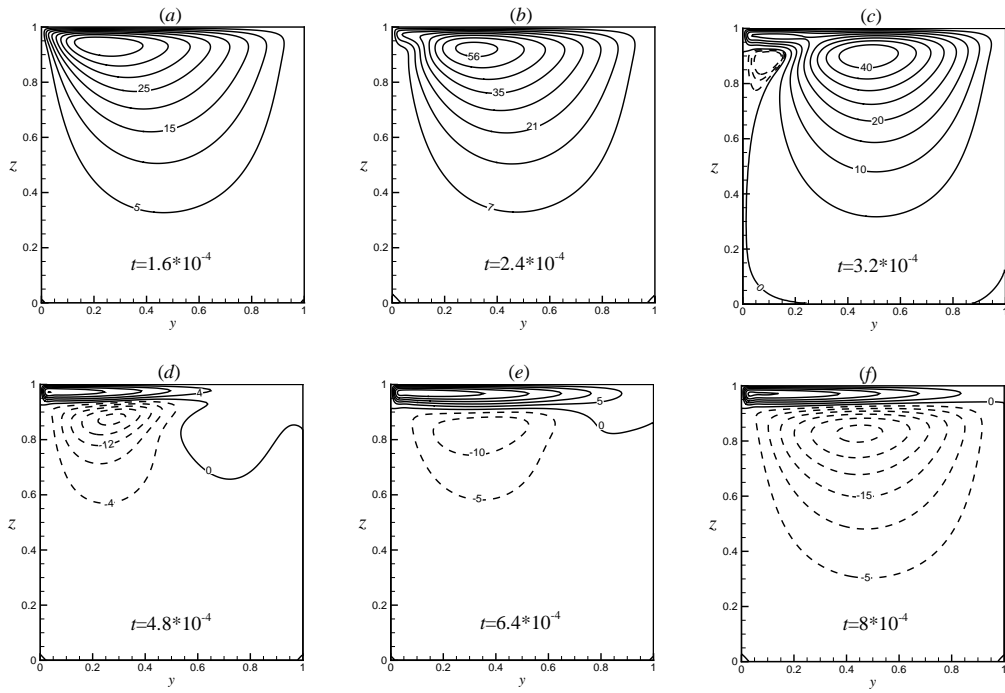


Figure 2-1: Snapshots of the flow fields (streamfunction Ψ), with solid counter curves for $\Psi > 0$ and dashed counter lines for $\Psi < 0$.

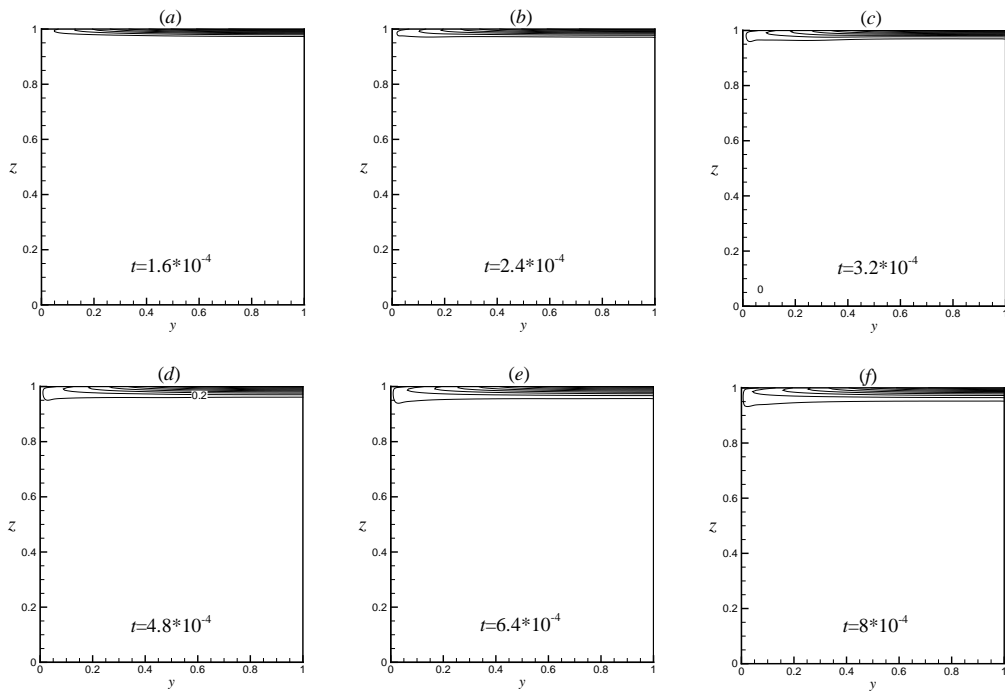


Figure 2-2: Snapshots of the temperature fields corresponding to these in Fig.2-1, with counter intervals being 0.1.

circulation becomes partial-penetrating, the secondary circulation becomes full-penetrating (Fig.2-1f). Meanwhile, the heat conducts from top to bottom along the side walls (Fig.2-2).

Comparing to the first stage, the second one is longer, during which the secondary circulation damps and breaks into several weaker circulations (Fig.2-3). In consequence, the smaller circulations emerges from the bottom one after another. And the flow field fulfills such partial-penetrating circulations, as observed by [54]. The damp of the secondary circulation is a puzzle for the experimentalists, as the corresponding temperature field was not well measured then. Here the temperature fields (Fig.2-4) explains the reason why such full-penetrating circulation can't be maintained. The lack of driven forcing and the viscous friction are the reasons. As in Fig.2-4, there is vanishingly small buoyancy gradient in the secondary circulation, so that it damps down due to viscosity and boundary friction, especially the circulation near the bottom. Meanwhile, the primary circulation covers the convection region, where the horizontal buoyancy gradient is remarkably large.

The last stage is a long and slowly process of approaching to quasi-equilibrium state. The primary circulation is amplified in this stage, and the secondary circulations disappear from the bottom, like their emerging process (Fig.2-6). It is notable that the primary circulation (e.g. the shadowed shallow circulation cell in Fig.2-6) seldom changes during this stage, which implies that the flow near surface approaches to quasi-equilibrium state relatively faster. While the process to quasi-equilibrium state is very slowly near the bottom. Comparing the flow field and temperature field, it is clear that the flow field can't be steady until thermal conduction is balanced.

The above stages have different time scales. The startup stage is the most fast stage, during with the circulations are established within $t = 10^{-3}$ (several minutes in laboratorial time). The

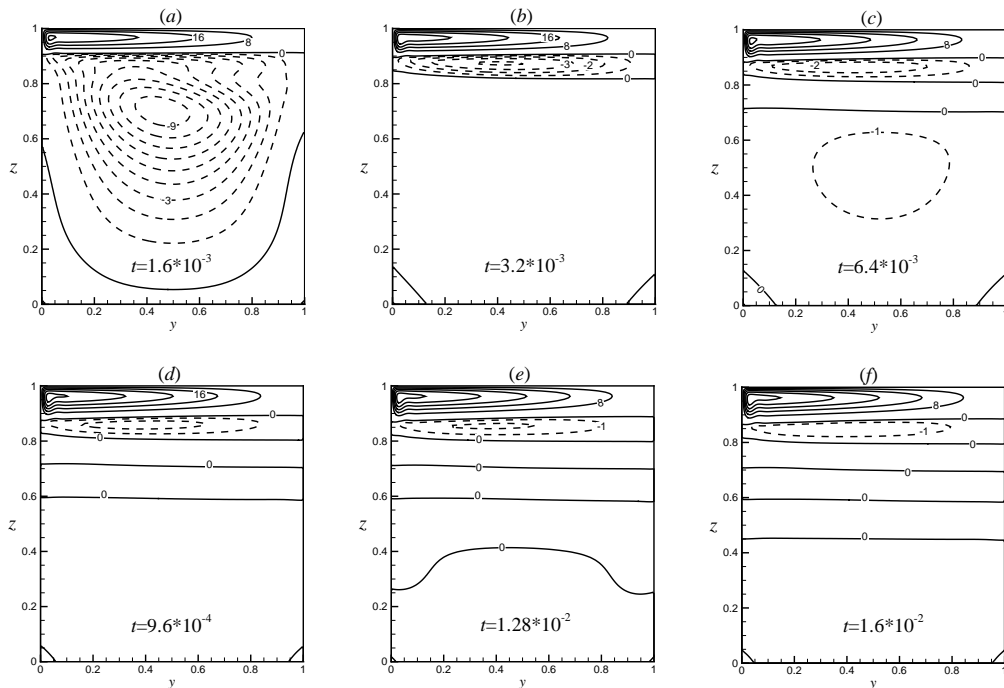


Figure 2-3: Snapshots of the flow fields (streamfunction Ψ), with solid counter curves for $\Psi > 0$ and dashed counter lines for $\Psi < 0$. The counter intervals are 8 and -1 for $\Psi > 0$ and $\Psi < 0$, respectively.

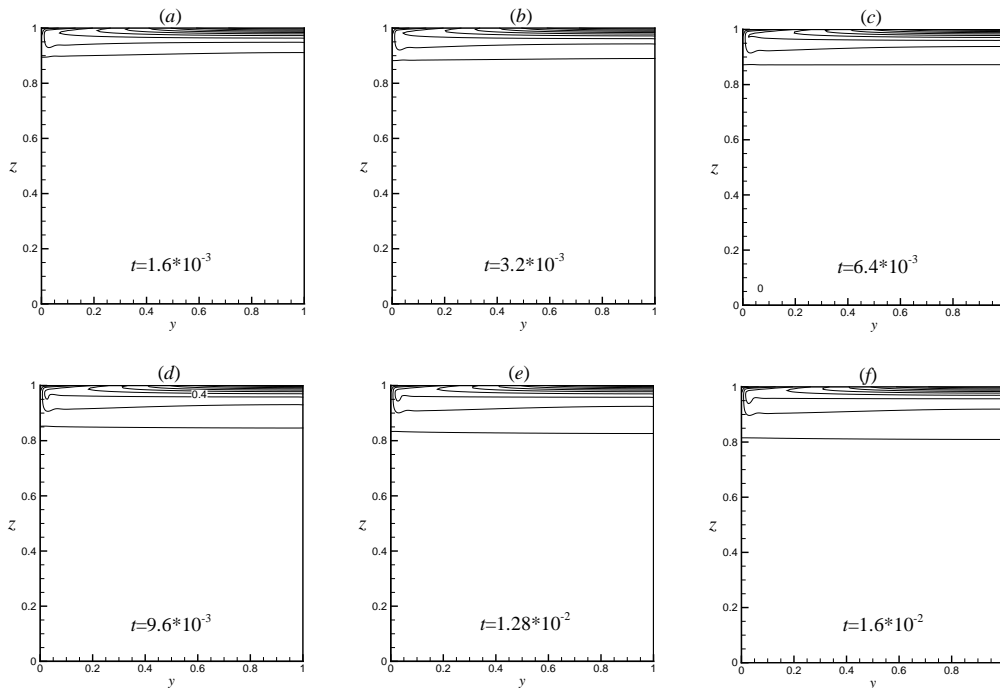


Figure 2-4: Snapshots of the temperature fields corresponding to these in Fig.2-3, with counter intervals being 0.1.

second stage and the last state are time scales of $t = 10^{-2}$ (several hours) and $t = 2.5$ (several days), respectively.

In the following simulations, we use the total kinetic energy E_k and Ψ_{\max} as indexes to oversee the evolution of the circulations, where $E_k = \oint (v^2 + w^2)/2 dy dz$. It is notable that the time approaching to quasi-equilibrium state is very long (about one week) in our numerical simulations, but is remarkably shorter in the experiments [53, 54]. According to the parameters used by [54], not all of the experiments take enough time, so that the circulations are not fully established in some cases. This is more serious in the experiments by [53], where the experiment time of 30 hours is much less than t_e of 200 hours.

The establishment time t_e of the circulation is defined as the time when $d\Psi/dt < 0.001\Psi_{\max}$ holds for whole field. It is found that the partial-penetrating circulation is established very fast, but it takes a very long time for the flow to approach to equilibrium state. Fig.2-7 displays the time evolutions of total kinetic energy E_k and Ψ_{\max} with time t . The circulation is established very fast, and both E_k and Ψ_{\max} reach their 95% of the equilibrium values within $t = 0.05$ (4 hours). In addition, Fig.2-7b agrees well with the experiments (e.g. Fig.2 in [54]), and this fast establishment of the circulation was also noted by [53]. However the total time to get the quasi-equilibrium state is relatively longer, it takes at least $t_e = 2.5$ (200 hours) for the flow being steady in present simulation.

Moreover, the numerical simulation shows that $t_e = 2.5$ is widely valid, at least for all the cases within the regime of $1 \leq \text{Pr} \leq 10$ and $10^7 \leq Ra \leq 10^{10}$. It also implies that the establishment of the circulation is governed by conduction process along the side walls, as t_e is only determined by D and κ . The conclusion of $t_e = 2.5$ is also potentially useful for both numerical simulations and laboratorial experiments.

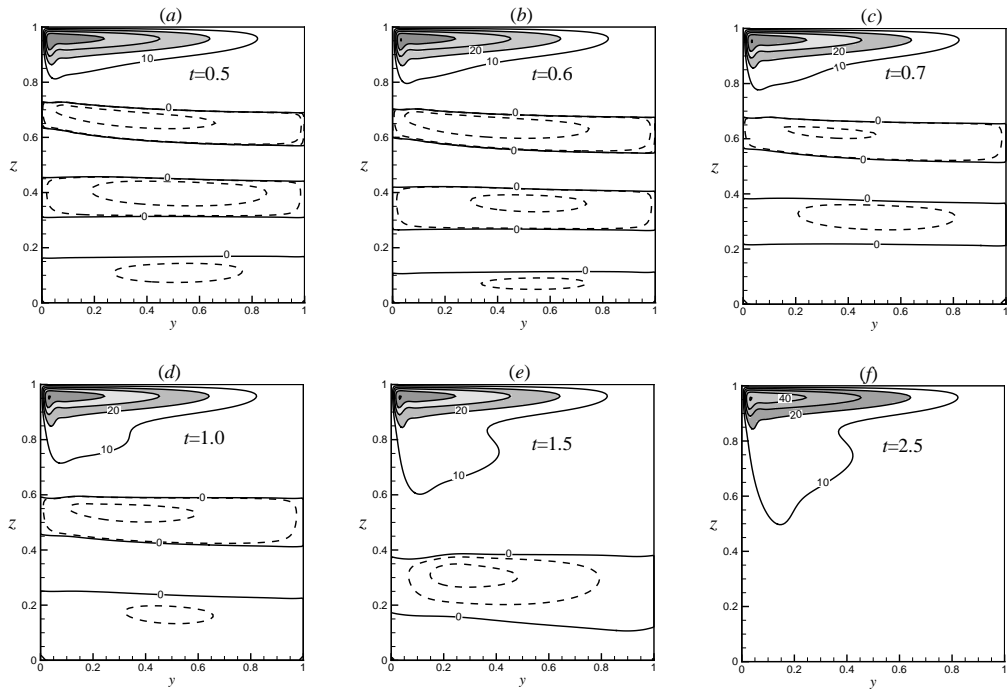


Figure 2-5: Snapshots of the flow fields (streamfunction Ψ) for $Pr = 8$ and $Ra = 5 \times 10^8$, with solid counter curves for $\Psi > 0$ and dashed counter lines for $\Psi < 0$. The counter intervals are 10 for $\Psi > 0$.

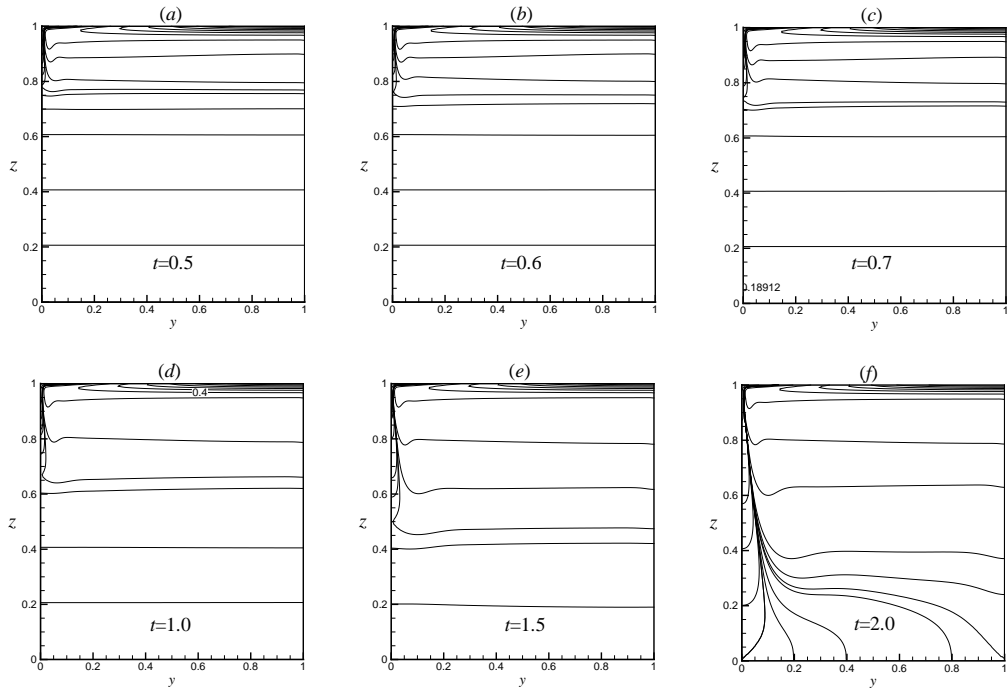


Figure 2-6: Snapshots of the temperature fields corresponding to these in Fig. 2-5.

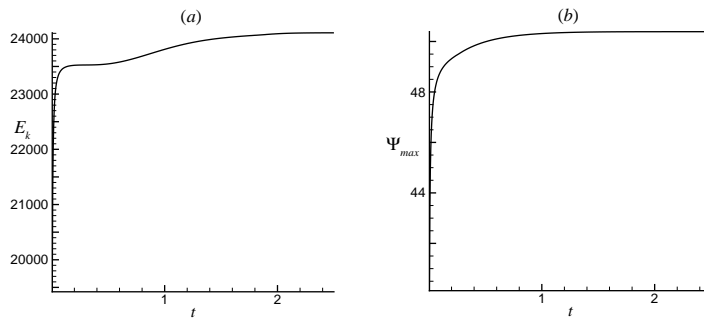


Figure 2-7: The time evolution of the flow field for total kinetic energy E_k (a) and maximum flow Ψ_{max} (b) at $Pr = 8$ and $Ra = 5 \times 10^8$.

The fast established but slowly steadied flow is due to the horizontal evolution of buoyancy (or temperature). It is well known that the horizontal gradient of buoyancy drives the circulation, which can also be known from Eq.(2-1b). Thus the fast establishment of the temperature gradient near the surface makes establishment of the circulation very fast. To illuminate this, the temperature fields of the circulation are shown in Fig.2-6. The horizontal temperature gradient is relatively large near the top surface, but it is relatively to small to be vanished near the bottom. Comparing Fig.2-5a with Fig.2-6a, the main circulation is right within the zone where temperature gradient is remarkably large, so as to the figures at other times. As the time goes on, the main circulation becomes deeper and deeper with the downward propagation of buoyancy gradient. So the slowly heat conduction from the top surface to the bottom makes the establishment of the circulation near bottom to be a long time process. Hence, the depth D of the tank and the thermal diffusivity κ both determinate the establishment time t_e of the circulation. And it is from Fig.2-7 that t_e is 2.5 for the circulation of $Pr = 8$ and $Ra = 5 \times 10^8$.

2. power laws

As the parameters in different ocean global circulation models (OGCM) varies in wide regime [e.g. 47, 65], it is very useful to know how the sensitivity of the results to the parameters. This is also useful when the experimental results are extrapolated to real ocean circulations [53].

Then, the power laws at different Prandtl numbers (e.g. $Pr = 1$, $Pr = 4$, $Pr = 8$ and $Pr = 10$) are calculated to investigate the sensitivities of Nu and Ψ_{max} to Pr . Fig.2-8a and Fig.2-8b show the 1/5-power laws of Ψ_{max} and Nu , respectively. Noting that Ψ_{max} instead of Ψ_{max} and $Ra_p = RaPr^{1/2}$ instead of Ra are in Fig.2-8a, it implies that the flow is dominated by thermal diffusivity κ . The larger Prandtl number is, the stronger the flow is. All the direct numeric simulation (DNS) data at $Pr = 1$, $Pr = 4$, $Pr = 8$ and $Pr = 10$ lie in the line of this power law, $\Psi_{max} = 0.75Ra_p^{1/5}$, where $Ra_p = RaPr^{1/2}$. On the other hand, [54] fitted their experiments data into two different 1/5-power laws. It is amazing that more than half of the experimental data (14/25) by [54], of which the reduced acceleration due to gravity $g' > 2.5 cm/s^2$, lie in this line (right triangles in Fig.2-8a). Taking account that the aspect ratio in DNS is not exact the same as in their experiments, these data are consistent well with each others. Meanwhile, the Nusselt number Nu in DNS lie in two slightly displaced parallel lines, one for $Pr = 1$ and the other for $Pr = 4$, $Pr = 8$ and $Pr = 10$. It seems that Ψ_{max} is more sensitive to Prandtl number than Nusselt number does.

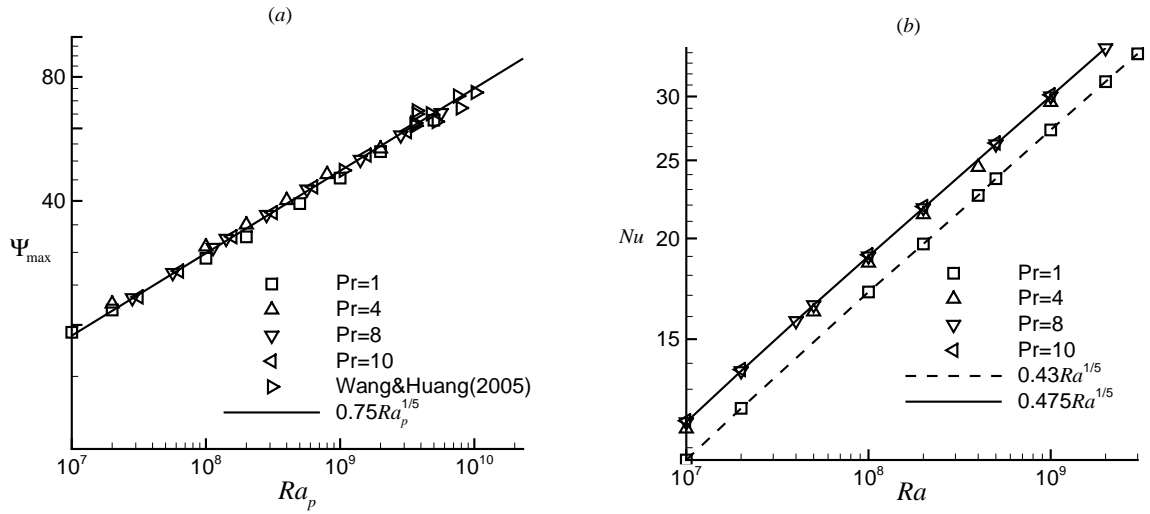


Figure 2-8: The flow streamfunction Ψ_{\max} (a) and the heat flux Nu (b) vs. Rayleigh number, where $Ra_p = RaPr^{1/2}$ in (a).

It is notable that 1/5-power law in Fig.2-8b is something different with that of [56], where Nu is very sensitive to Pr ($0.2 < Pr < 4$). The fact that the power law of Nu is little sensitive to Pr as $Pr > 4$ in Fig.2-8b is consistent with the results of [55]. Here a simple explanation is presented for these results.

Considering the steady state solution of Eq.(2-1) as $Ra \rightarrow \infty$, we obtain the following equation by taking $\Psi = \Psi^*/\kappa$ [48, 52].

$$J(T, \Psi) = \left(\frac{\partial^2 T}{\partial y^2} + \frac{\partial^2 T}{\partial z^2} \right) \quad (2-2a)$$

$$Pr^{-1}J(\nabla^2 \Psi, \Psi) = \left(\frac{\partial^4 \Psi}{\partial y^4} + \frac{\partial^4 \Psi}{\partial z^4} \right) + Ra \frac{\partial T}{\partial y} \quad (2-2b)$$

When $Pr \gg 1$, then the left convection term $Pr^{-1}J(\nabla^2 \Psi, \Psi)$ in Eq.(2-2b) can be ignored, and the buoyancy forcing term $Ra \frac{\partial T}{\partial y}$ balances the viscous term $\nabla^4 \Psi$. In this case, the governing equations is independent of Prandtl number Pr , which is due to [52]. This is the reason why Nu and Ψ_{\max} are little sensitive to Pr for $Pr > 10$ in the numerical simulations by [55]. When Pr is order of 1 or even less than 1, the convection term can not be ignored and Pr plays a role in this case, as obtained by [56]. As $Pr \ll 1$, the buoyancy forcing should be balanced by strong convection at high Ra numbers, which can be seen from Eq.(2-1b). This is also can explain the numerical results by [51], where the flow becomes unsteady and has strong eddy diffusion at $Pr = 0.1$.

§ 2.2 Partial-Penetrating Flow

§ 2.2.1 Introduction

Horizontal convection, in which the water is unevenly heated at the horizontal surface, was taken as a model of abyssal ocean circulation. The circulation, driven by density gradient and referred as thermohaline circulation (THC) at North Atlantic Ocean, is thought of an important energy con-

veyor belt and has great impact to climate change [42, 43, 44]. The horizontal convection become an important model to discuss the ocean energy balance [45, 46, 47]. Unlike the Rayleigh-Bénard convection, the horizontal convection can be set to motion by any small temperature gradient. Moreover, the horizontal convection yields 1/5-power laws of Ra , comparing with the 1/4-power laws in the Rayleigh-Bénard convection.

The 1/5-power laws of Ra for flow strength (streamfunction maximum Ψ_{\max}) and the heat flux (Nusselt number Nu), first found by [52], were later approved by both experiments [e.g. 52, 53, 54] and numerical simulations [e.g. 48, 55, 56, 66]. According to the scaling analysis [48, 52], there is a boundary layer near the surface, which is inverse proportion to 1/5 power of Ra . Both the flow strength and the heat flux are dominated by the scale of boundary-layer. Although this 1/5-power law of Ra is obtained for steady flow, it is still valid even for unsteady flow [e.g. 53].

The unsteady flow in horizontal convection was first found by numerically [51], then was observed in the experiment [53]. This unsteady flow is proved to be non-turbulent for that the energy dissipation turns to zero under the conditions of the viscosity ν and thermal diffusivity κ being lowered to zero with Prandtl number $Pr = \nu/\kappa$ being fixed [51]. Motivated by above investigations, [56] tried to find the bounded of Nu as $Ra \rightarrow \infty$. However, their conclusion of $Nu \leq cRa^{1/3}$ (for some constant c) seems not tight enough as all the numerical simulations yield 1/5-power law.

In a recent experiment, a new flow configuration referred as "parti-penetrating flow" was reported [54]. According to the measurement, the circulation cell is shallow and no longer occupies the whole length of the tank. Though lots of numerical simulations on the horizontal convection, none of them have obtained such partial-penetrating flow. The main reason is that all of the former simulations used free slip condition on the walls [48, 55, 56, 62], the energetic circulation turns to be full-penetrating. While the laboratory experiments always require no slip on the walls [54], the viscous drag slows down the vigorous circulation. Noting that the power law fitted from the experimental data is somehow coarse, this can be improved by numerical simulations. Moreover, the partial-penetrating flow and the onset of such flow needs to reveal too.

The main purpose of this paper is to investigate the partial-penetrating flow and to find a more accurate power law by numerical simulation, thus resulting in a more comprehensive view on this issue. The model and the scheme are sketched in § 2.2.2, in which a benchmark solution is included. The establishment of the circulation and the partial-penetrating cell of horizontal convection are depicted in § 2.2.3, with the onset of the partial-penetrating flow being discussed. Finally § 2.2.4 concludes.

§ 2.2.2 Model and Scheme

We consider the the horizontal convection flows within the two-dimensional domain, and the Boussinesq approximation is assumed to these flows. The horizontal (y) and vertical (z) regimes are $0 \leq y \leq L$ and $0 \leq z \leq D$, respectively. Similar to [52], the depth L is taken as reference length scale and $A = D/L$ denotes the aspect ratio. We use $A = 1$ in present work as [52] did, while $A = 0.675$ is used in the experiments by [54]. Taking account of nondivergence of velocity field in Boussinesq approximation, the lagrangian streamfunction Ψ and the corresponding vorticity ω are introduced. The velocity $\vec{u} = (v, w)$, where horizontal velocity $v = \frac{\partial \Psi}{\partial z}$ and vertical velocity $w = -\frac{\partial \Psi}{\partial y}$, respectively. The governing equations [48, 49, 50, 51, 56] in vorticity-streamfunction formulation are

$$\frac{\partial T}{\partial t} + J(\Psi, T) = \left(\frac{\partial^2 T}{\partial y^2} + \frac{\partial^2 T}{\partial z^2} \right) \quad (2-3a)$$

$$\frac{\partial \omega}{\partial t} + J(\Psi, \omega) = - \text{Pr}(\nabla^2 \omega + \text{Ra} \frac{\partial T}{\partial y}) \quad (2-3b)$$

$$\nabla^2 \Psi = -\omega \quad (2-3c)$$

where $J(\Psi, \phi) = \frac{\partial \Psi}{\partial y} \frac{\partial \phi}{\partial z} - \frac{\partial \phi}{\partial y} \frac{\partial \Psi}{\partial z}$ denotes the nonlinear advection term. There are two important dimensionless parameter in Eq.(2-3), i.e. Rayleigh number $\text{Ra} = \alpha_T \Delta T g L^3 / (\kappa \nu)$ and Prandtl number $\text{Pr} = \nu / \kappa$, where g , α_T , ΔT , L , κ and ν are gravity acceleration, thermal expansion coefficient, surface temperature difference, length of horizontal domain, thermal diffusivity and kinematic viscosity, respectively. The boundary condition is the same with the experiment: the surface buoyancy forcing is $T = \sin(\frac{\pi}{2}y)$, and no slip boundary condition is applied to walls except for surface.

There are two important quantity describing the circulation, i.e. the non-dimensional streamfunction maximum and the non-dimensional heat flux. The non-dimensional streamfunction maximum $\Psi_{\max} = \Psi_{\max}^* / \nu$, where Ψ_{\max}^* is the maximum of the dimensional streamfunction. The non-dimensional heat flux is defined as $f_T = \partial T / \partial z$ on the heated surface. Nusselt number Nu , which is defined here as the maximum of $\partial T / \partial z$ on the top surface. This definition of Nu is something different from the others [e.g. 53, 56].

The above Eq.(2-3) is solved with finite different method in non-uniform grids. Crank-Nicholson scheme and Arakawa scheme [e.g. 60, 61] are applied to discretize the linear and nonlinear terms, respectively. Comparing to the other schemes, Arakawa scheme is more accuracy but more expensive, and it has also been applied to horizontal convection flows at high Rayleigh number [62].

To validate the scheme, we calculate the nature convection problem with the resolution of 80×80 meshes. Table 2-1 compares the present solutions with bench mark solutions from [63], who solved the problems using a pseudo-spectral Chebyshev algorithm and [64], who used fourth-order compact finite difference scheme. It is obvious that the our scheme is very accuracy for such flows.

§ 2.2.3 Results

1. spatial resolution

First, we investigate grid dependency of the solutions to ensure that the numerical simulations are valid. The boundary condition is the same with the experiment: the surface buoyancy forcing is $T = \sin(\frac{\pi}{2}y)$, and no slip boundary condition is applied to walls except for surface. To this purpose, a case of $\text{Ra} = 2 \times 10^8$ and $\text{Pr} = 1$ is calculated with grids of three different resolution, i.e. the horizontal number of meshes $N = 40$, $N = 64$ and $N = 80$. We find that the resolution of grids must be fine enough, otherwise some unphysical time-depend solutions would be obtained.

Fig.2-9a depicts the time evolution of the maximum Ψ_{\max} . The solutions tend to be steady as time $t > 1$ for $N = 64$ and $N = 80$. While it becomes time-dependent for $N = 40$. It implies that some unphysical time-dependent solutions might be obtained if the spatial resolution is not fine enough. To exclude the unphysical time-dependent solutions, the numerical simulations must be obtained with sufficient spatial resolution which depends on the Rayleigh number Ra . As Fig.2-9b shows, the minimal number of horizontal meshes N is to obtain correct results directly proportion to $\text{Ra}^{1/3}$. Taking account of $\text{Ra} \propto L^3$, this means $N \propto L$: the longer L is, the larger N is. To obtain

the physical solutions, N must be within the stable regime in Fig.2-9b. According to our calculations, the flow is still steady and stable for $Ra \leq 10^{10}$.

It is from Fig.2-9b that $\Delta y = L/N = C_R(\kappa\nu)^{1/3}/(\alpha_T\Delta Tg)^{1/3}$, where Δy and $C_R = 10$ are the mesh size in y direction and the coefficient, respectively. The smaller κ and ν are, the smaller the mesh should be. For the molecular kinematic viscosity $\nu = 1.5 \times 10^{-2} \text{ cm}^2/\text{s}$ and thermal diffusivity $\kappa = 1.3 \times 10^{-3} \text{ cm}^2/\text{s}$ in the case of “run 16” by [54], the mesh Δy should be 2.1 mm , which is smaller than Kolmogorov scale $\eta = (\nu^3/\epsilon)^{1/4} = 5.8 \text{ mm}$, where $\epsilon = 2 \times 10^{-4} \text{ cm}^2/\text{s}$ is dissipation rate in the field [54]. So this implies that the mesh should be fine enough to resolute Kolmogorov scale eddies.

The resolution requirement of Δy implies that the bound of L in numerical simulations is about laboratory scale if molecular viscosity and diffusivity are used. And eddy viscosity and diffusivity are required, when the length of ocean scale is considered.

2. the establishment of circulation

Then the circulations are obtained numerically for $Ra > 10^7$. Similar to [51], the dimensionless time $t = t^*/\tau$, where t^* and $\tau = D^2/\kappa$ are the dimensional and the unit scaling times, respectively. A typical value of $t = 1$ is about 80 hours in the dimensional time, given $D = 20 \text{ cm}$ and $\kappa = 1.4 \times 10^{-3} \text{ cm}^2/\text{s}$, which are approximate to the values used in the experiments by [53, 54]. In the following simulations, we use the total kinetic energy E_k and Ψ_{\max} as indexes to oversee the evolution of the circulations, where $E_k = \oint (v^2 + w^2)/2 \, dy \, dz$. It is found that the flow is established very fast, but it takes a very long time for the flow to approach to equilibrium state.

To illuminate this, the circulation of $Pr = 8$ and $Ra = 5 \times 10^8$ is taken as an example. Fig.2-7 displays the time evolutions of total kinetic energy E_k and Ψ_{\max} with time t . The circulation is established very fast, and both E_k and Ψ_{\max} reach their 95% of the equilibrium values within $t = 0.05$ (4 hours). In addition, Fig.2-7b agrees well with the experiments (e.g. Fig.2 in [54]), and this fast establishment of the circulation was also noted by [53]. However the total time to get the quasi-equilibrium state is relatively longer, it takes at least $t_e = 2.5$ (200 hours) for the flow being steady in present simulation. During this process, the flow near the surface is fully established and

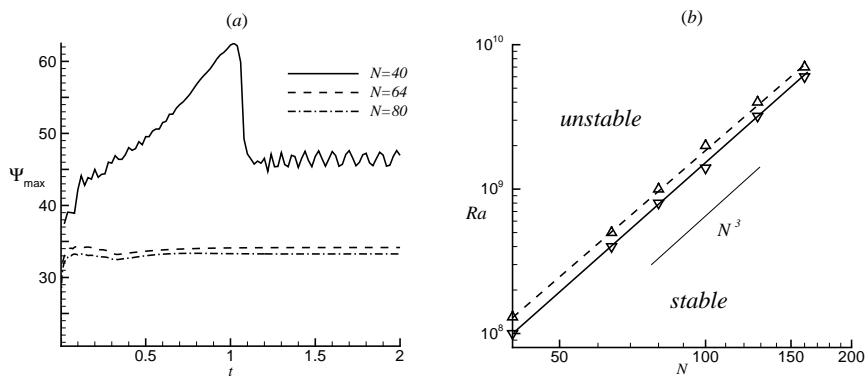


Figure 2-9: (a) The maximum of streamfunction Ψ_{\max} vs time t for $Ra = 2 \times 10^8$. The solid, dashed and dash-dotted curves are solutions with $N = 40$, $N = 64$ and $N = 80$, respectively. (b) The stable and unstable regime on the plot of Rayleigh number Ra vs N .

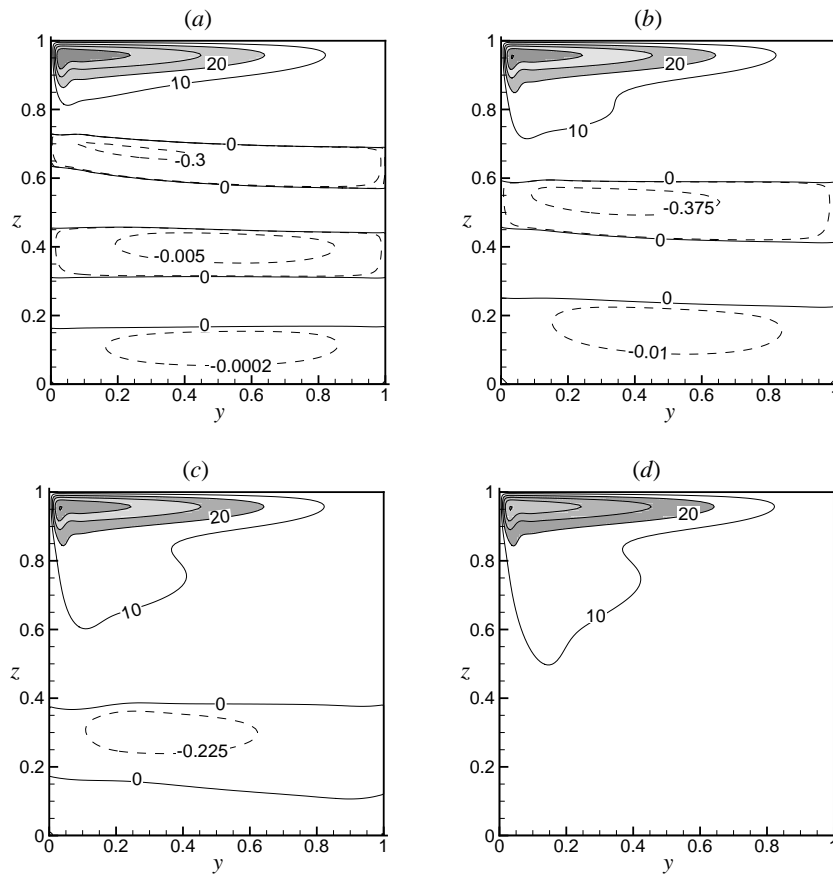


Figure 2-10: The flow fields (streamfunction Ψ) at four different time steps: $t = 0.5$ (a), $t = 1.0$ (b), $t = 1.5$ (c) and $t = 2.5$ (d) at $Pr=8$ and $Ra = 5 \times 10^8$, solid curves for clockwise flow ($\Psi > 0$) and dashed curves for anticlockwise flow ($\Psi < 0$), respectively. The partial-penetrating cells ($\Psi > 20$) are shadowed and the counter intervals are 10 for $\Psi > 0$ in each figures.

approaches to equilibrium state within $t = 1$, as Fig.2-10a and Fig.2-10b show. Meanwhile, there are several very weakly clockwise and anticlockwise circulation cells below the primary circulation cell, which are secondary flows due to the drag by upper primary circulation. These secondary cells were also observed in the experiments by [54]. As the time goes on, the primary circulation cell becomes stronger and larger, and the secondary circulations are weaker and smaller. So that the counter line of $\Psi = 10$ becomes deeper and deeper as shown from Fig.2-10a to Fig.2-10d. Finally, the primary cell fulfills the whole tank at $t = 2.5$ (Fig.2-10d).

Then, the flows within $10^7 \leq Ra \leq 10^{10}$ are calculated. Fig.2-8a shows the 1/5-power law of Ra for Ψ_{\max} at different Prandtl numbers (e.g. $Pr = 1$, $Pr = 4$, $Pr = 8$ and $Pr = 10$). Noting that $Ra_p = RaPr^{1/2}$ instead of Ra are used in Fig.2-8a, it implies that the flow is dominated by thermal diffusivity κ . The larger Prandtl number is, the stronger the flow is. All the direct numeric simulation (DNS) data at $Pr = 1$, $Pr = 4$, $Pr = 8$ and $Pr = 10$ yield,

$$\Psi_{\max} = 0.75Ra_p^{1/5} = 0.75Ra^{1/5}Pr^{1/10} \quad (2-4)$$

On the other hand, [54] fitted their experiments data into two different 1/5-power laws: bigger one for the reduced acceleration due to gravity $g' > 2.5 \text{ cm/s}^2$, the smaller one for $g' < 2.5 \text{ cm/s}^2$. Equation (2-4) is similar to but more accurate than the bigger one obtained by [54]. It is notable that all the experimental data lie around this line (right triangles in Fig.2-8a), as the Prandtl number is considered. Taking account that the aspect ratio in DNS is not exact the same as that in their experiments, these data are consistent well with each others. Fig.2-8b shows the 1/5-power law for Nu . This is consistent with the scaling analysis, i.e. the thermal boundary-layer is inverse proportion to $Ra^{1/5}$. It is obvious that Nu is less sensitive to Pr than that of Ψ_{\max} , so that Nu seldom changes for $Pr > 4$.

3. the partial-penetrating cell

It is notable that the main circulation near the surface is seldom changed during the establishment process, especially the close circulation cell shadowed in Fig.2-10. As this cell is shallow and the circulation is only near the surface, it is referred as the "partial-penetrating cell" after [54]. For example, the shadowed cell height is about 1/6 of the total depth in Fig.2-10, so that the whole cell is within the boundary-layer near the surface. This kind of flow also exist in other Rayleigh numbers, where the shallow and close cells like that in Fig.2-10.

An objective definition of "partial-penetrating cell" is more convenient for further discussion. In present investigation, the penetrating depth of the cell D_c is defined as the depth of a close circulation cell, which contains 60% of the total amount. Here the concept of partial-penetrating cell has such meanings: (1) above all, the close circulation cell is very shallow comparing to its width, so that D_c is within the boundary-layer near the surface, (2) consequently, the close cell is seldom affected by the bottom boundary, (3) moreover, the flow in close circulation cell is dominant of the main circulation, e.g., the flow rate in the shallow cell is about 60% of the total amount (e.g. $\Psi_c = 20$ in Fig.2-10). On the contrary, "the full-penetrating circulation" is referred to the circulation takes whole depth of the tank hereinafter.

Using the above definition, the shadowed cell in Fig.2-10 is the partial-penetrating cell. First, it is obvious that the shadowed cell satisfies conditions (1) and (3). Second, the close cell is seldom affected by the bottom boundary. To illuminate this, we descend the depth of the water tank (or equally descending aspect ratio A). Fig.2-11 clear depicts that the partial-penetrating part is little

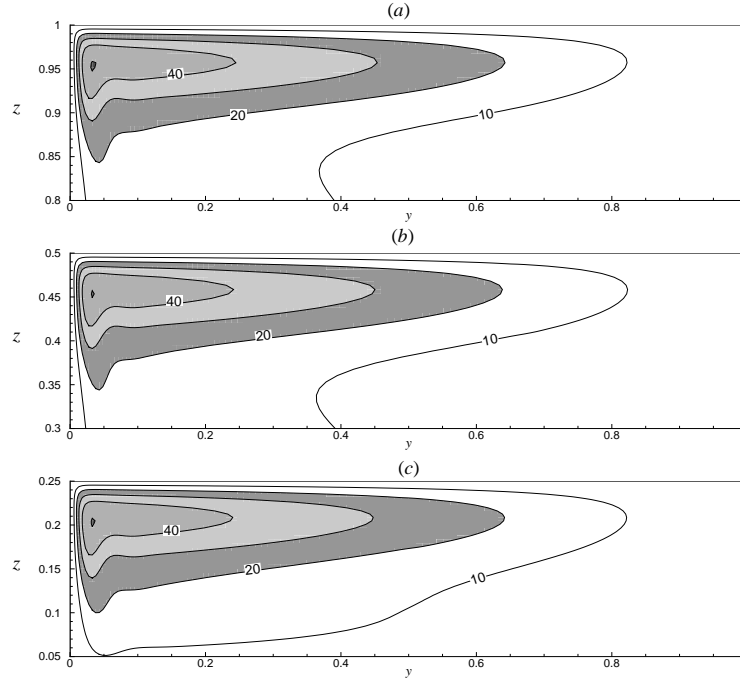


Figure 2-11: The flow fields (streamfunction Ψ) near the forcing surface of three respective aspect ratios: $A = 1$ (a), $A = 0.5$ (b) and $A = 0.25$ (c) at $Pr=8$ and $Ra = 5 \times 10^8$. The partial-penetrating cells are shadowed and the counter intervals are 10 in each figures.

sensitive to bottom, if the depth of the tank is large enough ($D_c < D < 2D_c$ in Fig.2-11c). It may also be noted that the flow in Fig.2-11c is very similar to the flow field near the surface ($0.75 \leq z \leq 1$) in Fig.2-10a. For that at that time in Fig.2-10a, the boundary of main circulation $\Psi = 0$ is about $z = 0.75$, hence the flow near the top is approximation of the case in Fig.2-11c. This also implies that the shadowed cell in Fig.2-10 is partial-penetrating.

As the partial-penetrating cell is near the forcing surface, it is quite independent of the flows in the middle and the bottom. First, the partial-penetrating cell changes little even when the full-penetrating circulation emerges in Fig.2-10c, d. Second, In addition, Fig.2-11 clear depicts that the partial-penetrating part is little sensitive to bottom, if the depth is large enough. Thus the partial-penetrating cell ($\Psi > \Psi_c$) is unchanged given the tank is deep enough. On the contrary, the full-penetrating part is very sensitive to the bottom, as the flow this part of flow approaches to the bottom.

4. the constrain for partial-penetrating flow

However, not all the flows have partial-penetrating cells like that in Fig.2-10, e.g. the flow at $Pr=1$ and $Ra = 5 \times 10^8$ in Fig.2-12. It is obvious that the circulation of $Pr = 1$, which is mainly full-penetrating, is more deep comparing to $Pr = 8$. So only the close circulation cell for $\Psi > 35$ is shallow enough, and it is about $1/6$ of the total depth (Fig.2-12). While this shallow cell is neither dominant in the whole circulation nor immune to the changes of bottom boundary, which is shown in Fig.2-13. Even this small shallow cell is sensitive to the bottom boundary. Compare this with Fig.2-11, the close circulation cell for $\Psi > 35$ is not like the partial-penetrating cell.

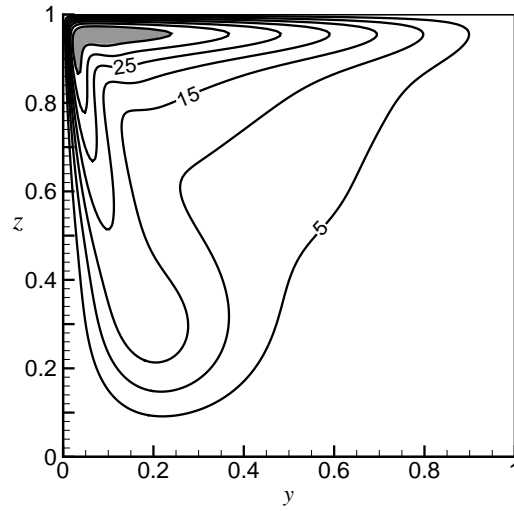


Figure 2-12: The flow fields (streamfunction Ψ) for full-penetrating flow at $Pr=1$ and $Ra = 5 \times 10^8$. The counter interval is 5, and $\Psi > 35$ is shadowed.

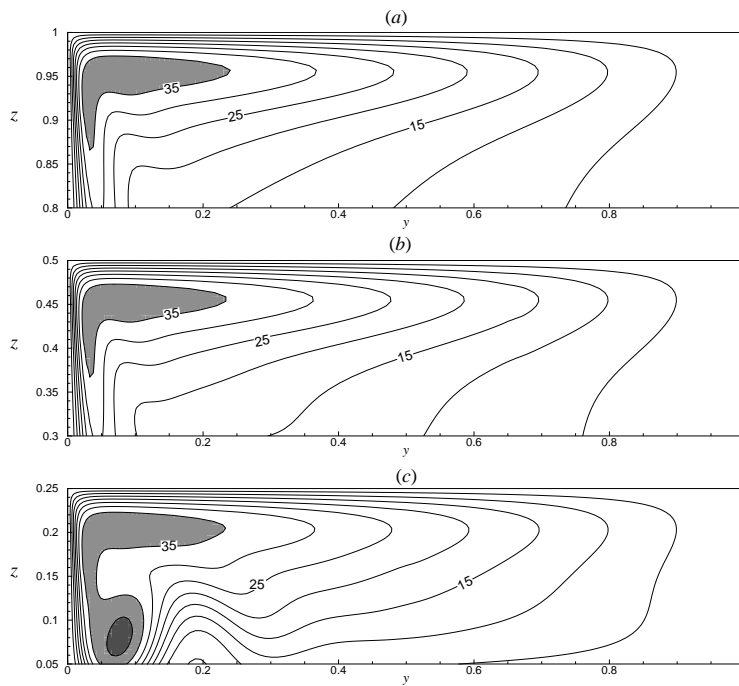


Figure 2-13: The flow fields (streamfunction Ψ) near the forcing surface of three respective aspect ratios: $A = 1$ (a), $A = 0.5$ (b) and $A = 0.25$ (c) at $Pr=1$ and $Ra = 5 \times 10^8$. The streamfunction $\Psi > 35$ are shadowed and the counter intervals are 5 in each figures.

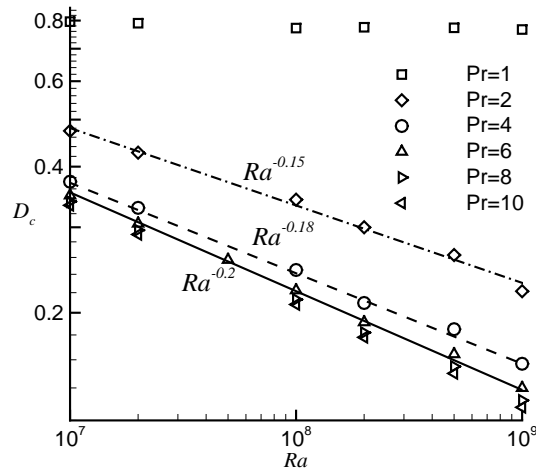


Figure 2-14: D_c vs. Ra . The solid, dashed and dash dotted lines are power laws of Ra respectively for D_c at $Pr = 6$, $Pr = 4$ and $Pr = 2$.

Then a new problem emerges. As there might be full-penetrating flows, what's the constrain for the partial-penetrating flow? To investigate this, D_c is employed as an index of partial-penetrating flow according to the above definition. If D_c satisfies $-1/5$ power law of Ra , then the flow is within the boundary-layer and the flow is partial-penetrating, for that the boundary-layer satisfies $-1/5$ power law of Ra [48, 52, 53]. Else if D_c does not satisfy $-1/5$ power law of Ra , then the flow is full-penetrating. Thus, according to the power law for D_c , the flow can be referred as either partial-penetrating or full-penetrating.

In fact, the critical parameter governing the exitance of partial-penetrating cell is Prandtl number Pr . The larger the Prandtl number is, the more obvious the partial-penetrating cell is. It is from Fig.2-14 that the smaller Pr is, the bigger or deeper D_c is. Only for the flows at $Pr \geq 6$, does D_c satisfy the $-1/5$ power law of Ra . D_c seldom changes with Ra even for the flows at $Pr = 1$.

It is notable that partial-penetrating flows exist for $Pr \geq 6$, this can be understood from scale analysis [48, 52]. When $Pr \gg 1$, then the left convection term $Pr^{-1}J(\nabla^2\Psi, \Psi)$ in Eq.(2-3b) can be ignored, and the buoyancy forcing term $Ra\frac{\partial T}{\partial y}$ balances the viscous term $\nabla^4\Psi$. In this case, the governing equations is independent of Pr and the boundary layer is inverse proportion to $Ra^{1/5}$. When Pr is order of 1 or even less than 1, the convection term can not be ignored. So that the strong convection is full-penetrating as depicted in Fig.2-12.

In words, it is Pr that governs the flow pattern. When $Pr \geq 6$, the flow is partial-penetrating. While $Pr \leq 4$, the flow is full-penetrating.

§ 2.2.4 Conclusion

The experiments of horizontal convection in a rectangle cavity are simulated numerically. The simulations agree well with the experimental data, and a more extensive $1/5$ -power law of Ra is obtained by fitting the DNS data. The partial-penetrating flows are revisited by numerical simulations. It is Pr that governs the the existent of the partial-penetrating flow. When $Pr \geq 6$, the flow is partial-penetrating. While $Pr \leq 4$, the flow is full-penetrating.

§ 2.3 Power Laws

§ 2.3.1 Introduction

The power laws in horizontal convection is one of the fundamental for understanding the flows. It is reported from [52] and [54] that the flow strength (the maximum of stream function Ψ_{max}) is always increasing with $Ra^{1/5}$. However, the flux of the flow can't be measured very accuracy, and the parameters are bounded within $Ra < 10^{10}$ due to experimental inconvenientness. Moreover, the numerical simulations of [51] ($0.1 < Pr < 10$), [56] ($0.2 < Pr < 4$) can obtain both the flow strength and the heat flux. But the Rayleigh number Ra used in numerical simulation are lower than the maximum value used in the experiments. It is found that $\Psi_{max} \sim Ra^{1/4}$ to $\Psi_{max} \sim Ra^{1/3}$, and $Nu \propto Ra^{1/5}$ [56], which is consist with the results by [62] at $Pr = 10$. The flow strength depends continuously to Ra from $\Psi_{max} \propto Ra$ to $\Psi_{max} \propto Ra^{1/3}$.

On the other hand, Paparella and Young (2002) [51] have claimed that the flux trends to zero as thermal diffusion trends to zero and Pr is fixed. Besides, Siggers et. al (2004) obtained that the maximum of heat flux Nu is proper to $Ra^{1/3}$, which is not supported by their numerical simulations. Then two possibilities are suggested. First, their theory is not accuracy. Second, the numerical simulation is not accuracy.

Motivated by the above problem, the power laws of horizontal convection is investigated. Similar to the previous investigations, we consider the horizontal convection flows within the two-dimensional domain with aspect ratio $A = 0.1$. In the following parts, the flows at very high Rayleigh numbers are simulated, and the power laws are obtained by fitting the individual result.

§ 2.3.2 Results

When the Rayleigh number is relatively lower, the flow is weak and the heat transportation is dominated by heat conduction [48, 56]. As the Rayleigh number increases, the thermal convection enhances to balance the surface heat flux. Fig.2-15 shows the stream function and temperature field of $Ra = 10^7$. There is a weak upwelling flow in the center and two strong downwelling flow in the two sidewalls, which are driven by central heating and sidewall cooling. Accordingly, the temperature field deforms it horizontal isothermal lines as the convection. There is a warm tongue (shaded in

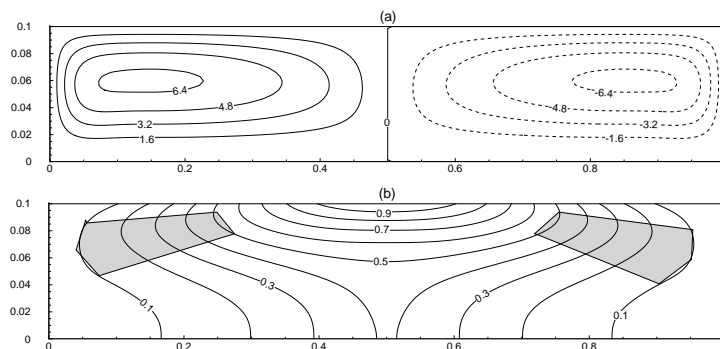


Figure 2-15: The flow stream function (a) and temperature field (b) of $Ra = 10^7$. It is steady and stable and symmetric with middle plume forcing, solid and dashed curves for positive and negative values, respectively.

Fig.2-15b), which is due to the vigorous central flow near the top surface and the central flow near the bottom bringing the cold water to the middle. For example, the isothermal line of $T = 0.3$ extends to cold water near top but but to warm water near bottom.

When the Rayleigh number is higher, the flow field is more complex. Fig.2-16 depicts the flow field and temperature field of $Ra = 10^{10}$, which are something different from the flow of $Ra = 10^7$. First, the downwelling flow departs into two separate parts: one descends the middle, the other can descend to the bottom. Thus there are two vortex centers in the main circulation as in Fig.2-16a. Besides, there is a reverse secondary circulation along the bottom near the sidewalls (1/10 departs from sidewall), which have no mass interchange with the main circulations (dead water). Consequently, they have no contribution to the main thermal convection. Similar to Fig.2-15a, the isothermal lines are concentrated and horizontal in the center. Moreover, the isothermal lines in Fig.2-16b shows there are a temperature boundary layer and a thermocline near the surface. In total, the flow field are dominated by cold water, where $T < 0.2$ except for the boundary layer. This contracts to the Fig.2-15b.

Compare the temperature fields in Fig.2-15b and in Fig.2-16b, the temperature boundary emerges near the top surface as the increase of Ra. The temperature is homogenous in the middle and bottom, except for near the sidewalls. The stable stratification also emerges during this process. It is horizontal temperature gradient that driven the surface circulation, which can be seen from the flow filed. However, the bottom circulations are dominated by kinetic adjustment, which has nothing to do with temperature distribution.

§ 2.3.3 Power laws

The above investigation have obtained the flow pattern of two different Rayleigh numbers. The general properties of the horizontal flows are addressed here, especially for the sensitivity of Ra. To this purpose, the power laws for flow strength and heat flux are calculated.

First, the flow strength vs. Ra is investigated, which is the main parameter of intensity in the thermohaline circulation. It is from Fig.2-17a that the flow strength Ψ_{max} is linear proper to Ra as $Ra < 10^6$, and that Ψ_{max} is 1/5-power proper to Ra as $Ra > 10^9$, between is the transition regime.

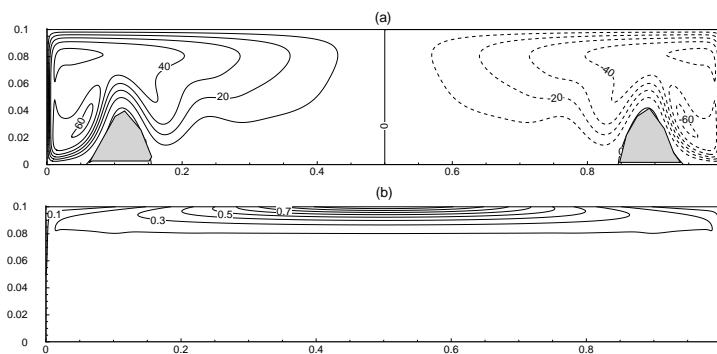


Figure 2-16: The flow stream function (a) and temperature field (b) of $Ra = 10^{10}$. It is steady and stable and symmetric with middle plume forcing, solid and dashed curves for positive and negative values, respectively.

The power law of Ra at high Rayleigh number is,

$$\Psi_{max} = 0.62Ra^{1/5}. \tag{2-5}$$

Similar to the numerical simulation by Siggers et al (2004), $\Psi_{max} \sim Ra^{1/4}$ to $\Psi_{max} \sim Ra^{1/3}$ as $10^8 < Ra < 10^9$. But there is an obvious 1/5-power law as Rayleigh number is higher enough, which implies that this 1/5-power law is valid only at relatively higher Ra. The power law obtained by Siggers et al (2004) is only valid for transition regime.

Second, the power law for heat flux is also studied. As in Fig.2-17b, the heat flux is seldom changed as the increase of Ra. In fact, the heat flux is dominated by heat conduction in this regime [48, 56]. However, this changes to convection dominance as Ra larger than a critical value $Ra \simeq 10^5$, and Nu increases quickly as Ra . Then, a 1/5-power law emerges as $Ra > 10^8$,

$$Nu = 0.75Ra^{1/5}. \tag{2-6}$$

Similar to the numerical simulation by Siggers et al (2004), there is no 1/3-power law regime in the simulations, though Ra is much larger here. The simulations supports their first hypothesis that the theory is overestimation to the heat flux. According to the analysis by Rossby [52], and Quon [48], the thickness of temperature boundary layer is proper to 1/5-power of Ra, which implies $Nu \sim Ra^{1/5}$. Compare the power laws for Ψ_{max} and Nu , there are always three regimes: linear regime, transition regime and 1/5-power regime. However, the transition from one regime to another is not synchronous for Ψ_{max} and Nu , where the transition for heat flux is leading than for the flow streamfunction.

§ 2.3.4 Summary

In summary, the horizontal convection at high Rayleigh number in a rectangle cavity with aspect ratio of 1 : 10 is numerically simulated. According to the results within the regime of $10^4 < Ra < 10^{11}$, three continues regimes are obtained: linear regime ($10^4 < Ra < 10^6$), transition regime ($10^6 < Ra < 10^8$) and 1/5-power law regime ($10^8 < Ra < 10^{11}$). For the flow strength, a 1/3-power

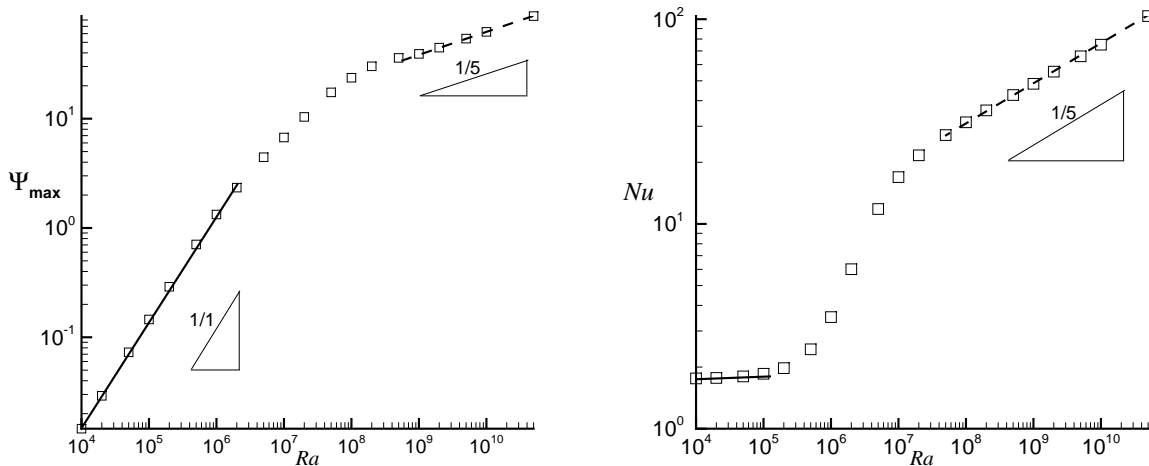


Figure 2-17: The flow streamfunction Ψ_{max} (a) and heat flux (b) vs. Ra.

law of Ra is fitted when Ra is not high enough ($10^7 < Ra < 10^8$). However, a 1/5-power law is obtained as Ra is high enough ($10^8 < Ra < 10^{11}$). The 1/5-power law confirms Rossby's analysis and implies that 1/3-power law of Ra for Nusselt number by Siggers et al. is over estimation.

§ 2.4 Onset of Instability

§ 2.4.1 Introduction

Horizontal convection, in which the water is unevenly heated at the horizontal surface, was taken as a model of abyssal ocean circulation. As the abyssal ocean circulation plays an important role in climate change, the horizontal convection has intensively been explored in recent years [51, 53, 54]. It can be set to motion by any small temperature gradient, unlike the Rayleigh-Bénard convection. But similar to Rayleigh-Bénard convection, the horizontal convection may be unsteady at high Rayleigh numbers Ra . There is a critical Rayleigh number Ra_c , and the steady flow is unstable and becomes unsteady when $Ra > Ra_c$. The unsteady flow in horizontal convection was first found by numerical simulation [51], then was observed in the experiment at $Ra > 10^{12}$ [53]. This unsteady flow is proved to be non-turbulent even as $Ra \rightarrow \infty$, though the flow field seems to be chaotic [51]. The investigation on the unsteady horizontal convection flow is relatively less, except for [51, 53, 67]. However, they have mainly focused on how the turbulent plume maintains a stable stratified circulation. Yet how the horizontal convection turned to be unsteady remains an elusive problem.

To understand this problem, both Ra_c for the onset of unsteady flow and instability mechanism are of vital. Paparella and Young [51] found $Ra_c \approx 2 \times 10^8$ at $Pr = 1$ in their simulations, which is significantly smaller than others' results. For example, Rossby (1965), Wang and Huang (2005) found the flow is steady and stable for $Ra < 5 \times 10^8$ in their experiments [52, 54]. Yet some other numerical simulations [55, 56, 62] have not found unsteady flows for $Ra < 10^9$. Paparella and Young [51] explained this difference as: (i) lower aspect ratio ($H/L = 1/4$) than the experiments and (ii) middle plume forcing instead of sidewall plume forcing in the experiments. Both may lead to destabilization of the flow at lower Rayleigh numbers. However, their hypotheses have not been intensely investigated. According to a recent investigation, the flow is still stable for $Ra < 10^{11}$ even at a much lower aspect ratio ($H/L = 1/10$) [68]. Thus, it maybe the middle plume forcing that leads to destabilization at lower Rayleigh numbers.

Our interest here is to verify their second hypotheses. Is the flow with middle plume forcing less stable than the sidewall plume forcing? How the instability occurs? To investigate these problems, more accurate numerical prediction of Ra_c is need for both forcing cases, for the spatial resolution of simulation is very coarse used (e.g. 128×32 meshes are used in [51]). Then the flow field under both middle and sidewall plume forcings are compared, which leads to an affirmative answer of the above problem.

Similar to the previous investigations, we consider the horizontal convection flows within the two-dimensional domain, and the Boussinesq approximation is assumed to be valid for these flows. As shown in Fig.2-18, the horizontal (y) and vertical (z) regimes are $0 \leq y \leq L$ and $0 \leq z \leq H$, respectively. Similar to [52], the depth L is taken as reference length scale and $A = H/L = 1/4$ denotes the aspect ratio. Taking account of nondivergence of velocity field in Boussinesq approximation, the Lagrangian streamfunction Ψ and the corresponding vorticity ω are introduced. The velocity $\vec{u} = (v, w)$, where horizontal velocity $v = \frac{\partial \Psi}{\partial z}$ and vertical velocity $w = -\frac{\partial \Psi}{\partial y}$, respectively. The governing equations in vorticity-streamfunction formulation are [48, 51, 56]:

$$\frac{\partial T}{\partial t} + J(\Psi, T) = \left(\frac{\partial^2 T}{\partial y^2} + \frac{\partial^2 T}{\partial z^2} \right) \quad (2-7a)$$

$$\frac{\partial \omega}{\partial t} + J(\Psi, \omega) = -\text{Pr}(\nabla^2 \omega + \text{Ra} \frac{\partial T}{\partial y}) \quad (2-7b)$$

$$\nabla^2 \Psi = -\omega \quad (2-7c)$$

where $J(\Psi, \phi) = \frac{\partial \Psi}{\partial y} \frac{\partial \phi}{\partial z} - \frac{\partial \phi}{\partial y} \frac{\partial \Psi}{\partial z}$ denotes the nonlinear advection term. There are two important dimensionless parameter in Eq.(2-7), i.e. Rayleigh number $\text{Ra} = \alpha_T \Delta T g L^3 / (\kappa \nu)$ and Prandtl number $\text{Pr} = \nu / \kappa$, where g , α_T , ΔT , L , κ and ν are gravity acceleration, thermal expansion coefficient, surface temperature difference, length of horizontal domain, thermal diffusivity and kinematic viscosity, respectively. Alternatively, Paparella and Youngs used vertical length H as length scale, so $\text{Ra} = 64 \text{Ra}_H$, where Ra_H is the vertical Rayleigh number by using vertical length H as unit [51].

More specifically, we consider the horizontal convection in a rectangle tank at $\text{Pr} = 1$. The tank has same velocity boundary condition as that in [51], i.e. free slip and no stress at the walls. In addition, two different surface forcings are used, which are central symmetric. One is middle plume forcing as $T = [1 + \cos(2\pi y)]/2$ [51], the other is sidewall plume forcing as $T = [1 - \cos(2\pi y)]/2$ [48, 68]. Comparing these with one cell forcing $T = \cos(\pi y/2)$ [55], there are two symmetric cells in the flow field under such forcings (e.g. Fig.2-18 and Fig.2-24), when the flow is symmetrically steady and stable. In addition, the middle plume forcing in the left cell is the same with the sidewall plume forcing in the right cell (see Fig.2-18 behind). Thus in the steady flows, both forcings will lead to the same flow patterns except for a position shift, which is proved by the following investigation.

There are two important quantity describing the circulation, i.e. the non-dimensional streamfunction maximum and the non-dimensional heat flux. The non-dimensional streamfunction maximum $\Psi_{\max} = \Psi_{\max}^* / \nu$, where Ψ_{\max}^* is the maximum of the dimensional streamfunction.

The above Eq.(2-7) is solved with finite different method in non-uniform grids. Crank-Nicholson scheme and Arakawa scheme [e.g. 60, 61] are applied to discretize the linear and nonlinear terms, respectively. Comparing to the other schemes, Arakawa scheme is more accuract but more expensive, and it has also been applied to horizontal convection flows at high Rayleigh number [62, 68]. Table 2-1 shows the validation of the scheme with nature convection problem. A fine spatial resolution mesh of 512×128 is used to eliminate numerical instability.

§ 2.4.2 Results

First, the middle plume forcing is considered, which is steady and stable for $\text{Ra} < 5.5 \times 10^8$. Fig.2-18 shows the flow field (a) and temperature field (b) of $\text{Ra} = 5 \times 10^8$ with $\Psi_{\max} = 59.83$, in which the flow is symmetric, steady and stable. In this case, the center line symmetrically separates the flow field into two parts, like a free slip wall. There is a vigorous downward jet in the center of tank corresponding to the middle plume forcing (Fig.2-18a), where the vertical velocity field has a minimum of $w = -2513$ (Fig.2-19b). The center jet leads to the clockwise and anticlockwise plume cells in the left and right part of tank, respectively. In the left circulation cell, the flow sinks quickly along the center line and upwells clockwise along the left side wall with relatively slower speed, which can be also seen from the vertical velocity of the flow (Fig.2-19). Besides, there are two horizontal jets respectively near top and bottom walls in the left circulation cell (Fig.2-19a). Totally, there are 2 horizontal jets near wall and a vertical jet at the center in each cell. Contract to the flow field, the

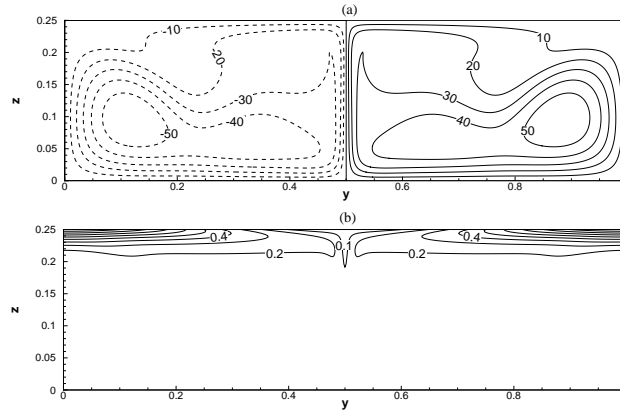


Figure 2-18: The flow stream function (a) and temperature field (b) of $Ra = 5 \times 10^8$. It is steady and stable and symmetric with middle plume forcing, solid and dashed curves for positive and negative values, respectively.

temperature field is very simple. An obvious boundary layer exists near the surface in temperature field, which leads to a $1/5$ -power law of Ra for heat flux [e.g. 48, 52, 56]. And below the temperature boundary layer, the temperature is almost homogeneous due to the convection. Thus there is a very strong stratification near the surface ($\partial T/\partial z \sim Ra^{1/5}$) but a very weak stratification in other region ($\partial T/\partial z \sim 0$). As the above case is stable, so the critical Rayleigh number must be larger than 5×10^8 , which is significantly larger than the value obtained before [51].

To find the critical Rayleigh number Ra_c , the growth rate of perturbation $\phi(t)$ is calculated numerically. And $\phi(t)$ is assumed to satisfy $\phi(t) = e^{\sigma t} \phi(0)$, where $\sigma = \sigma_r + i\sigma_i$ is the complex growth rate of disturbance. It is found that the onset of unsteady flow is at $Ra_c = 5.5377 \times 10^8$, as shown in Fig.2-20. For $Ra = 5.53 \times 10^8$, the flow is stable and the growth rate is approximately $\sigma_r = -0.12$. But the flow is unstable and the growth rate is approximately $\sigma_r = 0.03$ for $Ra = 5.54 \times 10^8$. Thus the critical Rayleigh number Ra_c is obtained $5.53 \times 10^8 < Ra_c < 5.54 \times 10^8$. The accurate value of $Ra_c = 5.377 \times 10^8$ is obtained by interpolating from the above result. Moreover, the onset of unsteady flow is found to occur via Hopf bifurcation. As Fig.2-20 shows, the image part of growth

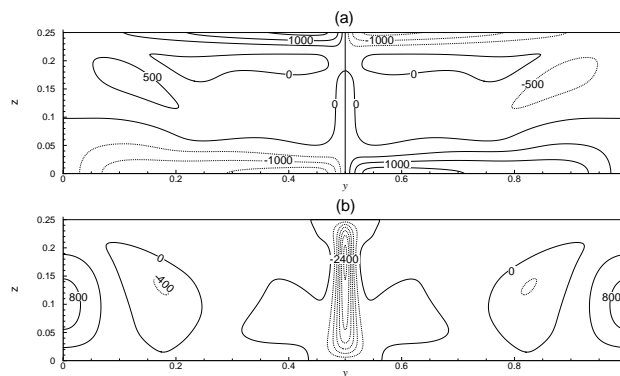


Figure 2-19: The horizontal (a) and vertical (b) velocity fields of $Ra = 5 \times 10^8$. It is steady and stable and symmetric with middle plume forcing, solid and dashed curves for positive and negative values, respectively.

rate is nonzero and the eigenmode of perturbation is periodic. This Hopf bifurcation of the horizontal convection has not been reported yet, and previous investigations dealt only with chaotic flows.

Meanwhile, the evolution of the perturbational vorticity fields during the first half period at $t = 0$ (a), $t = T/8$ (b), $t = T/4$ (c) and $t = 3T/8$ of $Ra = 5.54 \times 10^8$ are depicted in Fig. 2-21, respectively. The perturbational vorticity fields are symmetric about centerline, which implies that the horizontal velocity is nonzero at centerline. It can be seen that the perturbation tripole A (the shadowed ellipse in Fig. 2-21a) is generated from central downward jet, then propagates and amplifies along the central jet downward to the bottom wall (Fig. 2-21b,c,d). When tripole A approaches the bottom, it becomes weaker and weaker and breaks into two parts: the left and the right near the bottom, which can be seen from the evolution of tripole B (the shadowed rectangle in Fig. 2-21a). And the mean flow advects the broken vortices horizontally along the bottom wall (Fig. 2-21b,c,d). Then in the second half period, a reverse tripole will generate right the same place of vortices A at $t = T/2$, and the same story repeats for it, which is shown in Fig. 2-22. In short, the perturbations generate and amplify in the central vertical jet, but are propagated and weakened along the horizontal wall.

Further investigation shows that the instability of flow occurs due to shear. First, as we noted, the instabilities always occur in the center and propagate along the mean flow. Second, this trigger place locates in the area where there is a vigorous jet with strong shear (see e.g. Fig. 2-19b and Fig. 2-23) (Fig. 2-23). As the stratification is very weak here (see e.g. Fig. 2-18b), so that the flow in this region is dominated by momentum dynamics other than thermal dynamics. All these imply that the onset of instability leading to unsteady flow is due to shear instability at larger Rayleigh numbers, which is much different from Rayleigh-Bénard instability. However, shear is not the only sufficient condition for instability. For example, the instability near the top surface is suppressed due to strong stratification (Fig. 2-18b), though both the velocity (Fig. 2-19a) and the shear (Fig. 2-23) near top surface are still very large. In words, the onset of instability is due to velocity shear (shear instability) other than thermal dynamics (thermal instability).

Second, the sidewall plume forcing is considered. Fig. 2-24 shows the flow field and temperature field of $Ra = 5 \times 10^8$, in which the flow is symmetric, steady and stable like that under middle plume forcing. There are two strong downward jets near the walls corresponding to the sidewall plume forcing (Fig. 2-24a). As mentioned above, the sidewall plume forcing will lead to exactly the same flow pattern as the middle plume forcing does except for a position shift, which can be seen from Fig. 2-18 and Fig. 2-24. As the flow is stable, the center line like a free slip wall symmetrically separates the two cells. The left cell in Fig. 2-18 is exactly the same with the right cell in Fig. 2-24. However, the

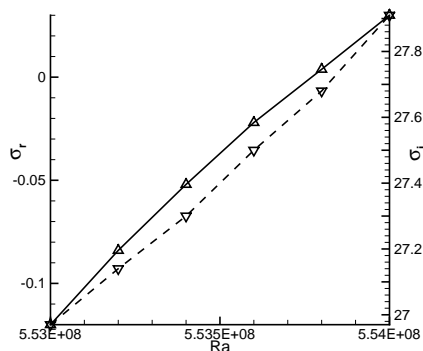


Figure 2-20: Growth rate σ_r (solid) and σ_i (dashed) vs. Ra , respectively.

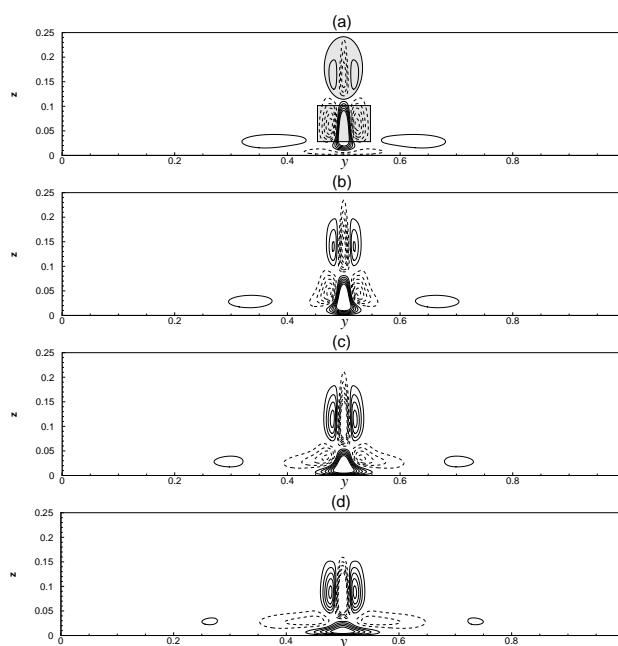


Figure 2-21: The perturbational vorticity fields at $t = 0$ (a), $t = T/8$ (b), $t = T/4$ (c) and $t = 3T/8$ of $Ra = 5.54 \times 10^8$, solid and dashed curves for positive and negative values, respectively.

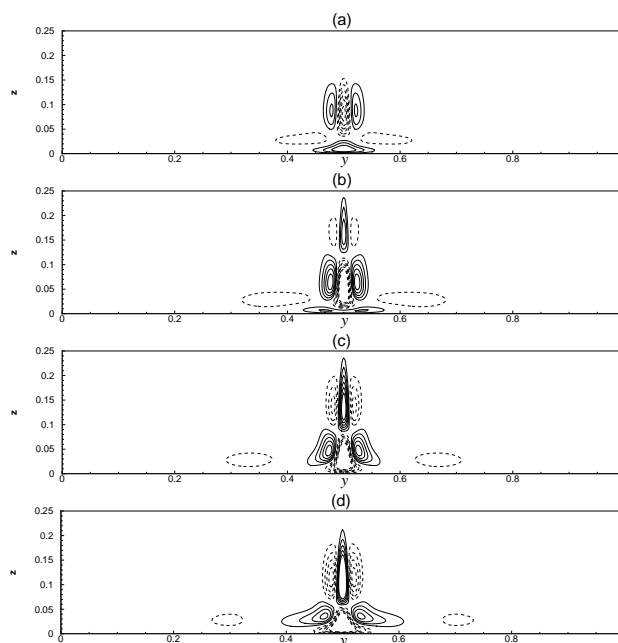


Figure 2-22: The perturbational vorticity fields at $t = T/2$ (a), $t = 5T/8$ (b), $t = 6T/8$ (c) and $t = 7T/8$ of $Ra = 5.54 \times 10^8$, solid and dashed curves for positive and negative values, respectively.

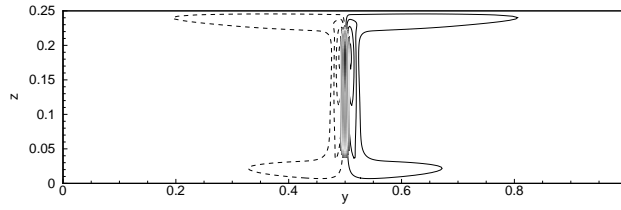


Figure 2-23: The vorticity of $Ra = 5.54 \times 10^8$ with vertical velocity w (shadowed as $w > 1800$), solid and dashed curves for positive and negative values, respectively.

flow is much more stable with the sidewall plume forcing. And the critical Rayleigh number is found $Ra_c \approx 1.85 \times 10^{10}$ (with 768×192 meshes) in this case. As noted above, the flow is much more stable with the sidewall plume forcing than that with the middle plume forcing, though both forcings lead to the same flow patterns. This is very interesting, and can be understood from the mechanism of instability.

It's found that the rigid wall suppresses the perturbation, which leads a more stable flow with the sidewall plume forcing than that with the middle plume forcing. As the flow loss stability is due to strong velocity shear in the center in horizontal convection, the smaller of the shear the more stable of the flow. In the case of middle plume forcing, the perturbation with nonzero horizontal velocity occurs at strongest downward jet. And the perturbed flows cross the center line and propagate downstream. However, in the case of sidewall plume forcing, these crossing flows are suppressed by rigid walls. So that the critical Rayleigh number is much larger in this case. Paparella and Young (2002) hypothesized that middle plume forcing may lead to a destabilization of the flow. Here this hypotheses is proved both physically and numerically.

§ 2.4.3 Conclusion

In conclusion, the onset of unsteady flow is found to occur via a Hopf bifurcation in the regime of $Ra > Ra_c = 5.5377 \times 10^8$ for the middle plume forcing at $Pr = 1$, which is much larger than the previously obtained value. Besides, the onset of unsteady flow is due to shear instability of

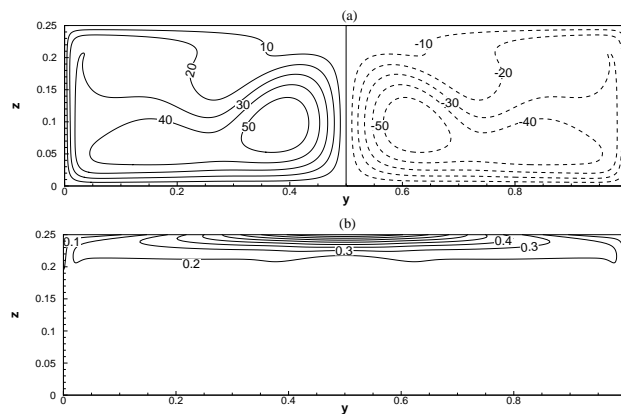


Figure 2-24: The flow field (a) and temperature field (b) of $Ra = 5 \times 10^8$, which are steady and stable and symmetric with sidewall plume forcing.

central downward jet. Finally, the second hypotheses of Paparella and Young (2002) for instability is numerically approved, i.e. the middle plume forcing can lead to a destabilization of the flow at relatively lower Rayleigh numbers.

Acknowledgements

This work was original from author's dream of understanding the mechanism of instability in the year 2000, when the author was a graduated student and learned the course of hydrodynamic stability by Prof. Yin X-Y at USTC (China). The author thanks Prof. Sun D-J at USTC (China), Dr. Yue P-T at UBC (Canada) for their help on preparing the report.

The support of NSFC (No. 40705027 and No. 10602056) and the National Science Foundation for Post-doctoral Scientists of China are gratefully acknowledged. The author would like to acknowledge Professor Wang W at OUC (China) and Professor Huang R. X. at WHOI (USA) for the useful comments and suggestions on the studies of horizontal convection during the preparation of the second part of the report.

Bibliography

- [1] Lord Rayleigh. On the stability or instability of certain fluid motions. Proc London Math Soc. 1880, **11**:57–70
- [2] W. O. Criminale, T. L. Jackson, R. D. Joslin. Theory and computation of hydrodynamic stability. Cambridge, U.K.: Cambridge University Press, 2003
- [3] H. L. Kuo. Dynamic Instability of Two-Dimensional. Nondivergent Flow in. a. Barotropic Atmosphere. J Meteorology. 1949, **6**:105–122
- [4] R. Fjørtoft. Application of integral theorems in deriving criteria of stability of lamiar flow and for the baroclinic circular vortex. Geofysiske Publikasjoner. 1950, **17**:1–52
- [5] W. Tollmien. General instability criterion of laminar velocity disturbances. Tech. Rep. NACA TM-792, NACA, 1936
- [6] P. G. Drazin, W. H. Reid. Hydrodynamic Stability. Cambridge University Press, 1981
- [7] P. Huerre, M. Rossi. Hydrodynamic instabilities in open flow. C. Godrèche, P. Manneville, (Editors) Hydrodynamics and nonlinear instabilities, Cambridge: Cambridge University Press, 1998
- [8] V. I. Arnold. Conditions for nonlinear stability of the stationary plane curvilinear flows of an ideal fluid. Doklady Mat Nauk. 1965, **162(5)**:975–978 (Engl. transl.: Sov.Math. 6, 773–777)
- [9] V. I. Arnold. A Variational principle for three-dimensional stationary flows of the ideal fluid. J Applied Math and Mechan. 1965, **29(5)**:1002–1008
- [10] V. I. Arnold, B. A. Khesin. Topological methods in hydrodynamics. Springer-Verlag, 1998
- [11] T. E. Dowling. Dynamics of Jovian Atmospheres. Ann Rev Fluid Mech. 1995, **27**:293–334
- [12] Geoffrey K. Vallis. Atmospheric and Oceanic Fluid Dynamics. Cambridge, U. K.: Cambridge University Press, 2006. Doi:10.2277/0521849691
- [13] Peter J. Schmid, Dan S. Henningson. Stability and Transition in Shear Flows. Springer-Verlag, 2000
- [14] V. I. Arnold. On the a priori estimate in the theory of hydrodynamical stability. Amer Math Soc Transl. 1969, **19**:267–269
- [15] L. N. Howard. Note on a paper of John W Miles. J Fluid Mech. 1961, **10**:509–512

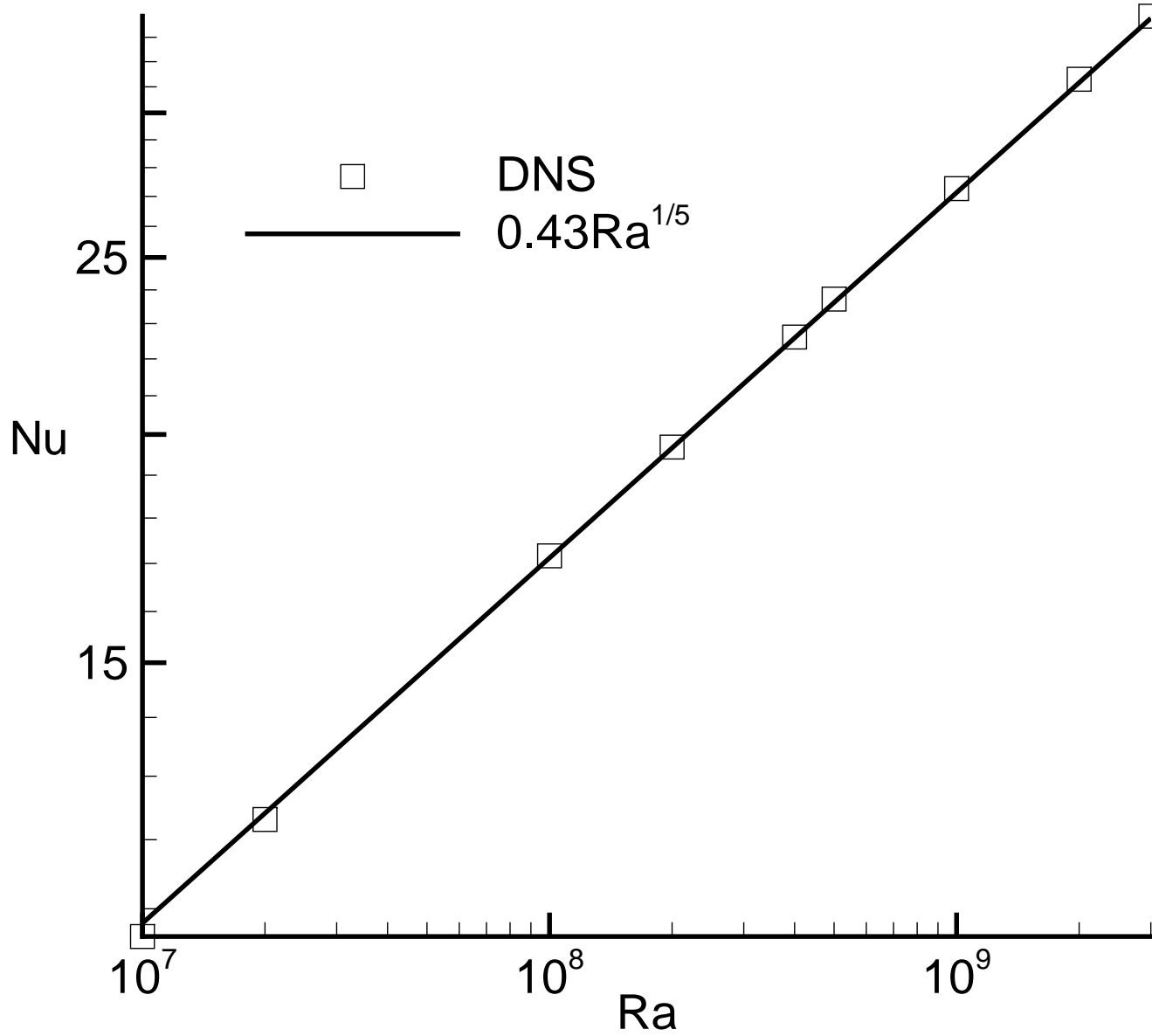
-
- [16] Lord Rayleigh. *The Theory of Sound*. London: Macmillan, 1894
- [17] S. Chandrasekhar. *Hydrodynamic and Hydromagnetic Stability*. New York, U.S.A.: Dover Publications, Inc., 1961
- [18] C. C. Lin. *The Theory of Hydrodynamic Stability*. London, UK: Cambridge University Press, 1955
- [19] Liang Sun. General stability criterion of inviscid parallel flow . *Eur J Phys.* 2007, **28**:889–895
- [20] E Høiland. On two-dimensional perturbations of linear flow. *Geofysiske Publikasjoner.* 1953, **18**:1–12
- [21] Lord Kelvin. *Vortex Statics*. *Collected works.* 1875, **IV**:115–128
- [22] P. G. Saffman. *Vortex Dynamics*. Cambridge, U.K.: Cambridge University Press, 1992
- [23] V. A. Vladimirov, K. I. Ilin. On Arnolds variational principles in fluid mechanics. E. Bierstone, B. Khesin, A. Khovanskii, J. E. Marsden, (Editors) *The Arnoldfest: Proceedings of a Conference in Honour of V.I. Arnold for His Sixtieth Birthday*, American Mathematical Society, 1999. 471–495
- [24] G. K. Batchelor. *An Introduction to Fluid Dynamics*. Cambridge, U. K.: Cambridge University Press, 1967
- [25] A. D. D. Craik. Nonlinear resonant instability of in boundary layers. *J Fluid Mech.* 1971, **50**:393–413
- [26] K. M. Butler, B. F. Farrell. Three-dimensional optimal perturbations in viscous shear flow. *Phys Fluids A.* 1992, **4**:1637–1650
- [27] P.G. Baines, H Mitsudera. On the mechanism of shear flow instabilities. *J Fluid Mech.* 1994, **276**:327–342
- [28] C. Staquet, J. Sommeria. INTERNAL GRAVITYWAVES: From Instabilities to Turbulence. *Ann Rev Fluid Mech.* 2002, **34**:559–593
- [29] K. O. Friedrichs. *Fluid dynamics*. Providence, Rhode Island: Brown University, 1942
- [30] P. G. Drazin, L.N. Howard. Hydrodynamic stability of parallel flow of an inviscid fluid. G. G. Chernyi, (Editor) *Advances in applied mechanics*, Academic Press, New York, 1966, vol. 9. 1–81
- [31] Liang Sun. Long-wave instability in shear flow. *arXiv:physics/0601112v2.* 2006
- [32] F. L. Ponta, H. Aref. Strouhal-Reynolds Number Relationship for Vortex Streets. *Phys Rev Lett.* 2004, **93**(8):084501
- [33] Liang Sun. General stability criterion of two-dimensional inviscid parallel flow. *arXiv:physics/0512208v3.* 2005
- [34] J. Ma, Y. H. Chen, B. X. Gan, F. H. Wang, D. Wang. Stability of Rayleigh–Taylor Vortices in Dusty Plasma. *Chin Phys Lett.* 2006, **23**:895–898

-
- [35] B Paul, G. Francois. Generalized Rayleigh criterion for non-axisymmetric centrifugal instabilities. *J Fluid Mech.* 2005, **542**:365–379
- [36] L. N. Howard, A. S. Gupta. On the hydrodynamic and hydromagnetic stability of swirling flows. *J Fluid Mech.* 1962, **14**:463–476
- [37] T. J. Pedley. On the stability of viscous flow in a rapidly rotating pipe. *J Fluid Mech.* 1969, **35**:97–115
- [38] D. J. Tritton. Stabilization and destabilization of turbulent shear flow in a rotating fluid. *J Fluid Mech.* 1992, **241**:503–523
- [39] S. Leblanc, C. Cambon. On the three-dimensional instabilities of plane flows subjected to Coriolis force. *Phys Fluids.* 1997, **9(5)**:1307–1316
- [40] H. Faisst, B. Eckhardt. Transition from the Couette-Taylor system to the plane Couette system. *Phys Rev E.* 2000, **61**:7227–7230
- [41] L. N. Howard. Review of Hydrodynamic and hydromagnetic stability by S. Chandrasekhar. *J Fluid Mech.* 1962, **13**:158–160
- [42] C. Wunsch. What is the thermohaline circulation? *Science.* 2002, **298**:1179–1180
- [43] S. Rahmstorf. The current climate. *Nature.* 2003, **421**:699–699
- [44] L. Sun, M. Mu, D. J. Sun, X. Y. Yin. Passive Mechanism of Decadal Variation of Thermohaline Circulation. *J Geophys Res.* 2005, **110**:C07025. Doi:10.1029/2005JC002897
- [45] W. Munk, C. Wunsch. The Moon and mixing: abyssal recipes II. *Deep-Sea Research.* 1998, **45**:1977–2010
- [46] R. X. Huang. Mixing and energetics of the thermohaline circulation. *J Phys Oceanogr.* 1999, **26**:727–746
- [47] C. Wunsch, R. Ferrari. Vertical mixing, energy, and the general circulation of the oceans. *Annual Review of Fluid Mechanics.* 2004, **36**:281–314
- [48] C. Quon, M. Ghil. Multiple equilibria in thermosolutal convection due to salt-flux boundary conditions. *J Fluid Mech.* 1992, **245**:449–484
- [49] H. A. Dijkstra, M. J. Molemaker. Symmetry breaking and overturning oscillations in thermohaline-driven flows. *J Fluid Mech.* 1997, **331**:169–198
- [50] L. Fleury, O. Thual. Stationary fronts of the thermohaline circulation in the low-aspect ratio limit. *J Fluid Mech.* 1997, **349**:117–147
- [51] F. Paparella, W. R. Young. Horizontal convection is non-turbulent. *J Fluid Mech.* 2002, **466**:205–214
- [52] H. T. Rossby. On thermal convection driven by non-uniform heating from below: an experimental study. *Deep-Sea Research.* 1965, **12**:9–16

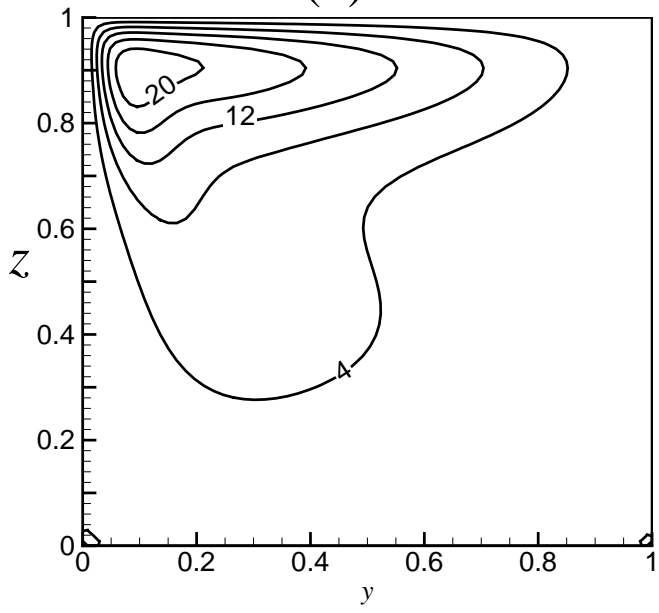
BIBLIOGRAPHY

- [53] J. C. Mullarney, R. W. Griffiths, G. O. Hughes. Convection driven by differential heating at a horizontal boundary. *J Fluid Mech.* 2004, **516**:181–209
- [54] W. Wang, R. X. Huang. An experimental study on thermal circulation driven by horizontal differential heating. *J Fluid Mech.* 2005, **540**:49–73
- [55] H. T. Rossby. Numerical experiments with a fluid non-uniformly heated from below. *Tellus.* 1998, **50A**:242–257
- [56] J. H. Siggers, R. R. Kerswell, N. J. Balmforth. Bounds on horizontal convection. *J Fluid Mech.* 2004, **517**:55–70
- [57] P. Cessi, W. R. Young. Multiple equilibria in two-dimensional thermohaline circulation. *J Fluid Mech.* 1992, **241**:291–309
- [58] J. W. Sandström. Meteorologische Studien im schwedischen Hochgebirge. Goteborgs K Vetenskaps-och Vitterhetssamhalles Handl Ser 4. 1904, **22**:48pp
- [59] C. Wunsch. Moon, tides and climate. *Nature.* 2000, **405**:743–744
- [60] A. Arakawa. Computational design for long-term numerical integrations of the equations of atmospheric motion. *J Comput Phys.* 1966, **1**:119–143
- [61] P. Orlandi. Fluid flow phenomena. Dordrecht, The Netherlands: Kluwer Academic publishers, 2000
- [62] L. Sun, Y. F. Sun, D. J. Sun, X. Y. Yin. Horizontal convection in a narrow rectangular cavity. *Journal of Hydrodynamics A.* 2006, **21**(2):252–258
- [63] P. Le Quéré. Accurate solution to the square thermally driven cavity at high Rayleigh number. *Computers and Fluids.* 1991, **20**:29–41
- [64] Z. Tian, Y. Ge. A fourth-order compact finite difference scheme for the steady stream function-Cvorticity formulation of the Navier-Stokes/Boussinesq equations. *Int J Numer Meth Fluids.* 2003, **41**:495–518
- [65] H. A. Dijkstra. *Nonlinear Physical Oceanography: A Dynamical Systems Approach to the Large Scale Ocean Circulation and El Niño.* New York: Springer, 2005
- [66] R. C. Beardsley, J. F. Festa. A numerical model of convection driven by a surface stress and non-uniform horizontal heating. *J Phys Oceanogr.* 1973, **2**:444–455
- [67] G. O. Hughes, R. W. Griffiths, J. C. Mullarney, W. H. Peterson. A theoretical model for horizontal convection at high Rayleigh number. *J Fluid Mech.* 2007, **581**:251–276
- [68] L. Sun, Y. F. Sun, D. J. Ma, D. J. Sun. Power law of Horizontal Convection at High Rayleigh Numbers. *Acta Physica Sinica.* 2007, **56**(11):6503–6507

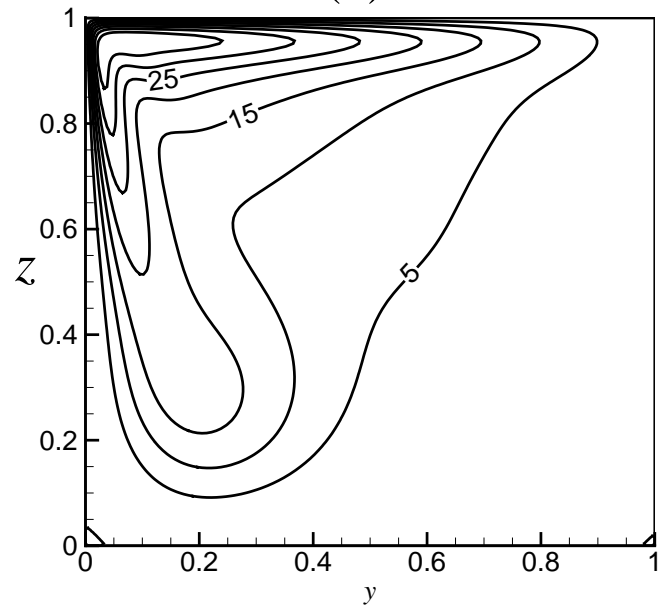
(b)



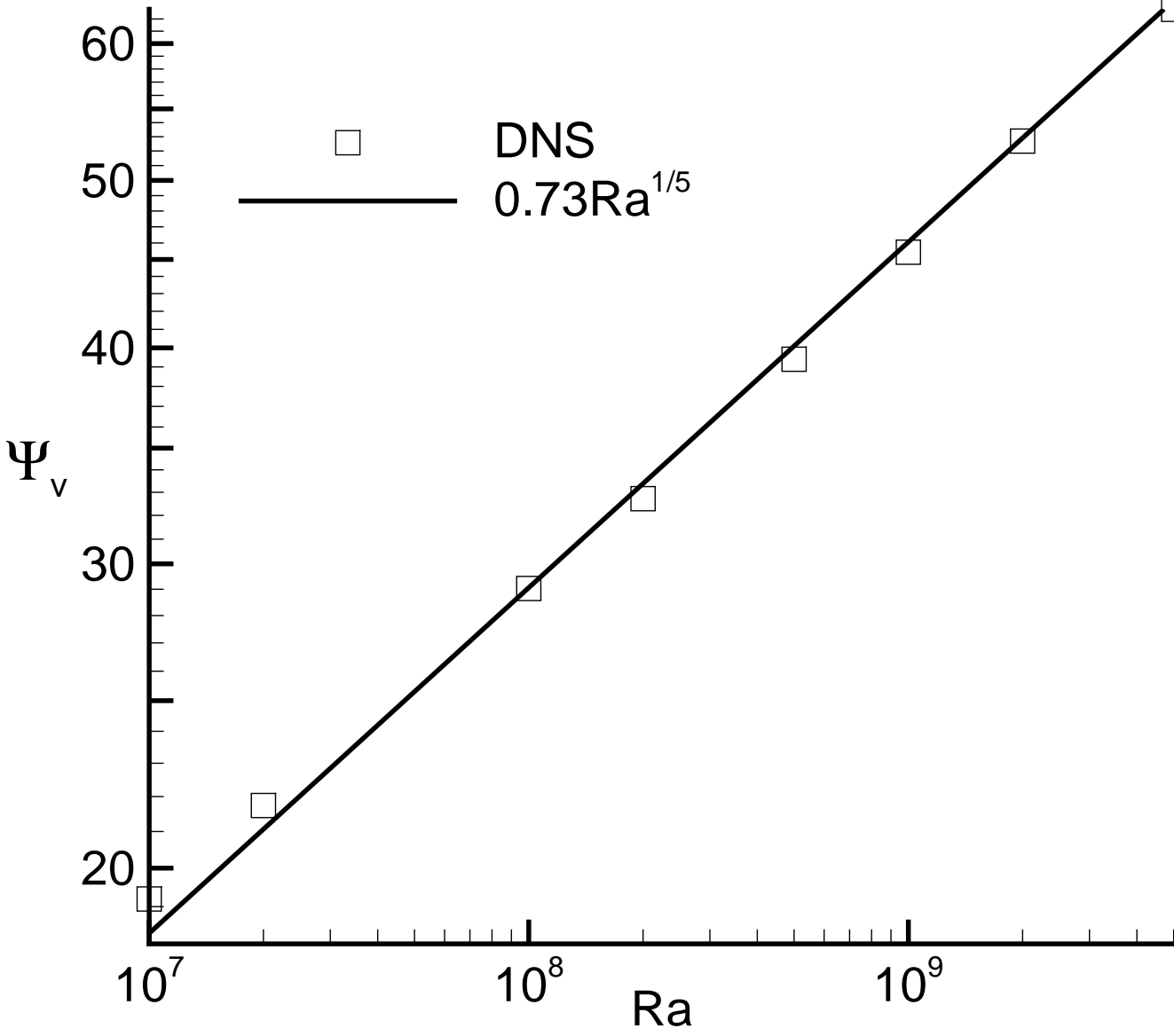
(a)



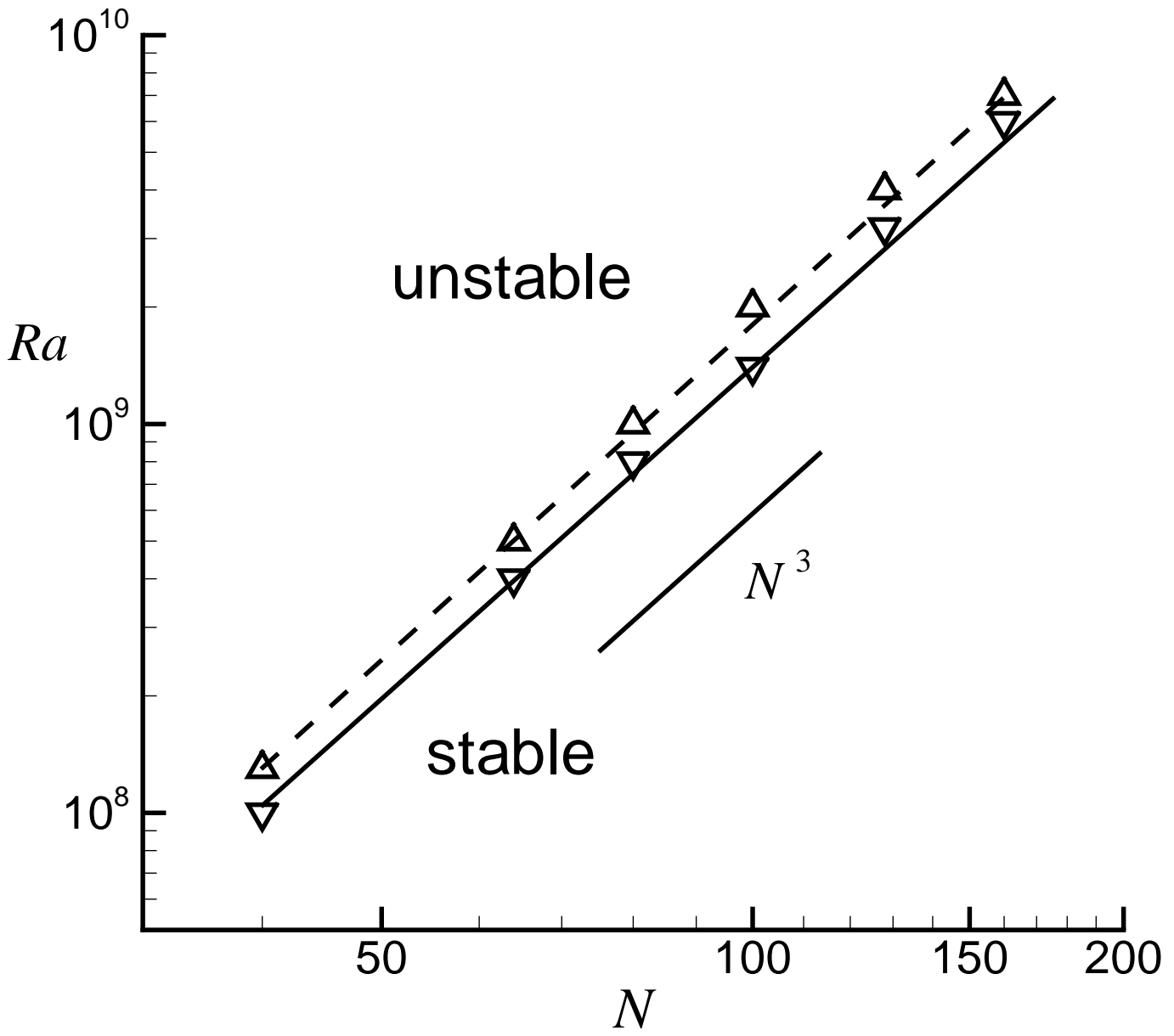
(b)



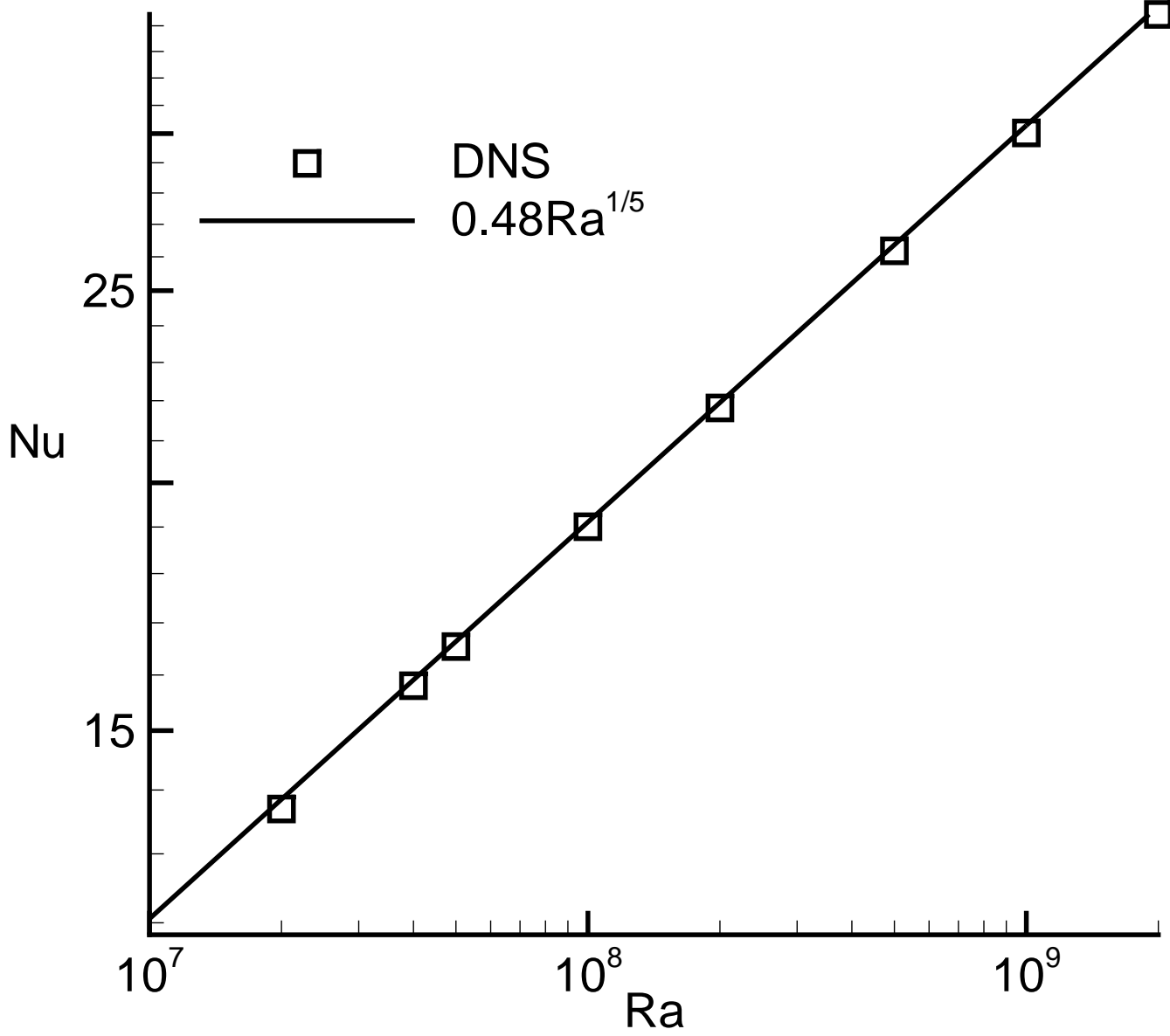
(a)



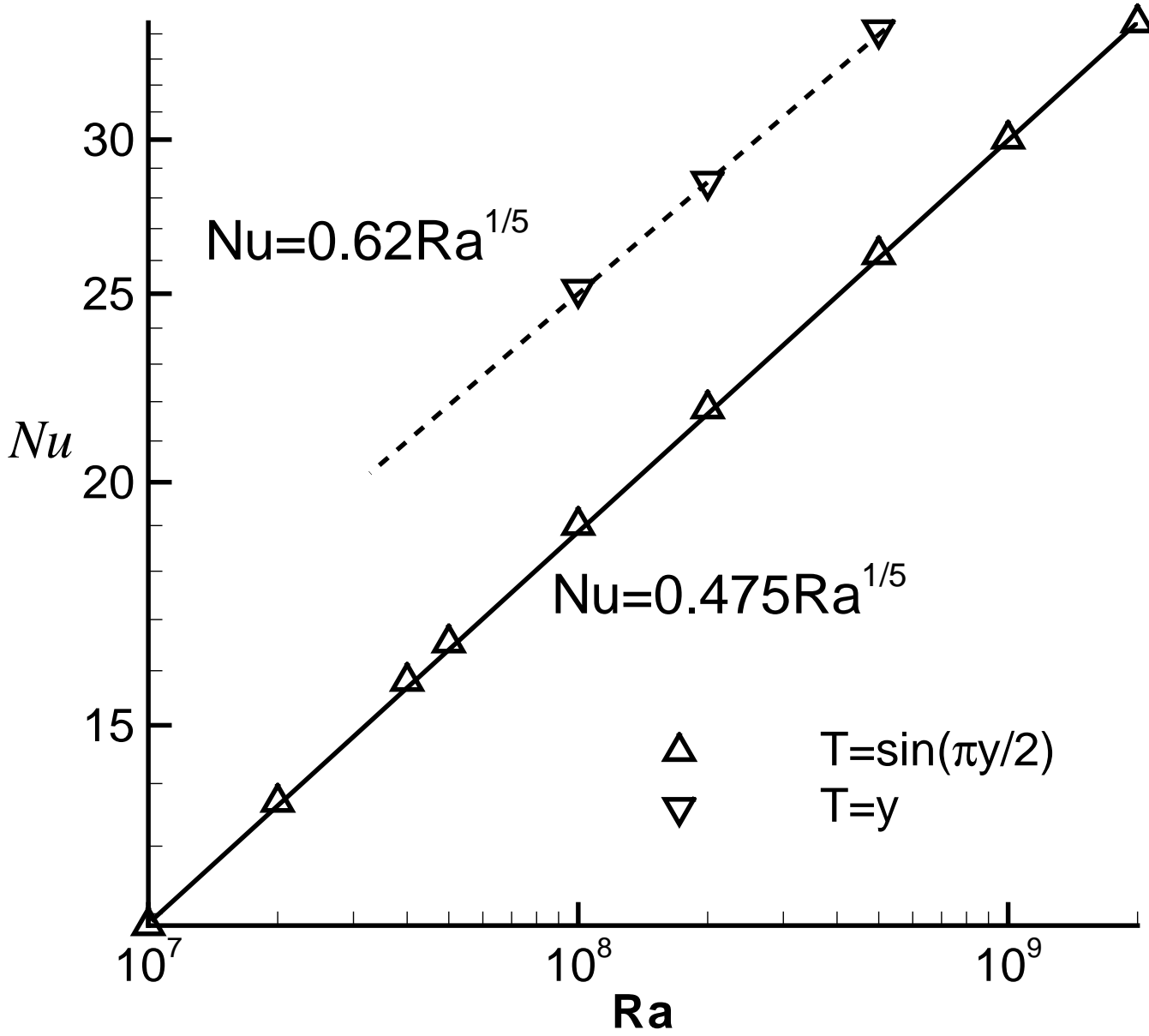
(b)

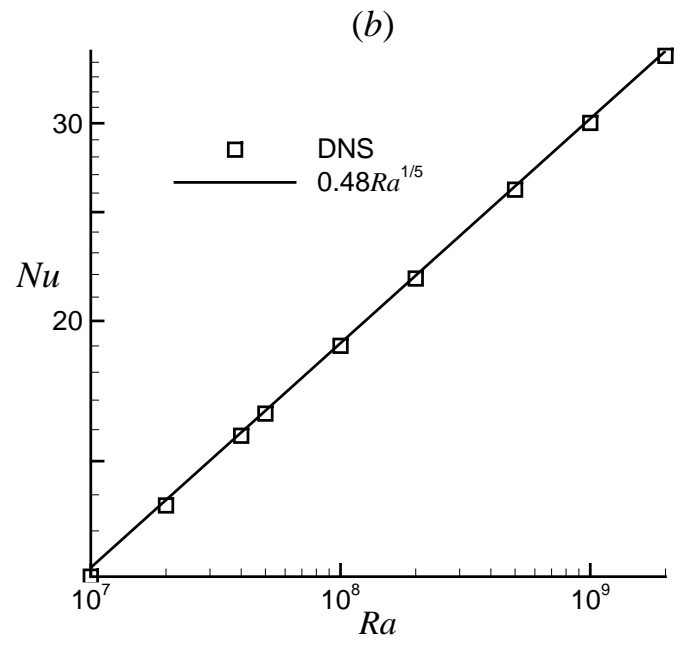
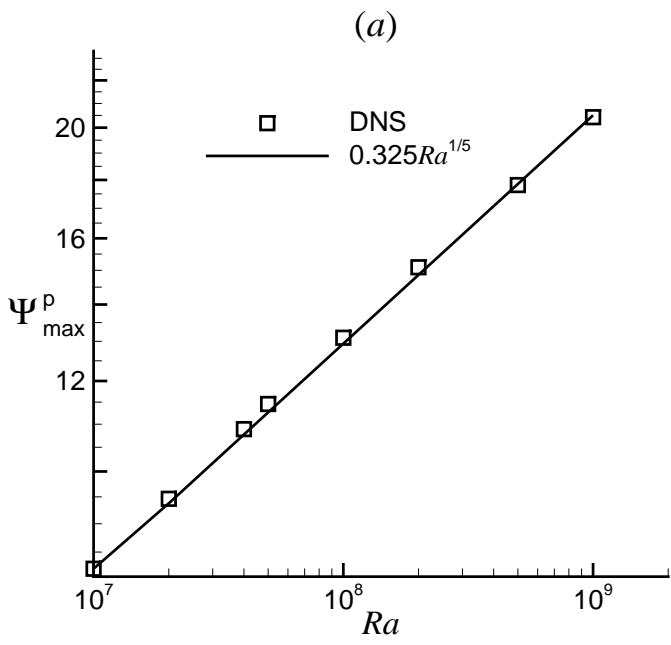


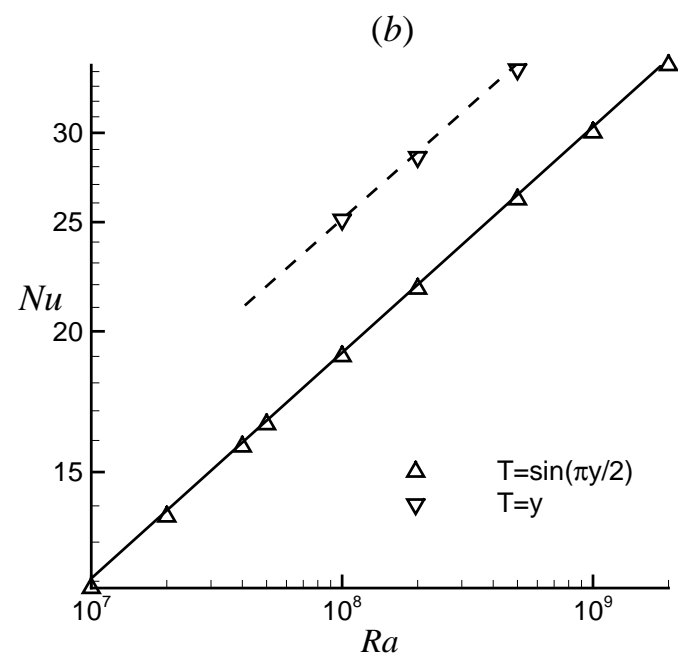
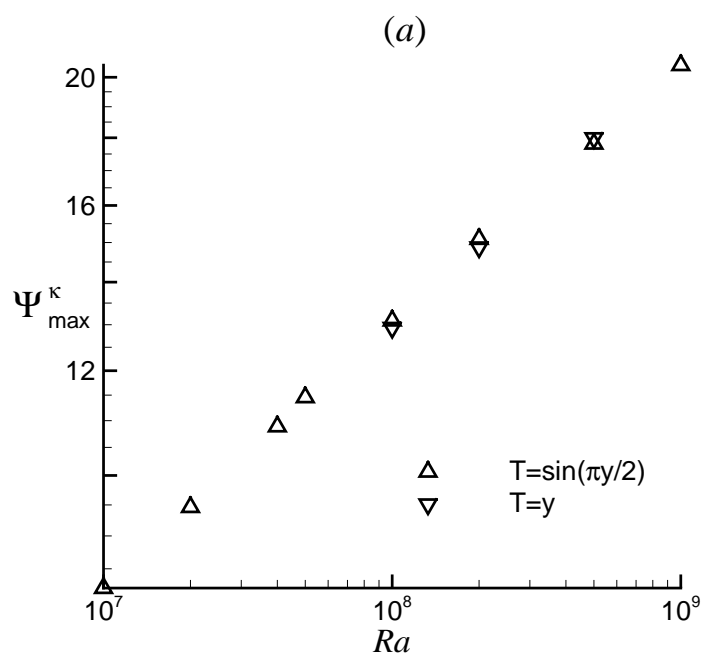
(b)



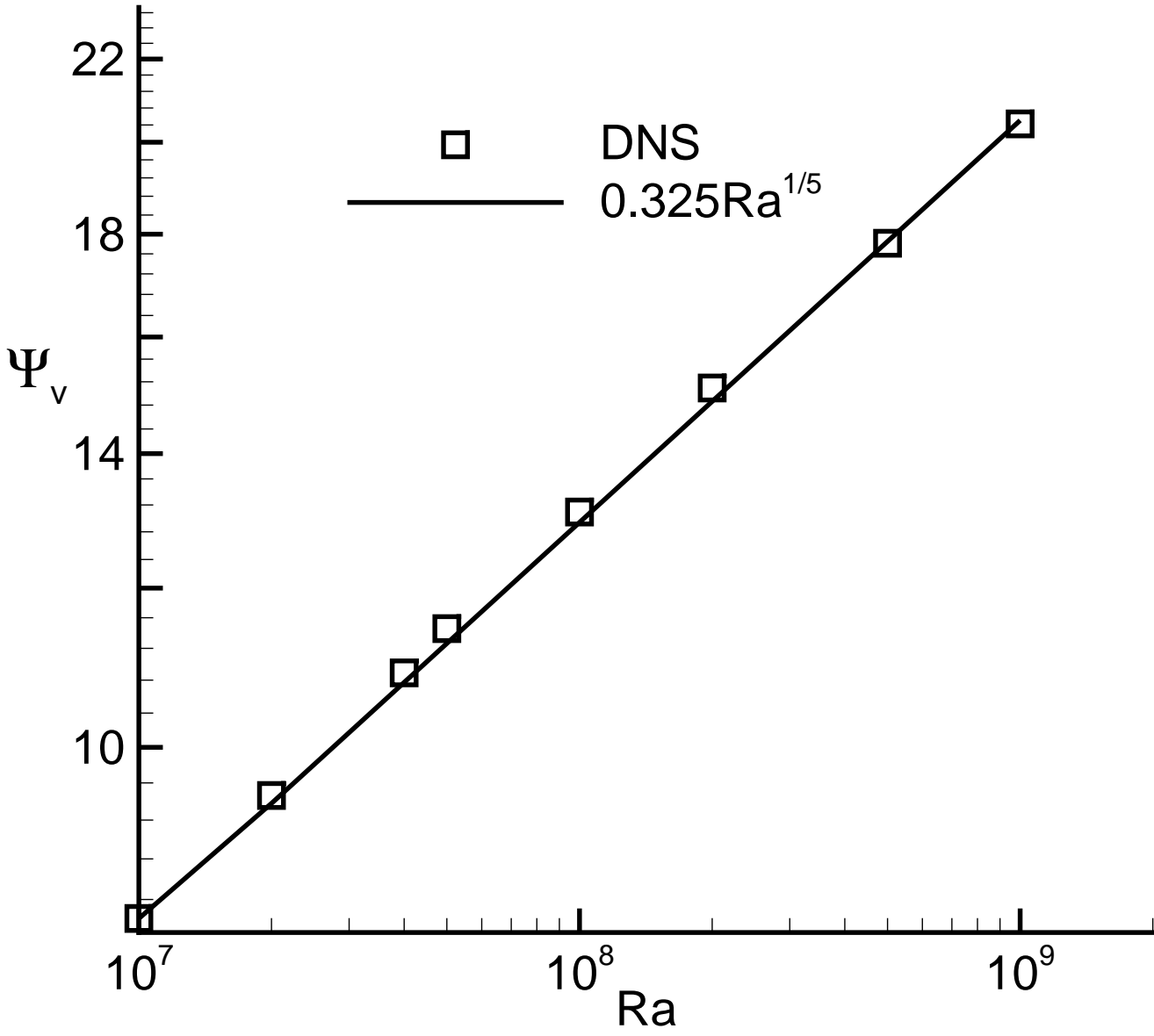
(b)



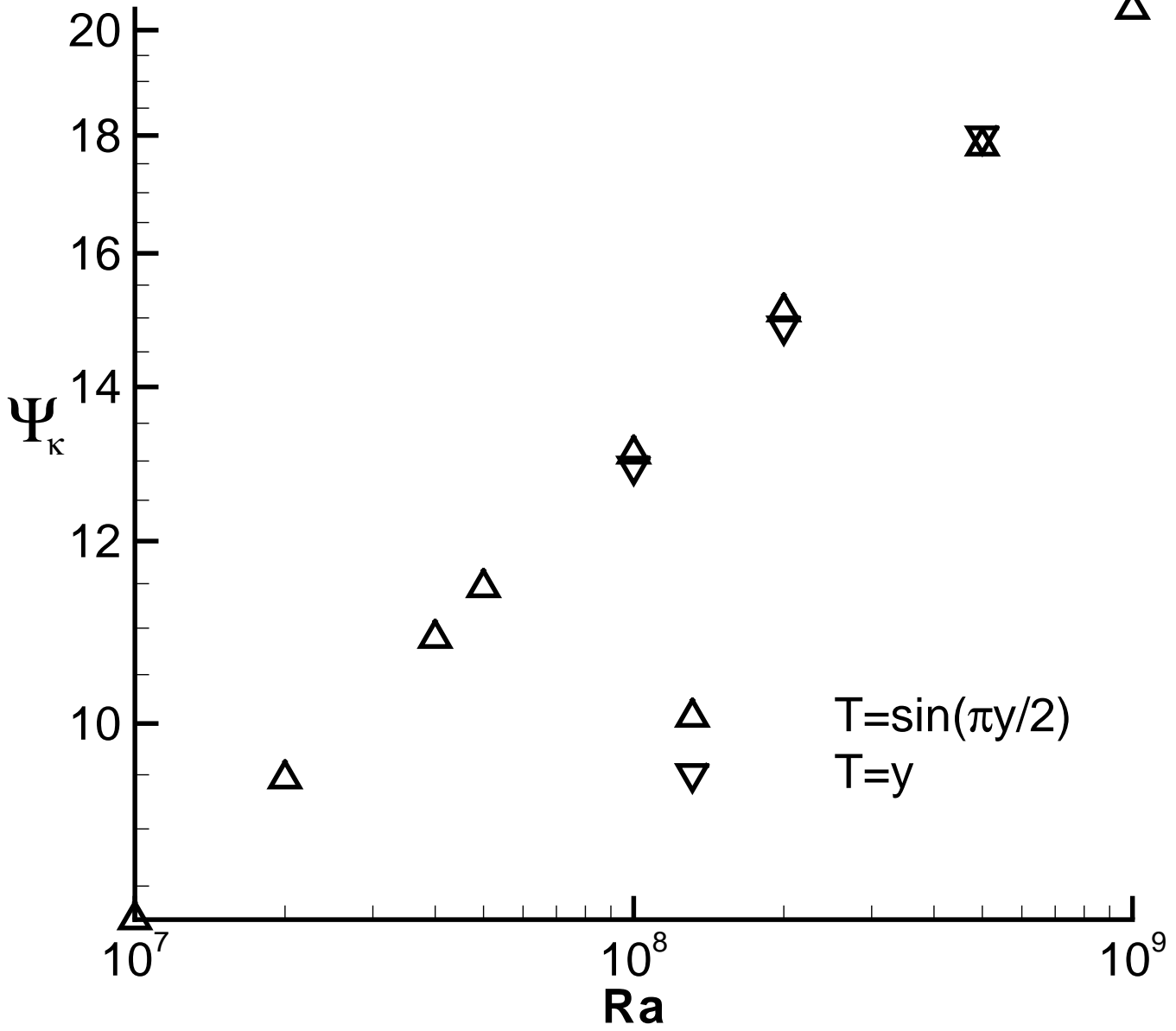


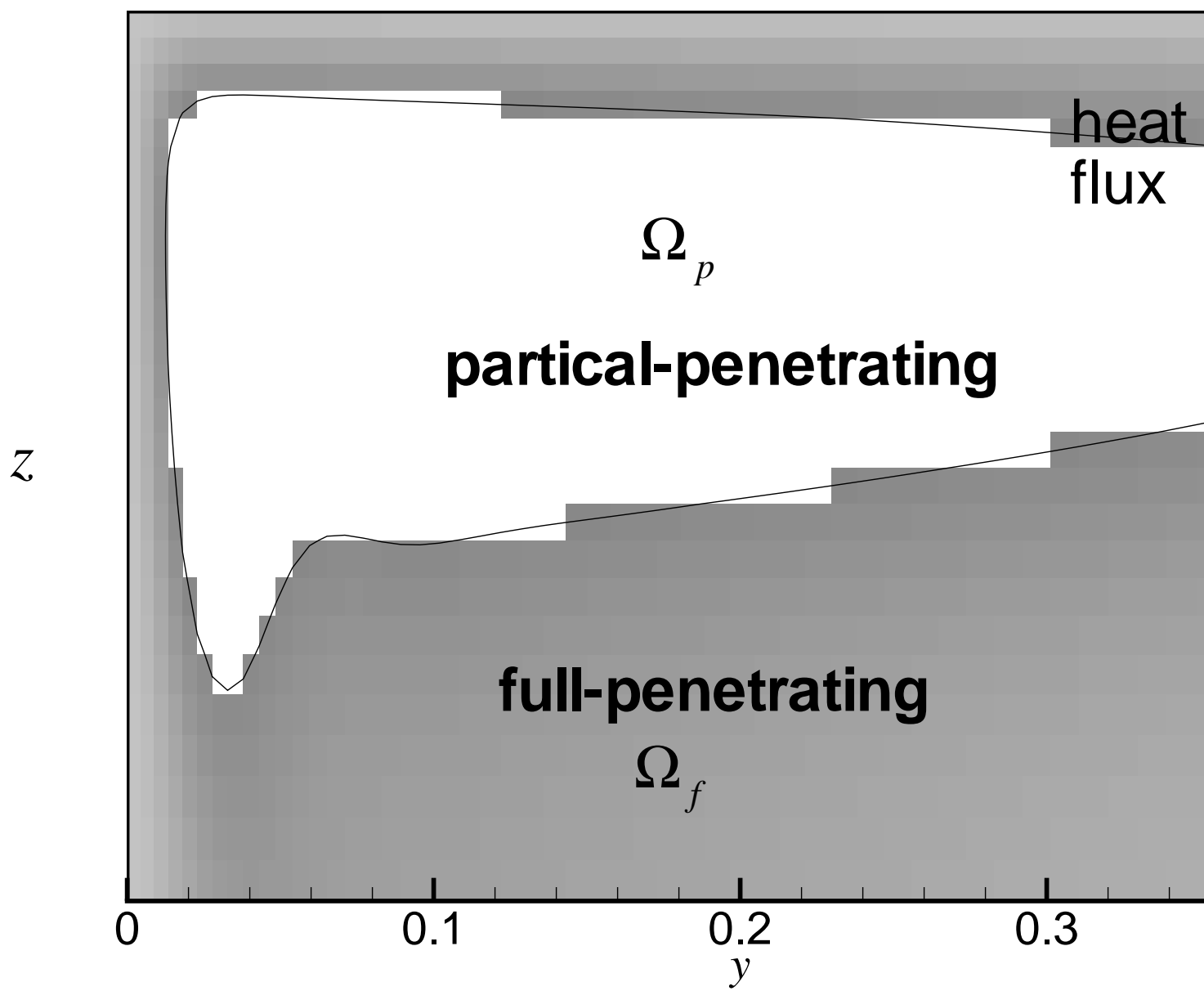


(a)

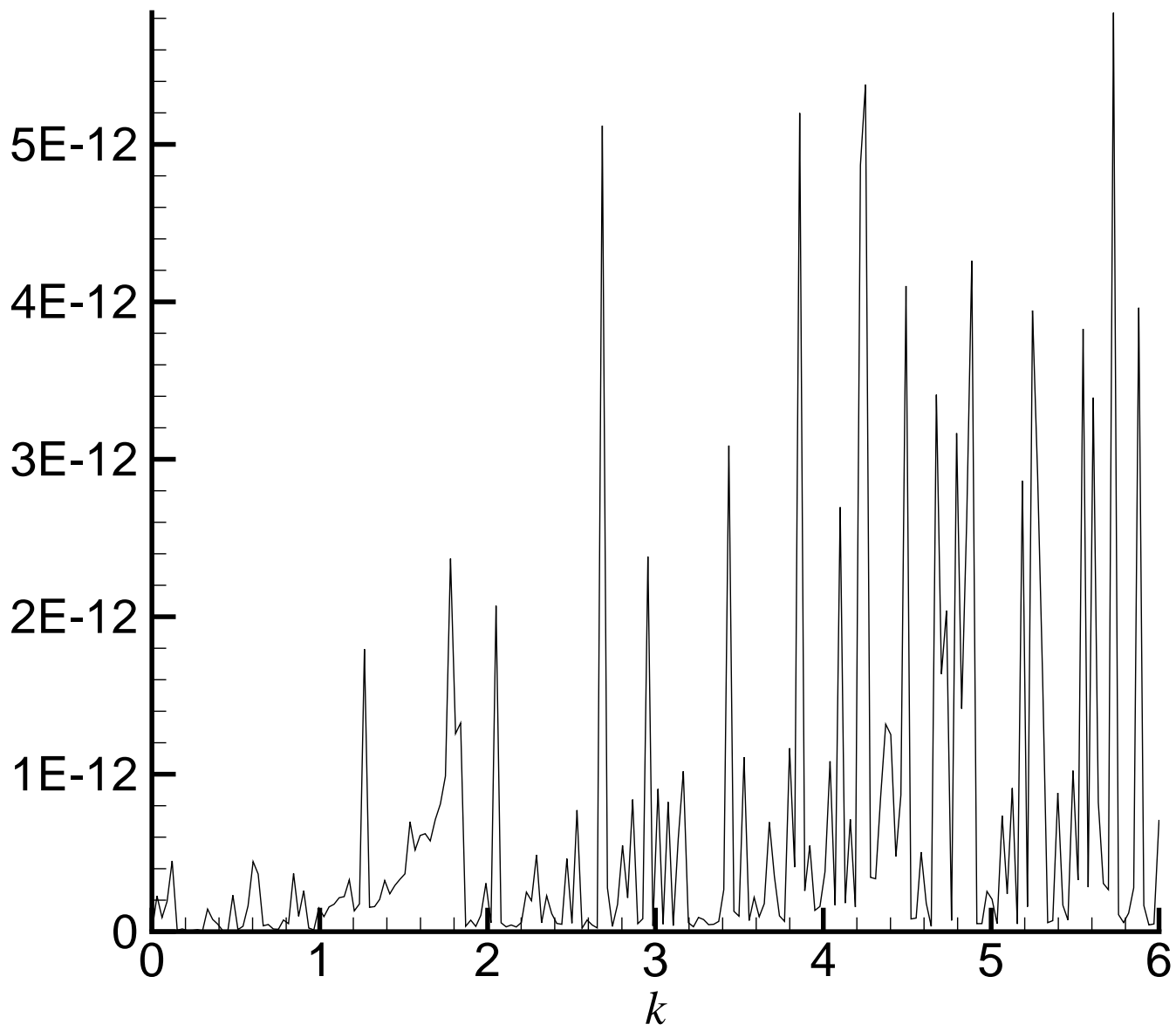


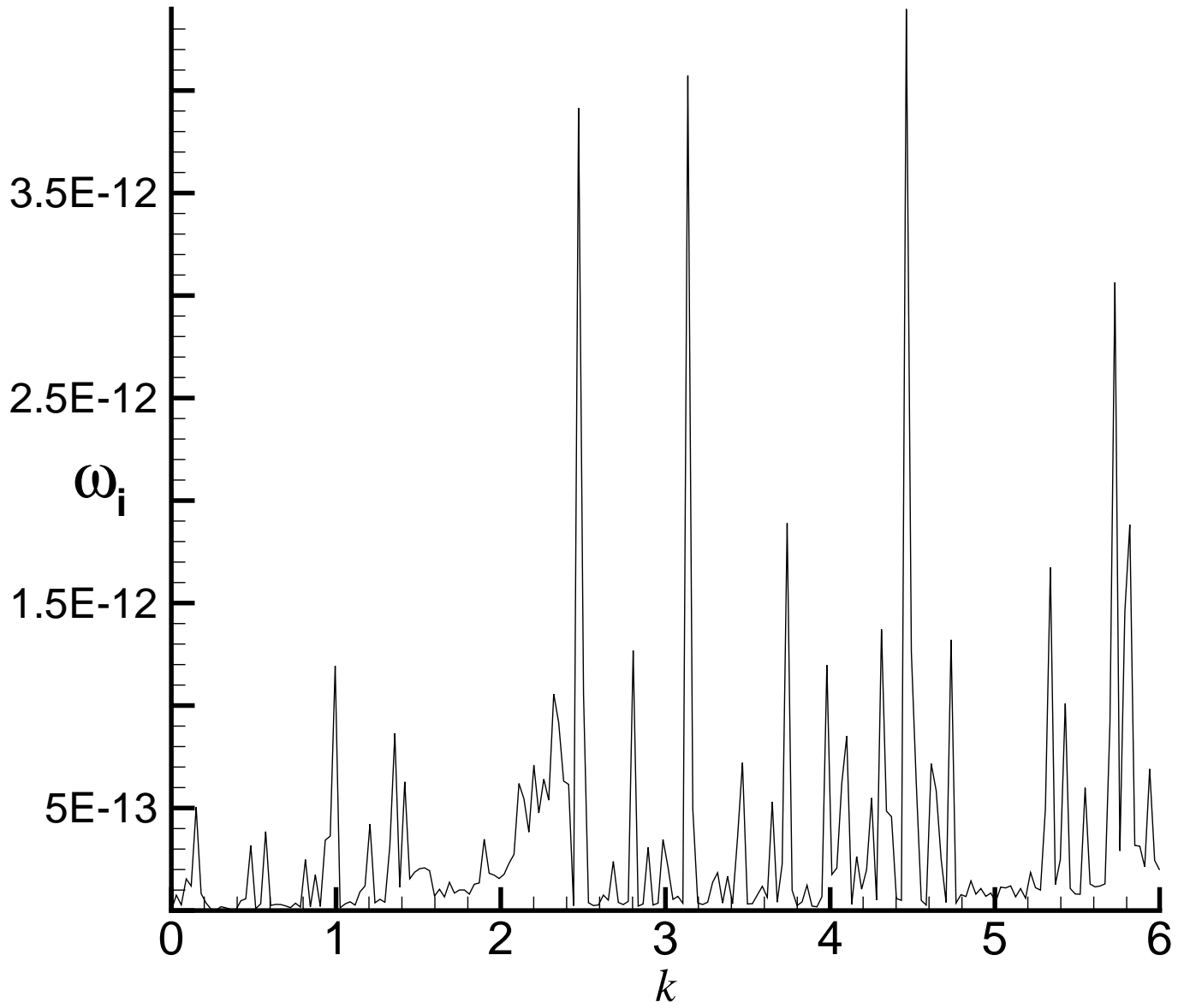
(a)



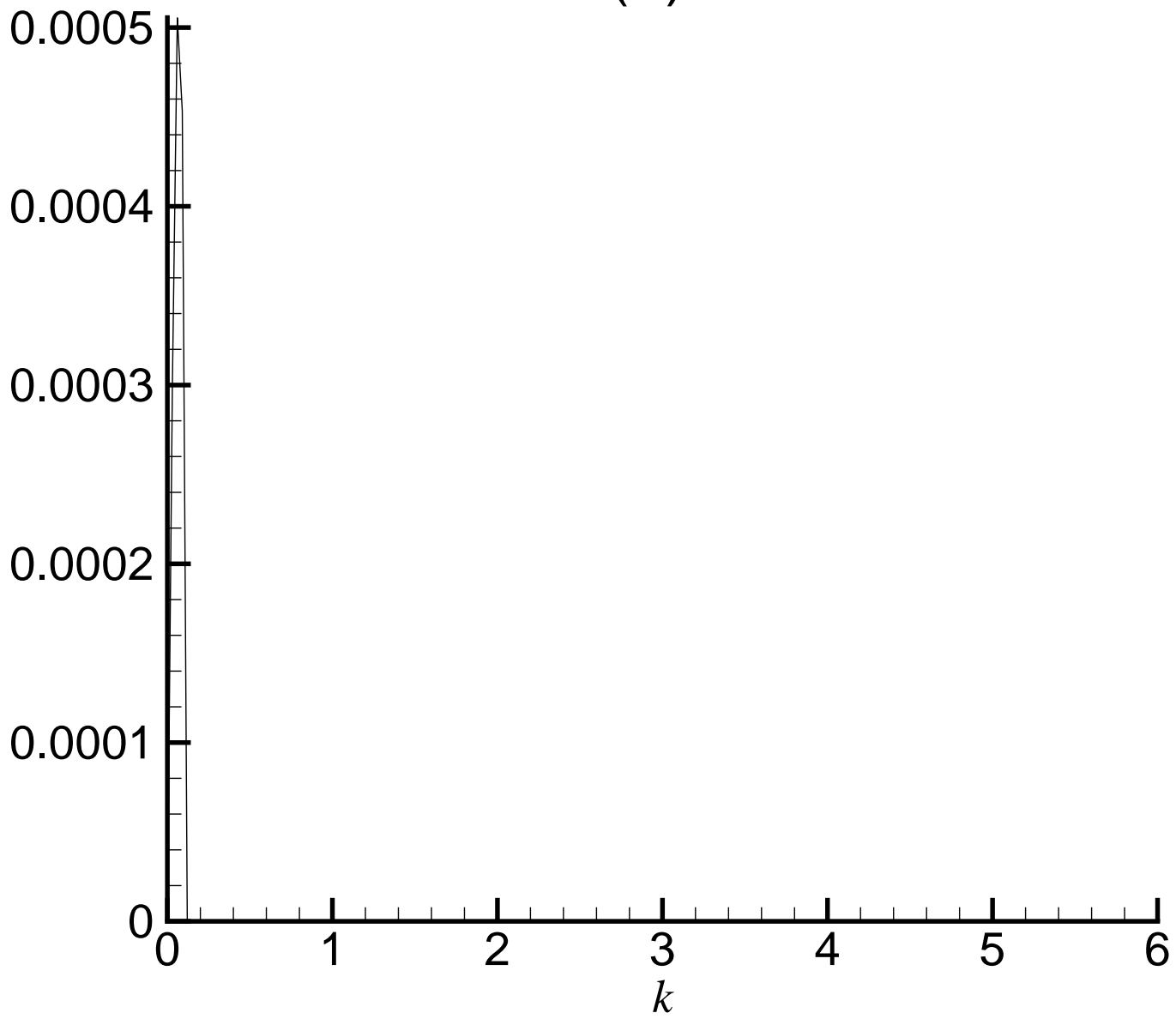


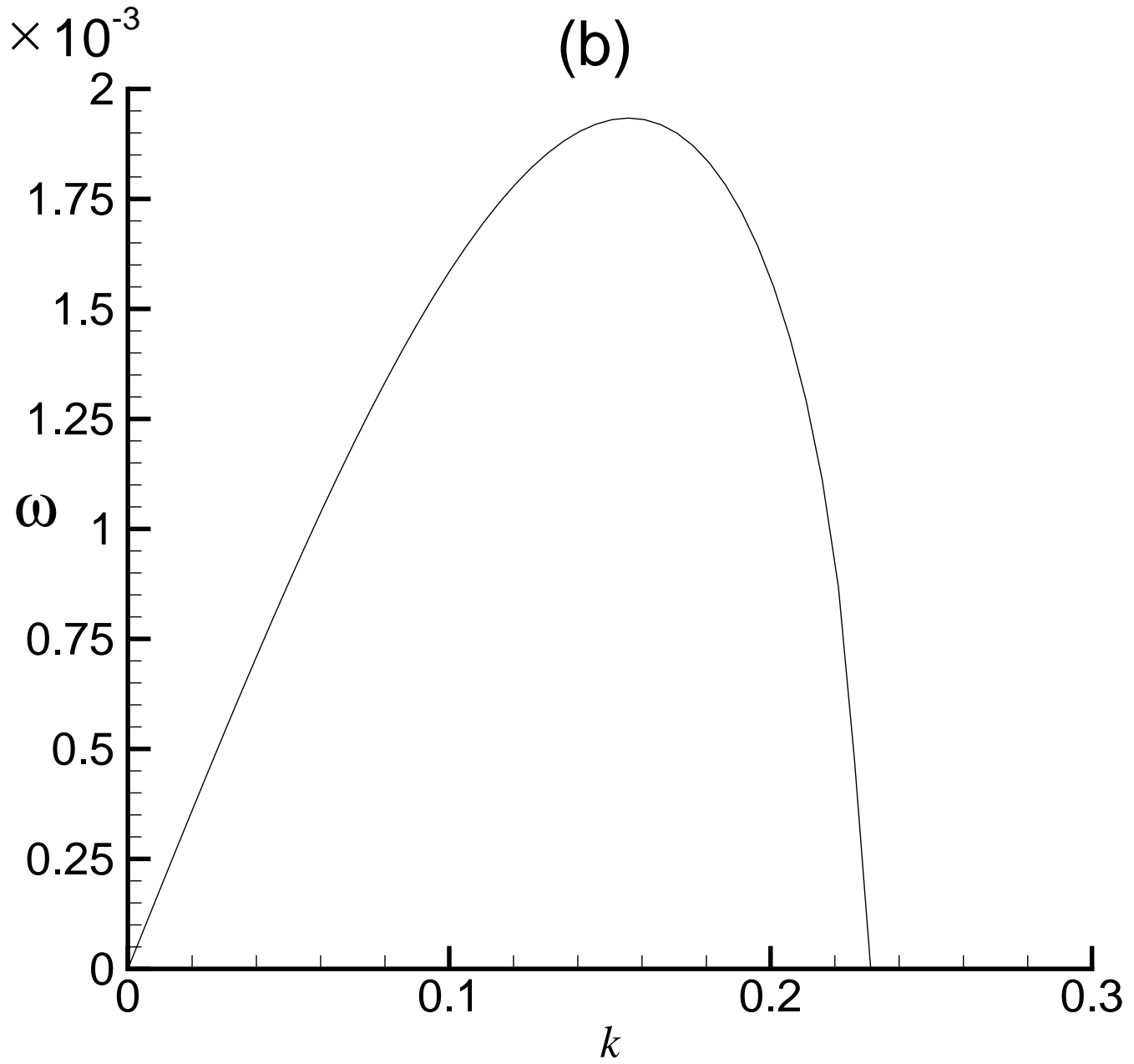
(a)

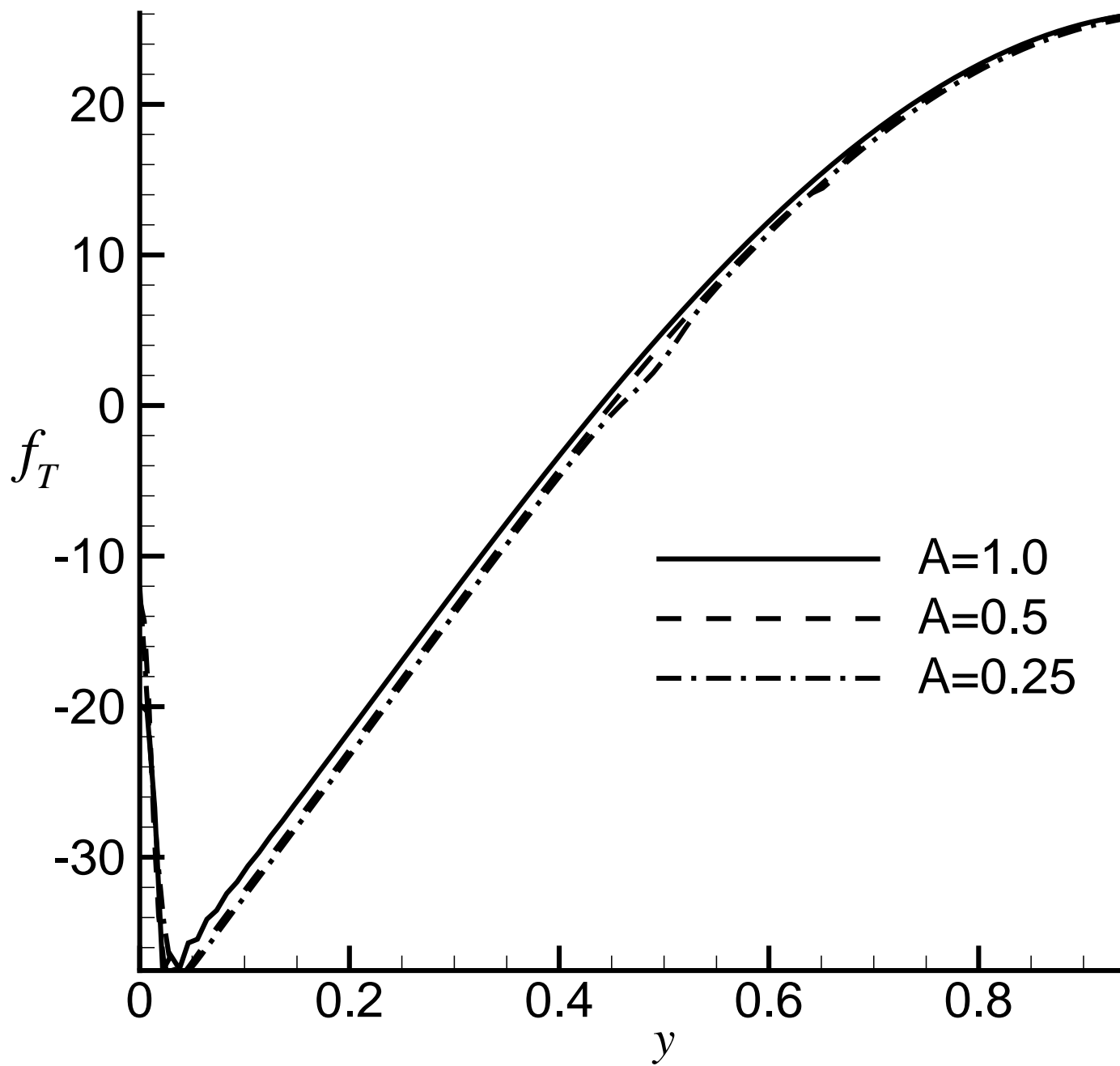


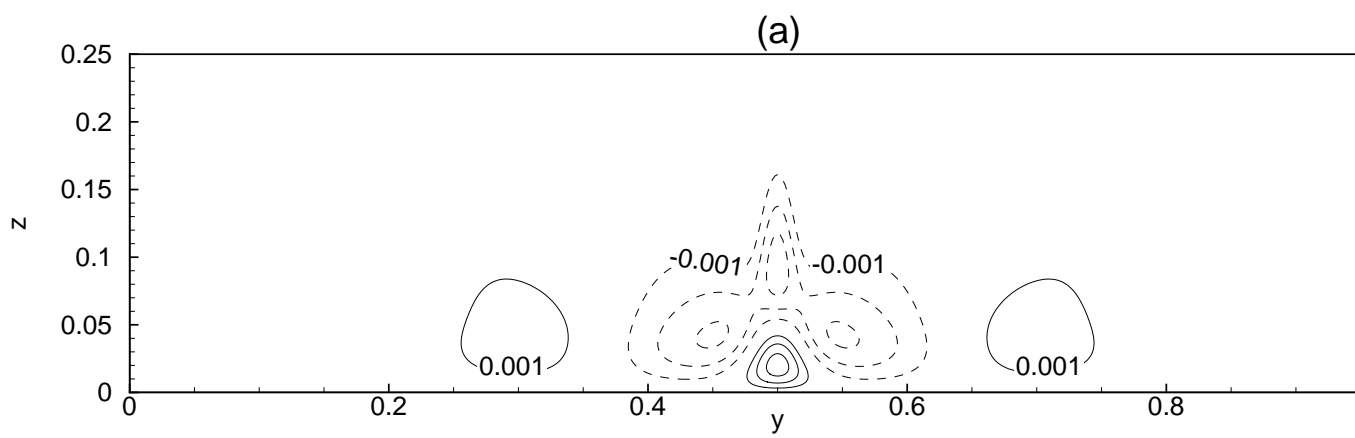
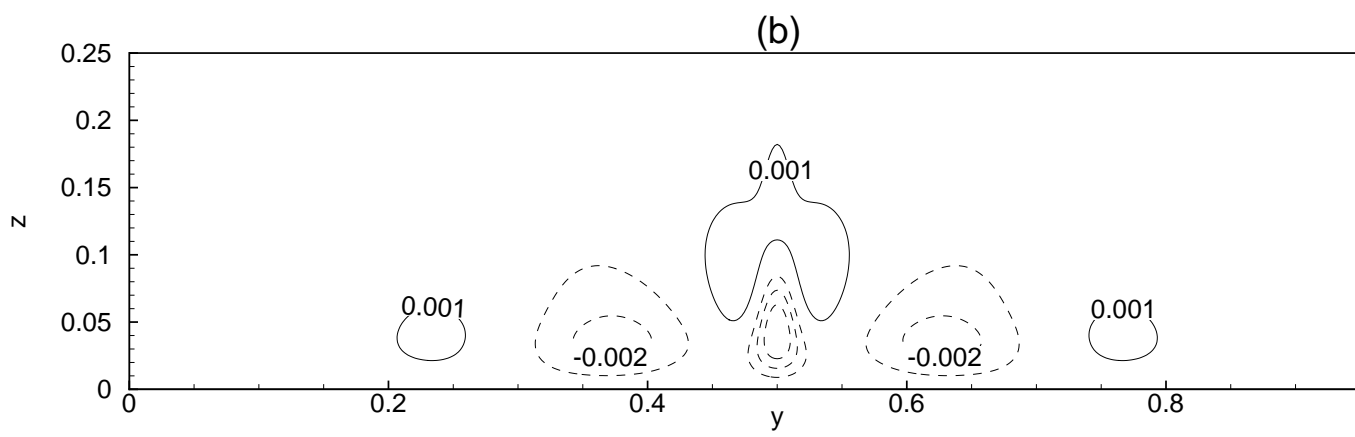


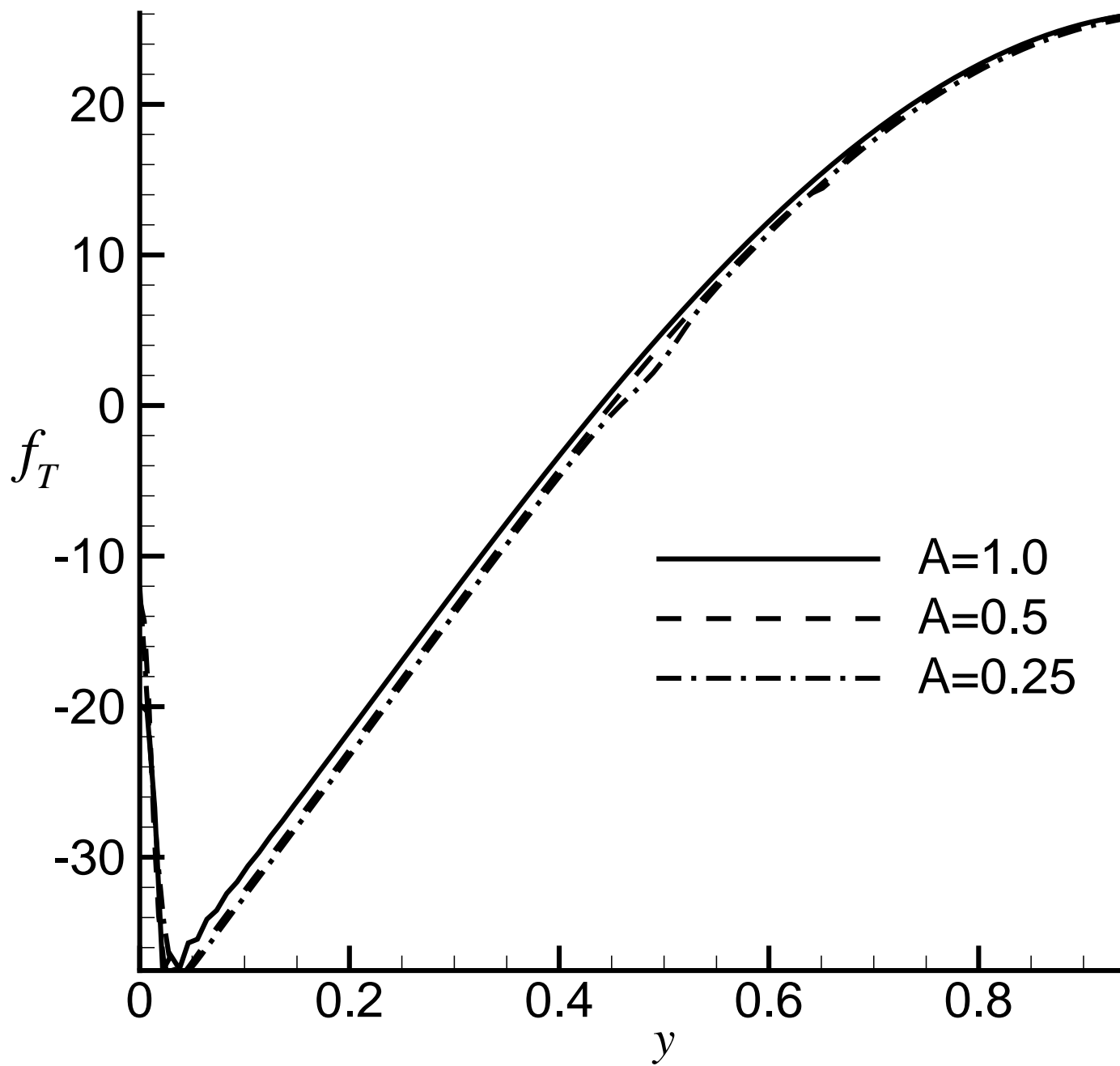
(b)

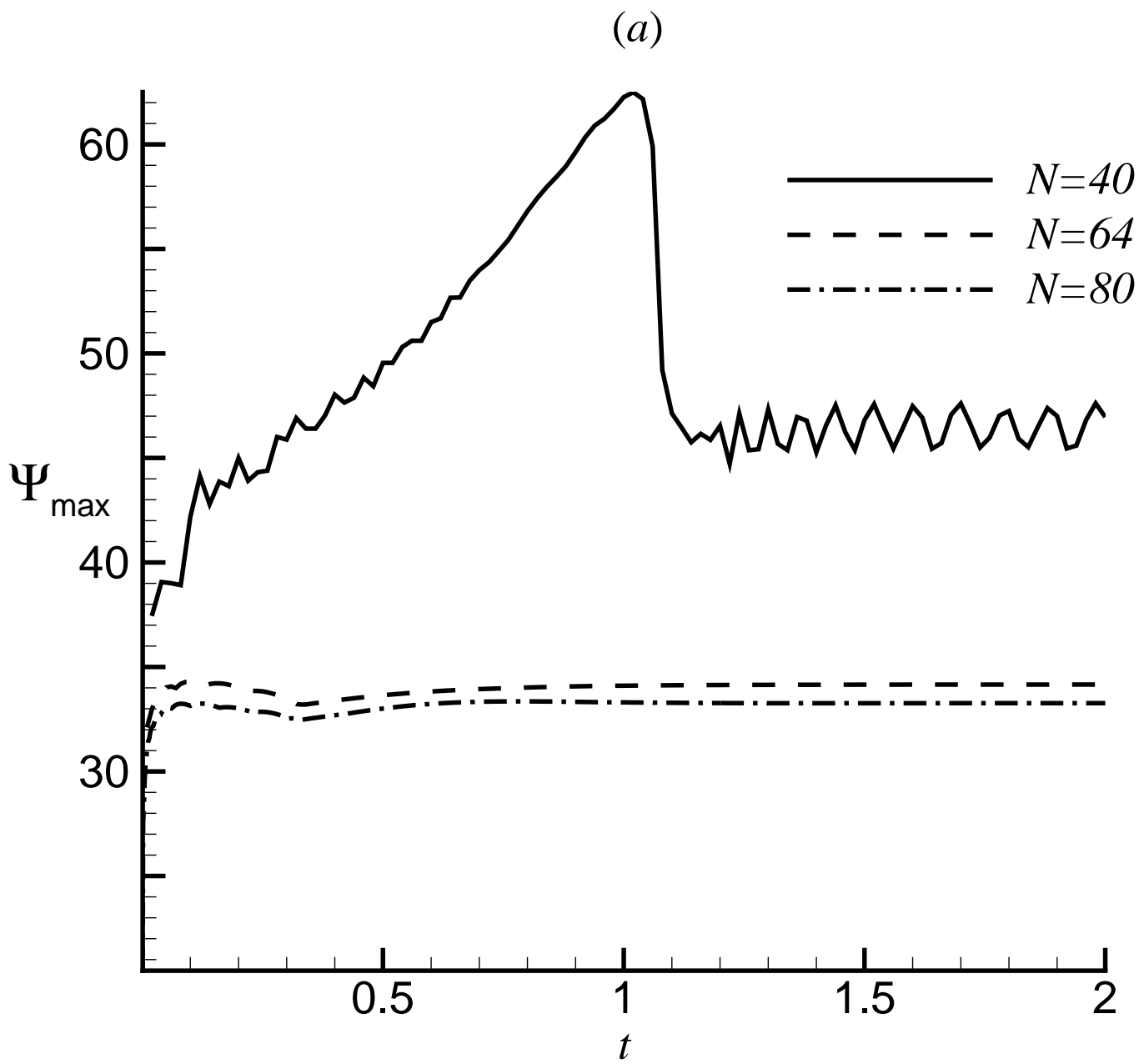


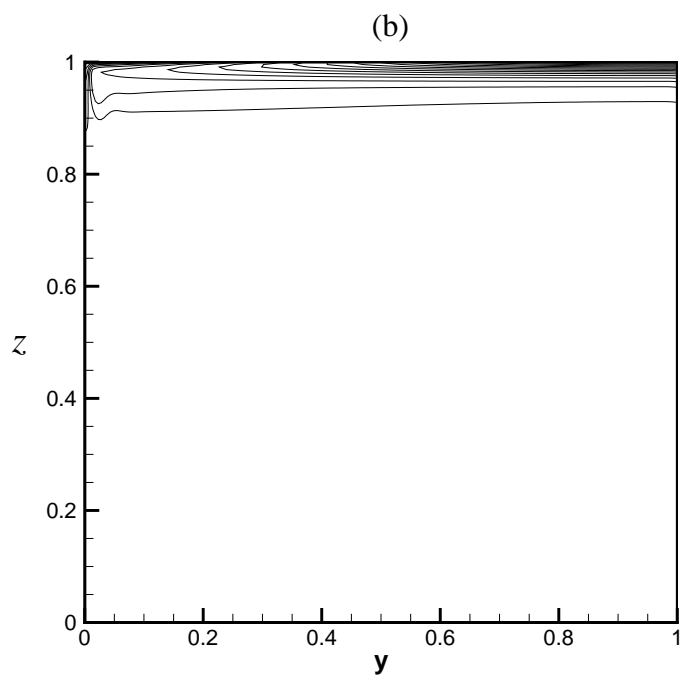
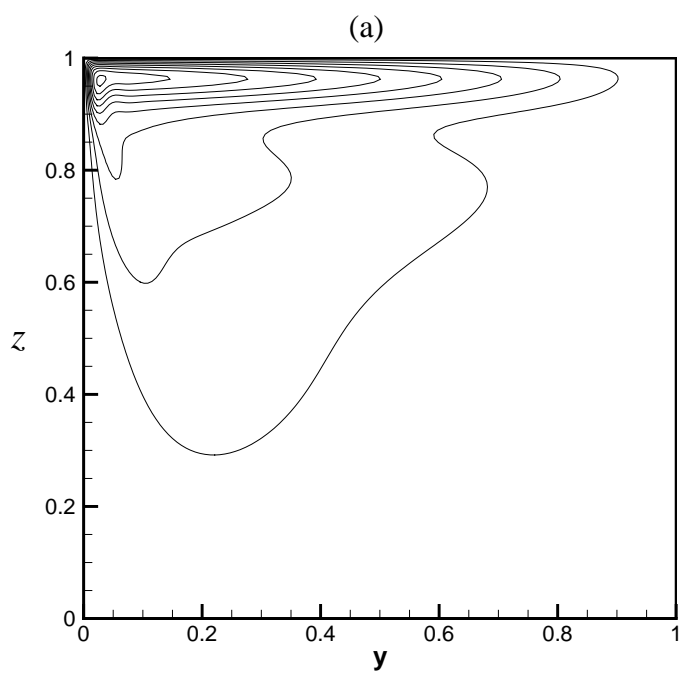


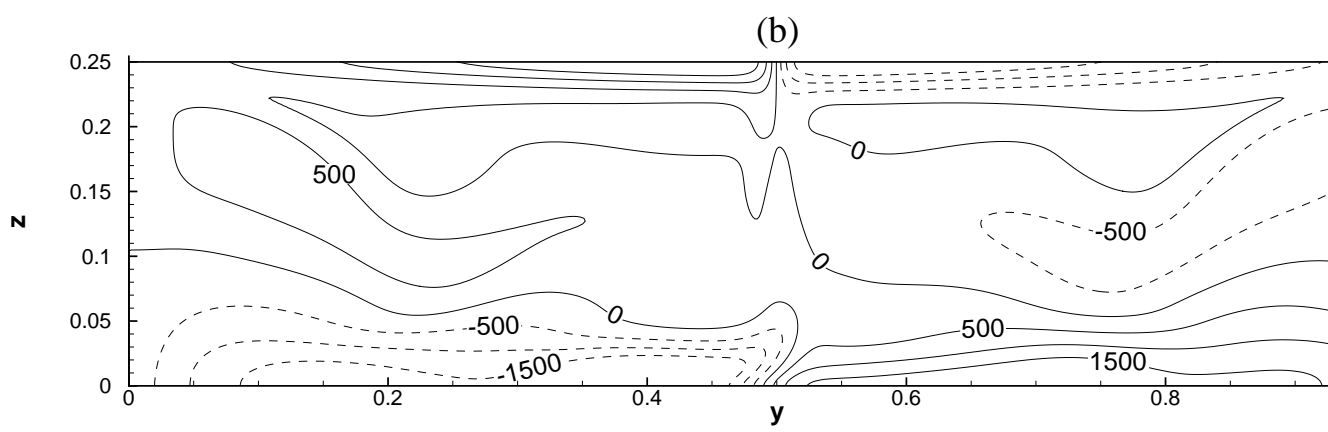
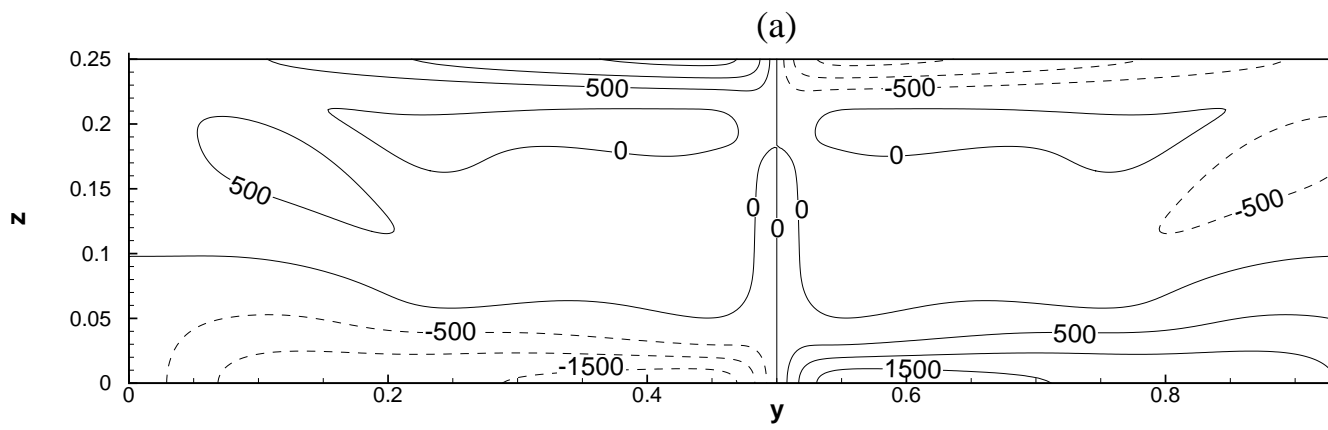


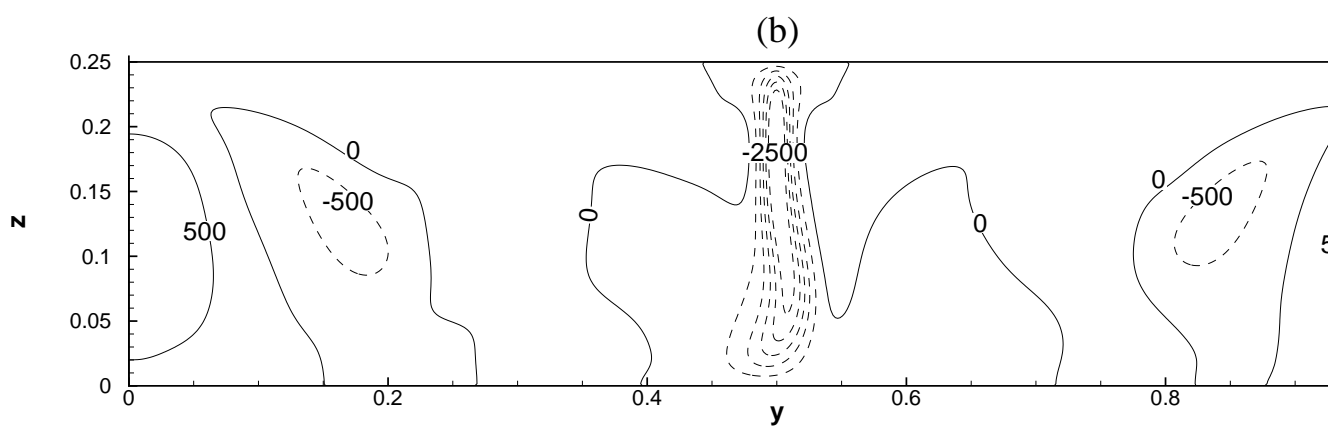
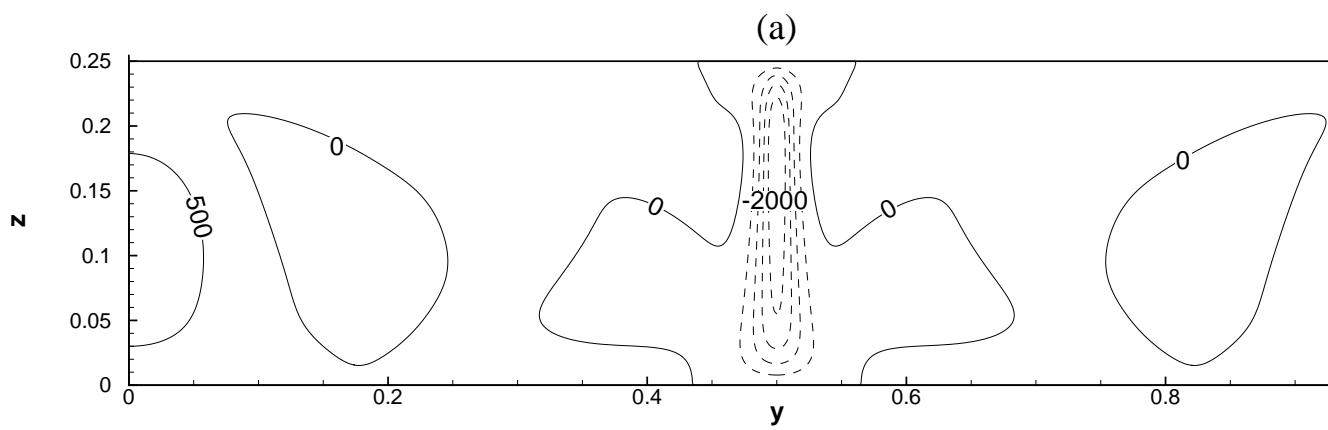


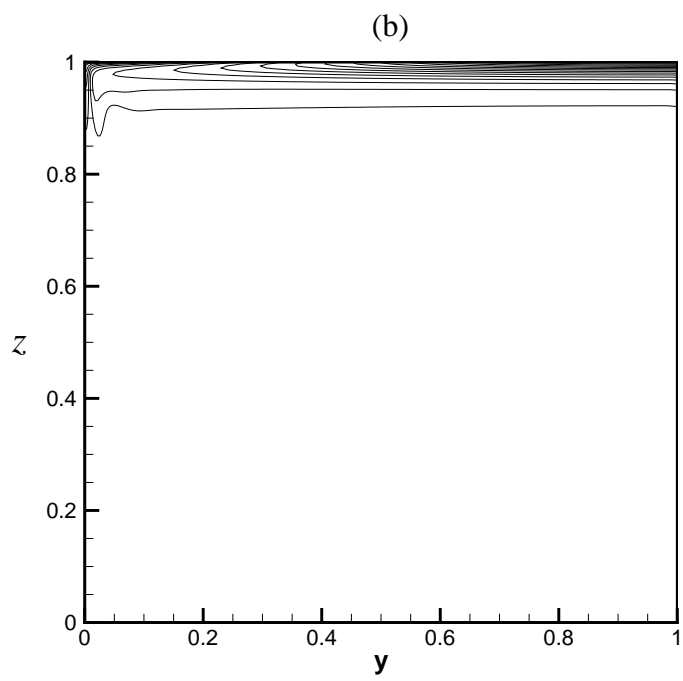
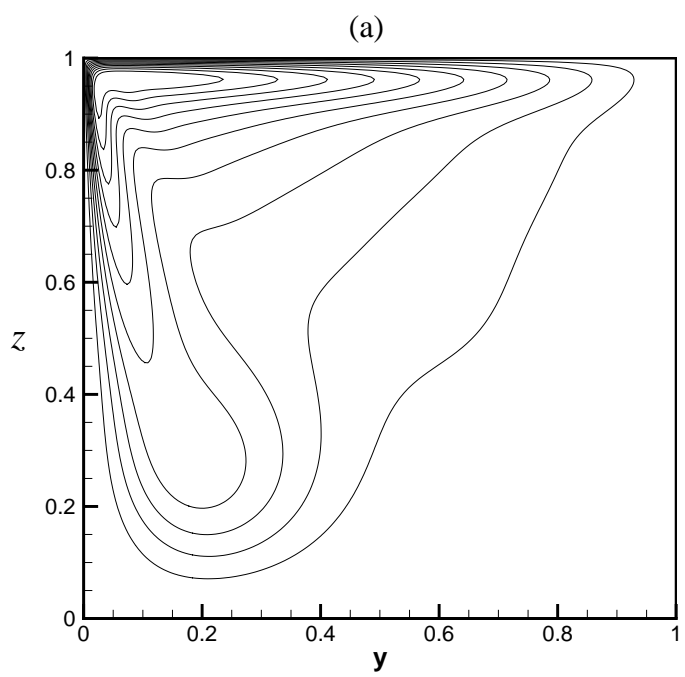


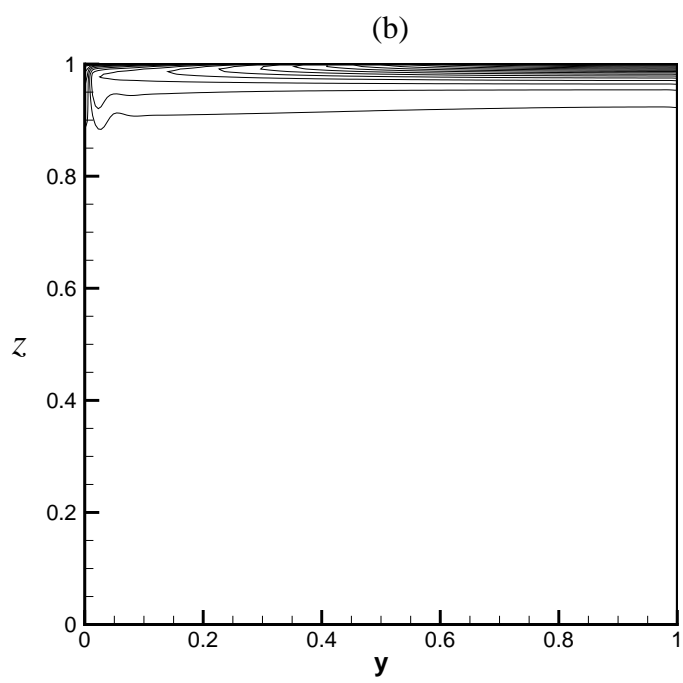
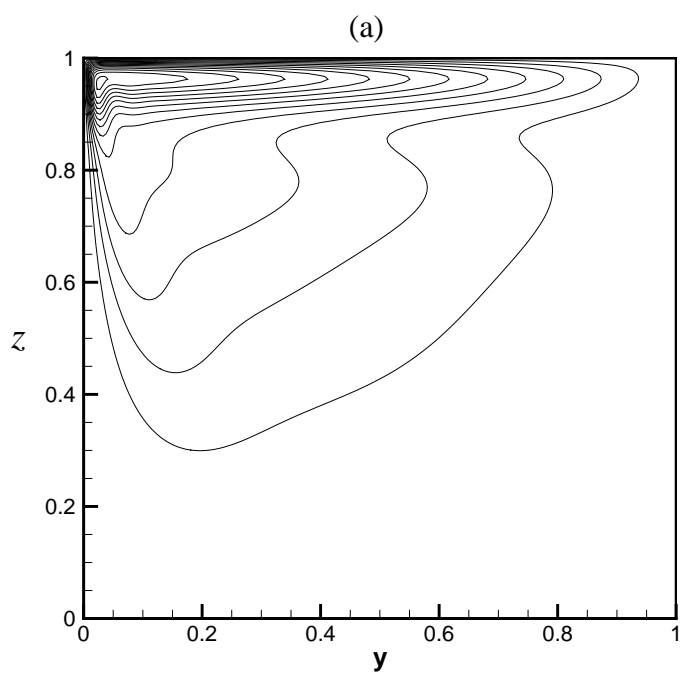


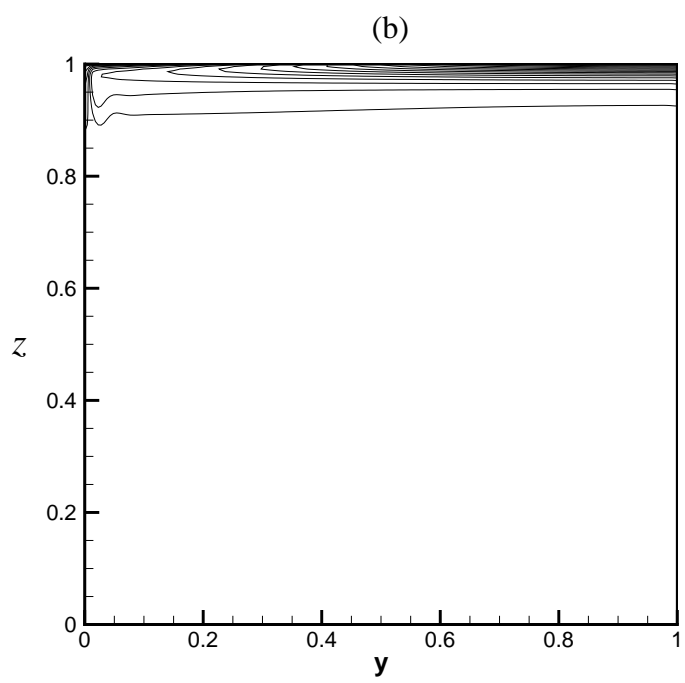
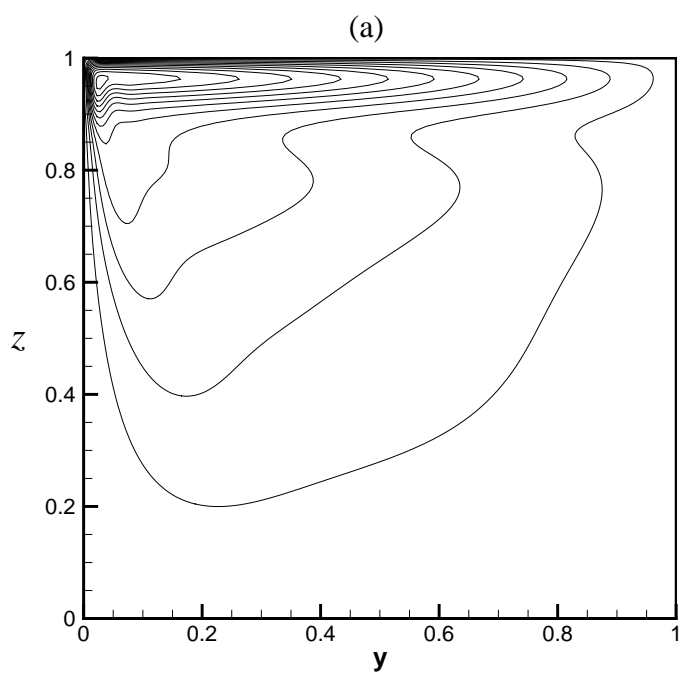


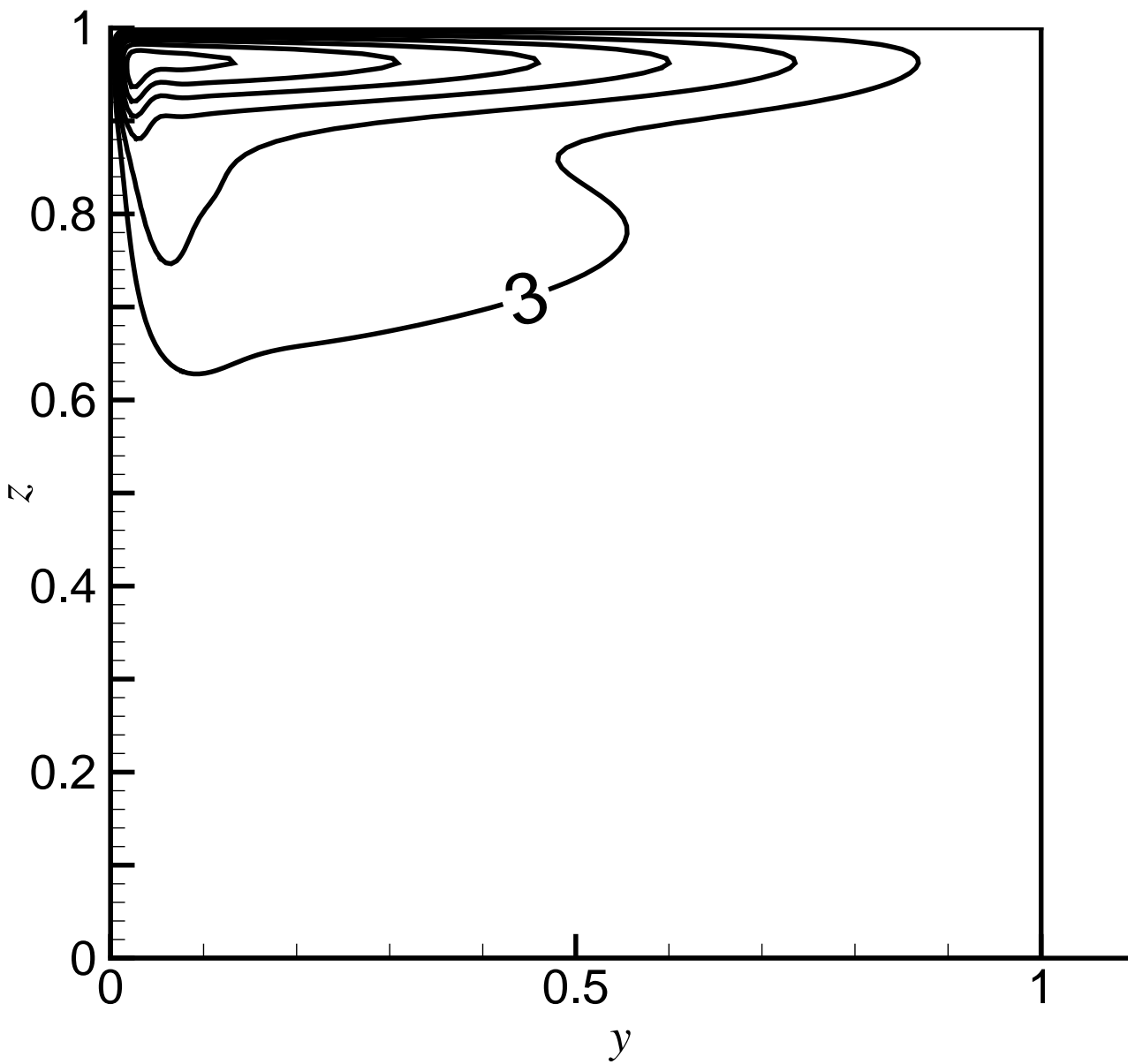


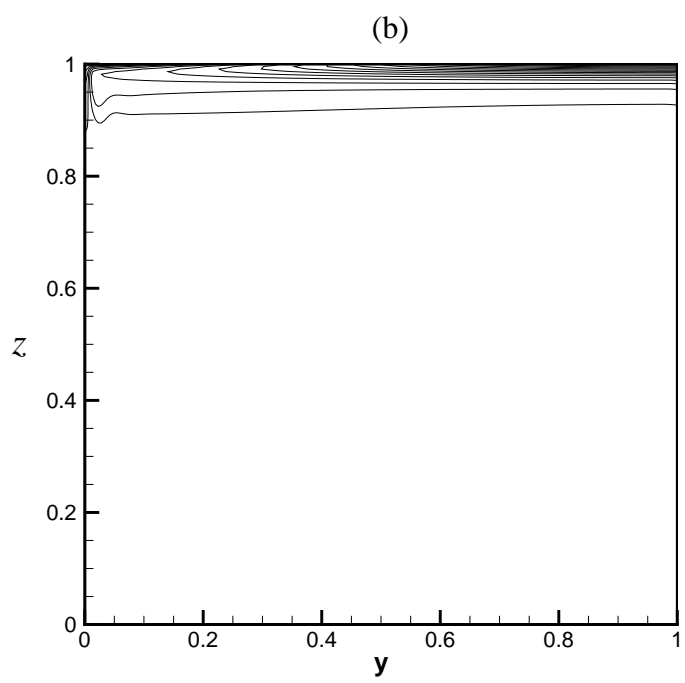
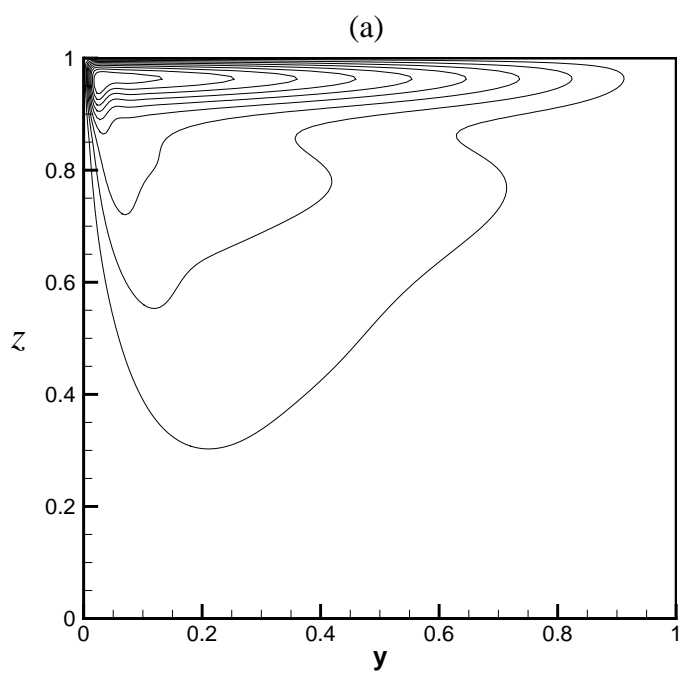


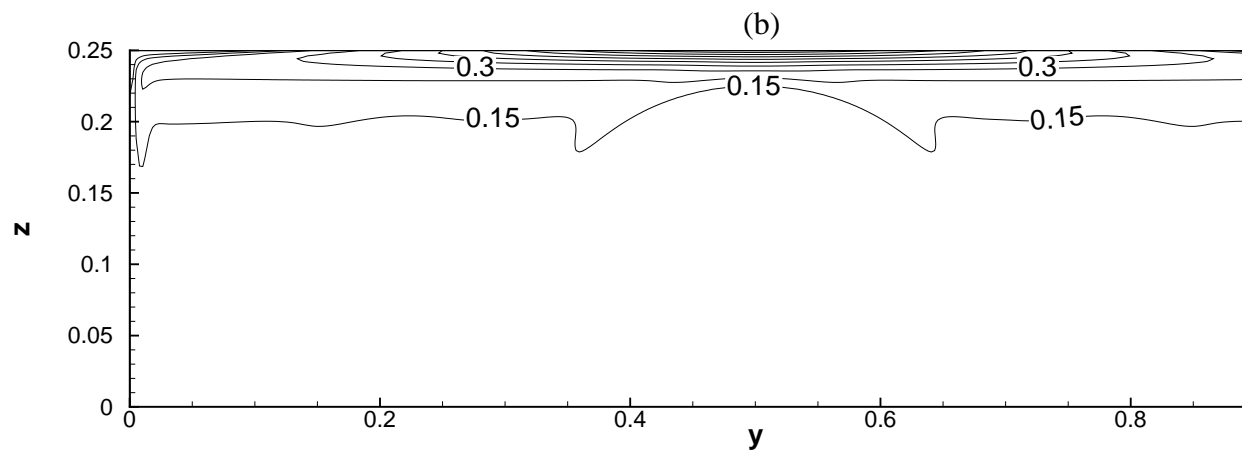
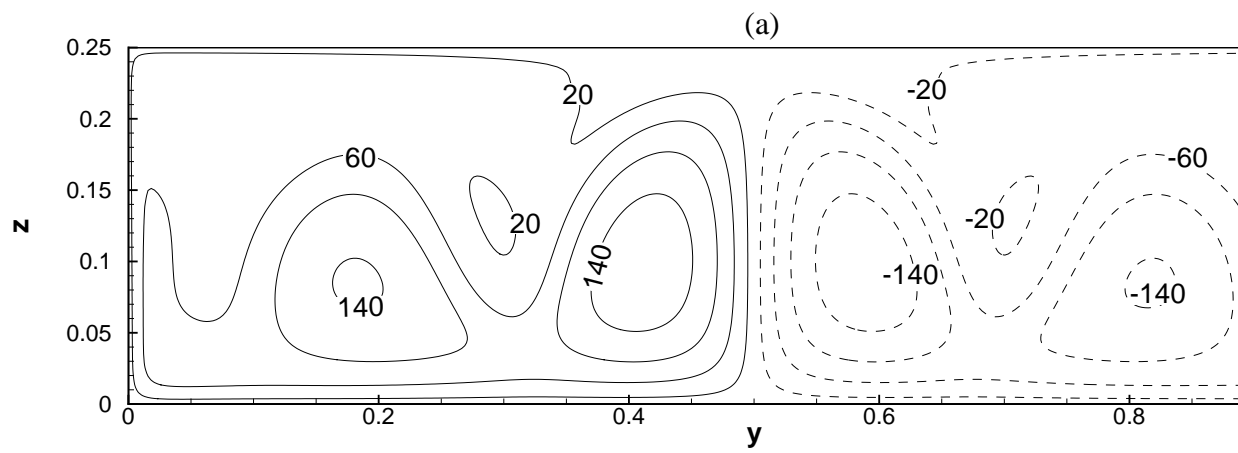


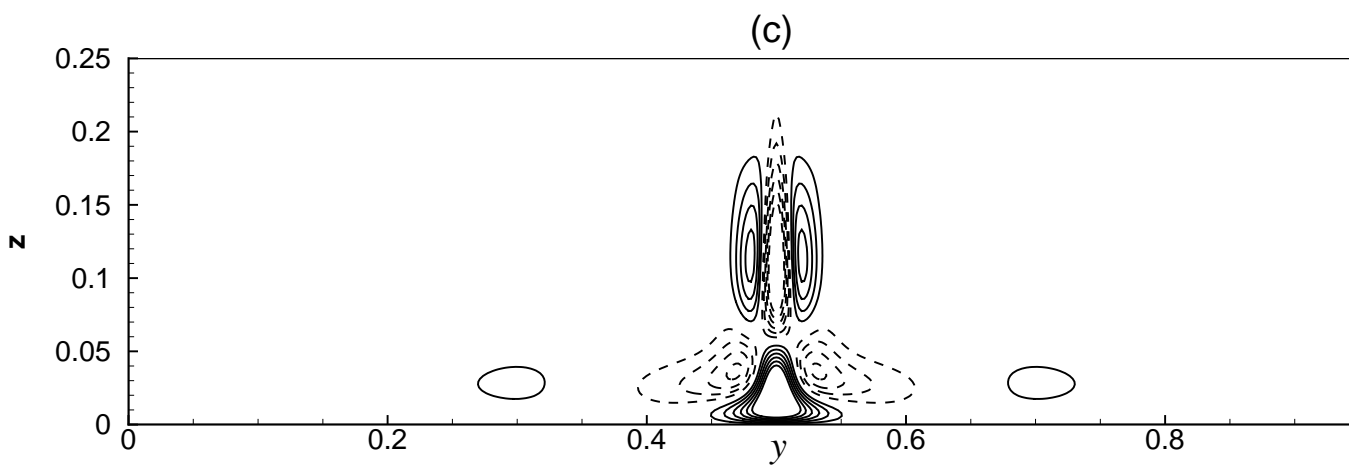
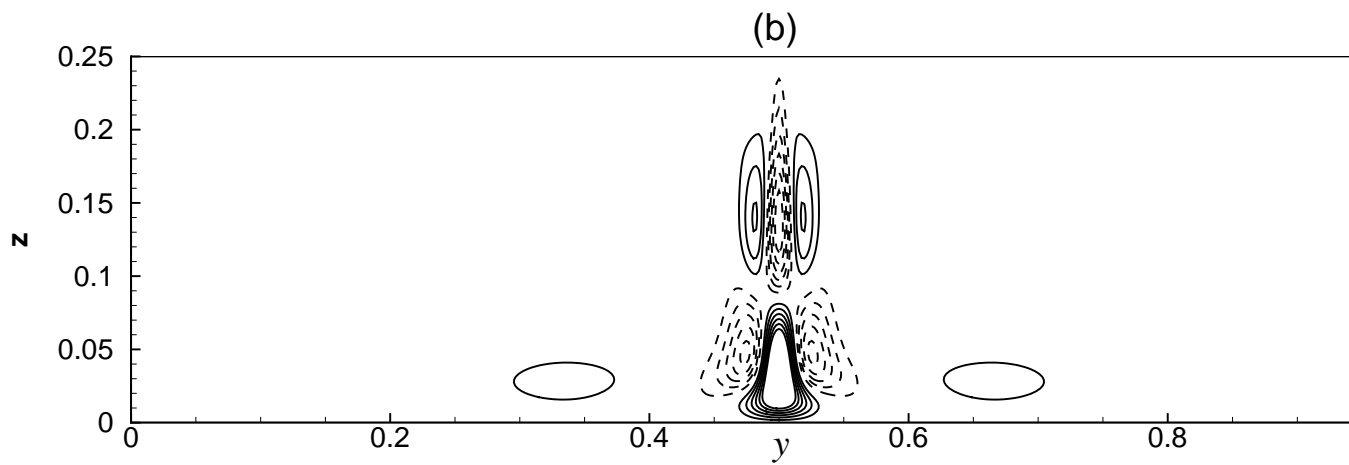
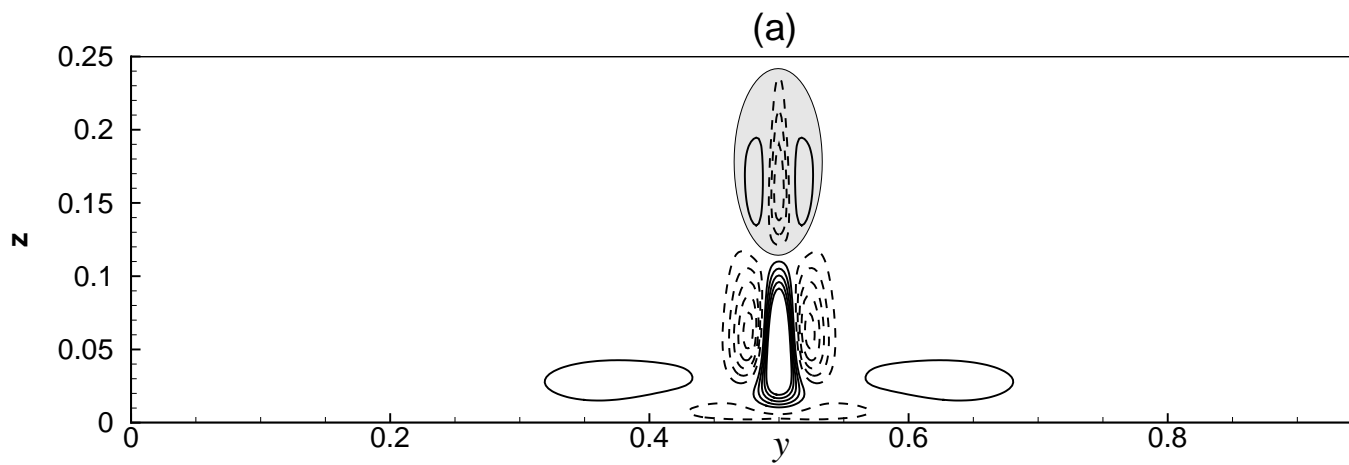


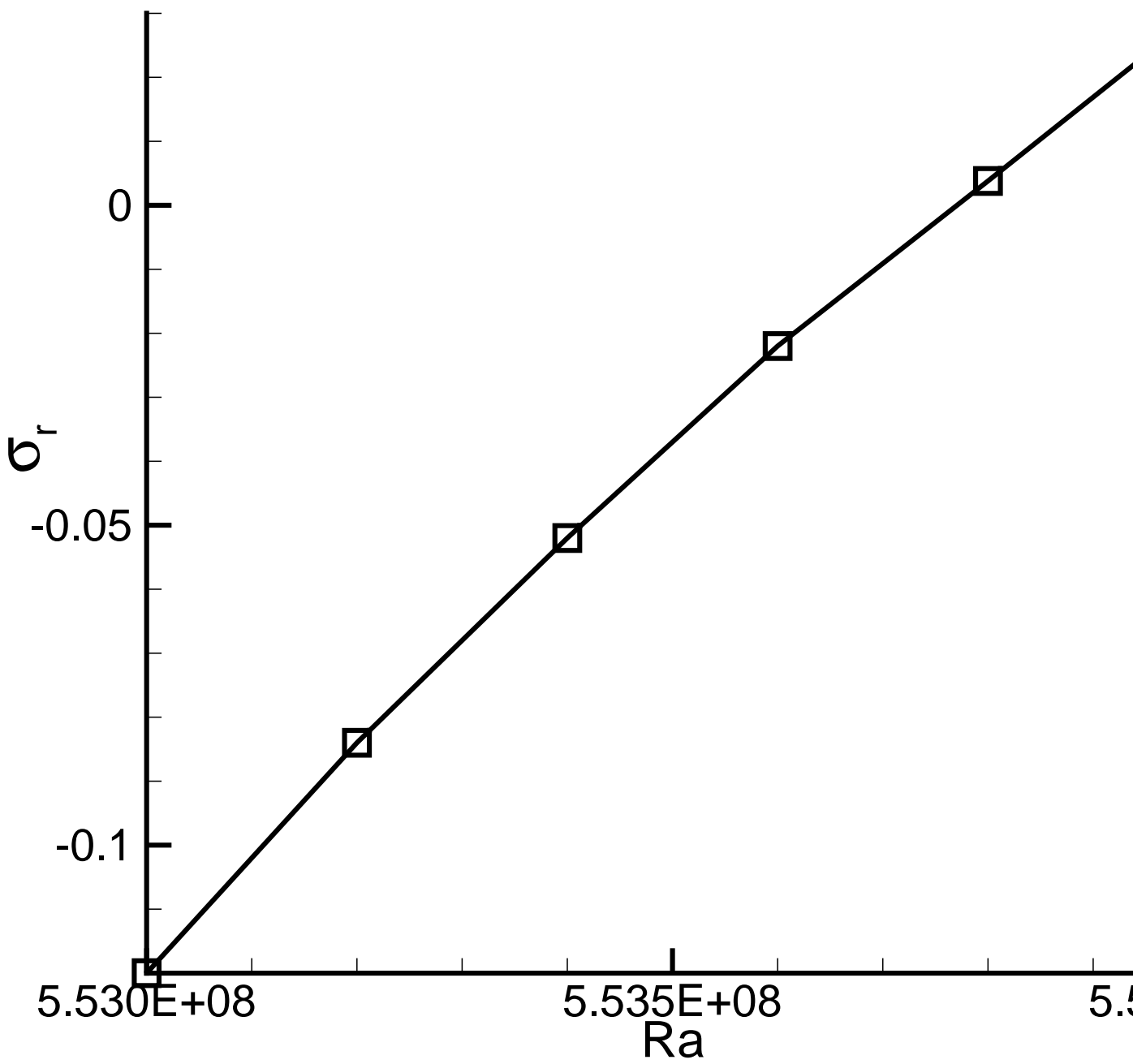


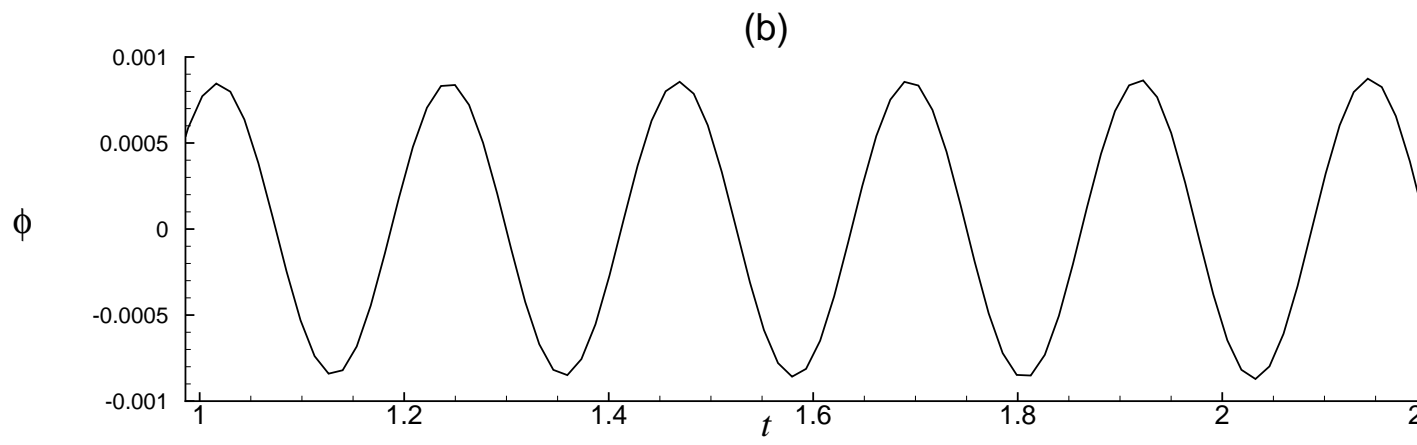
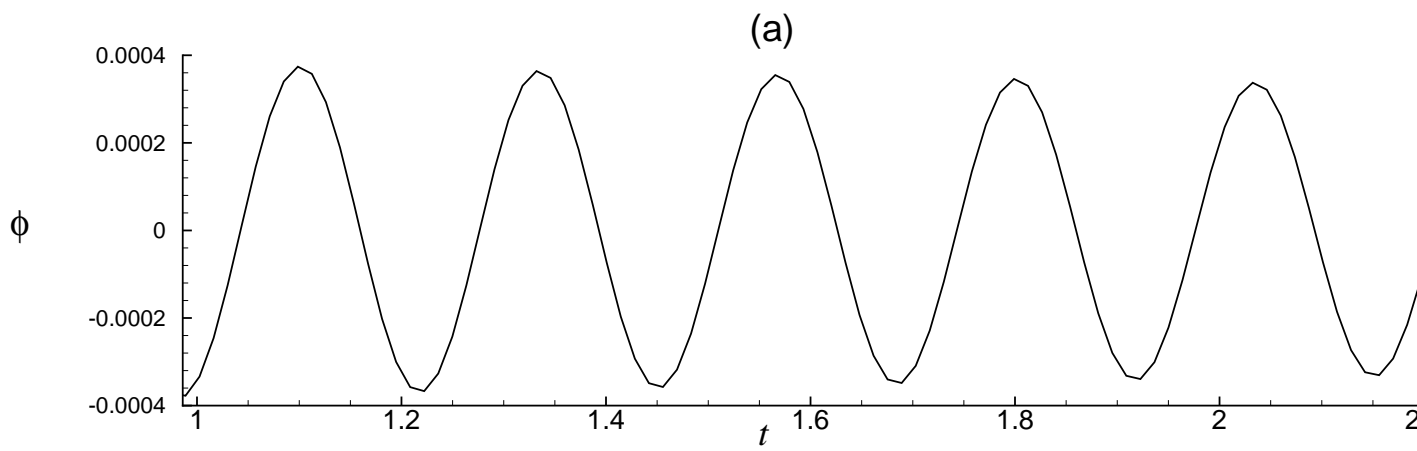


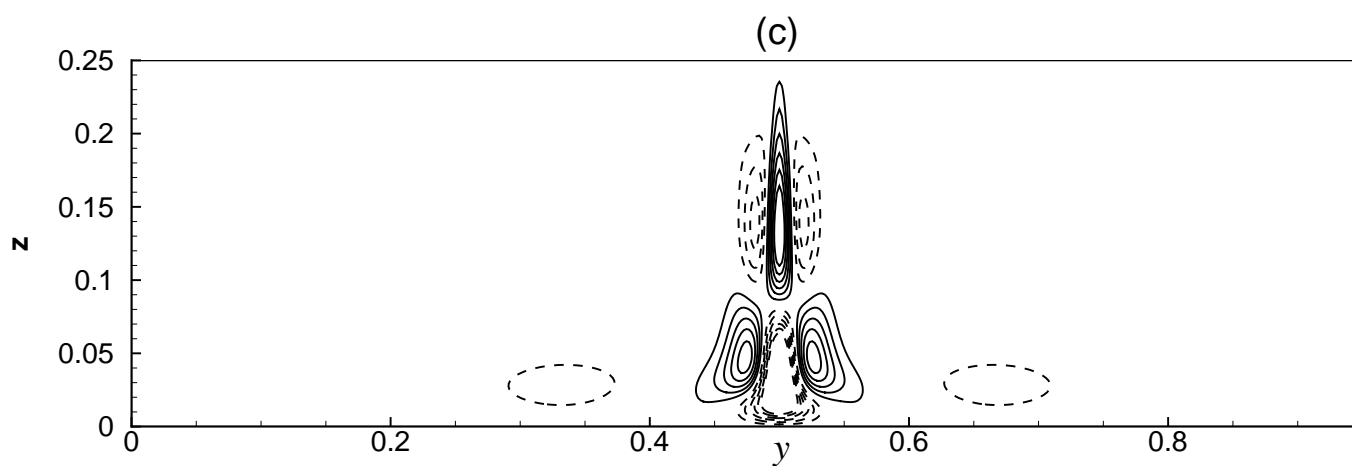
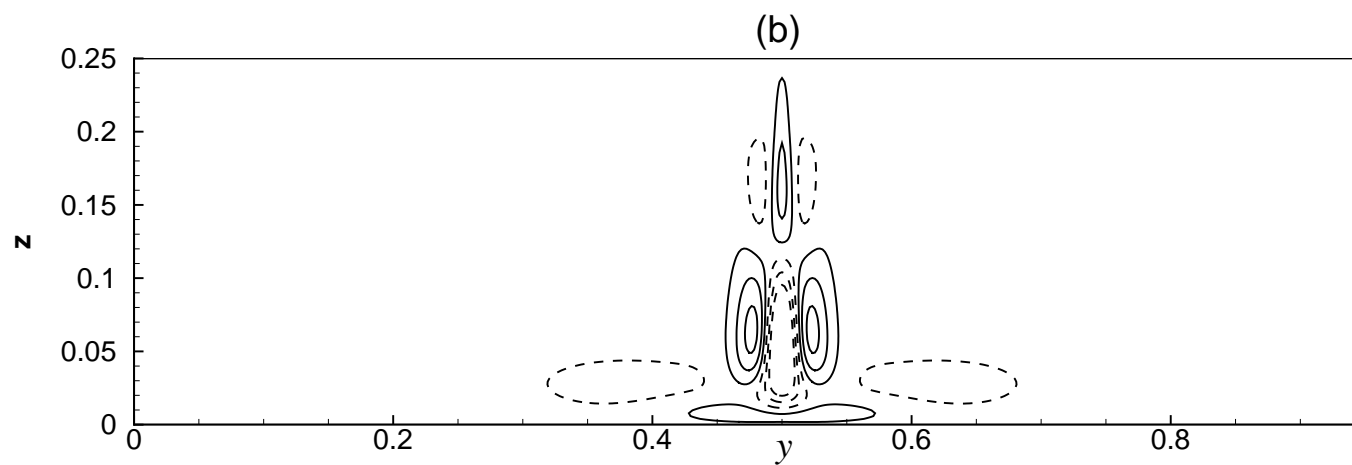
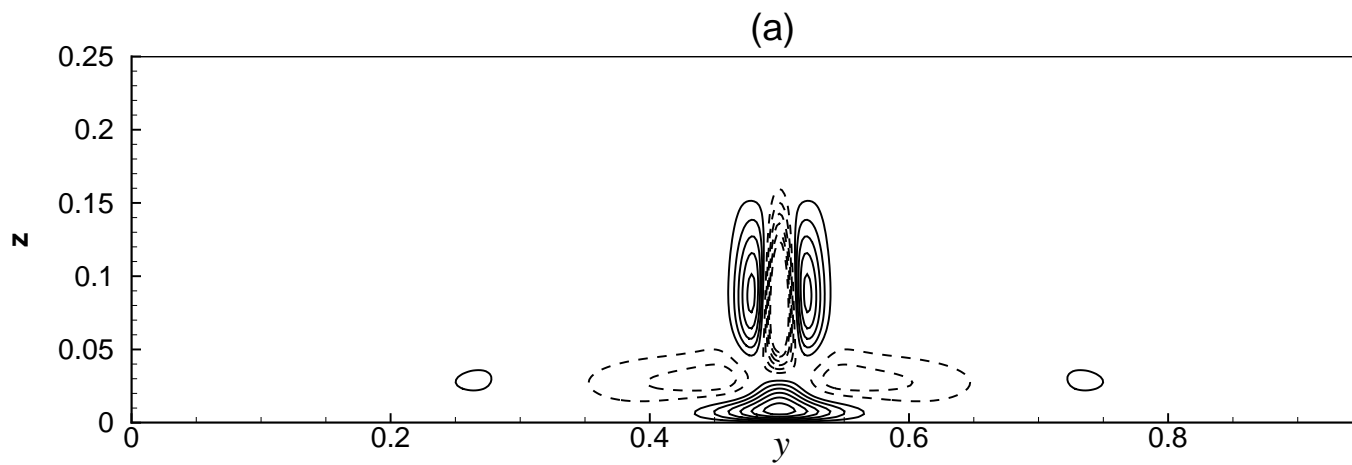


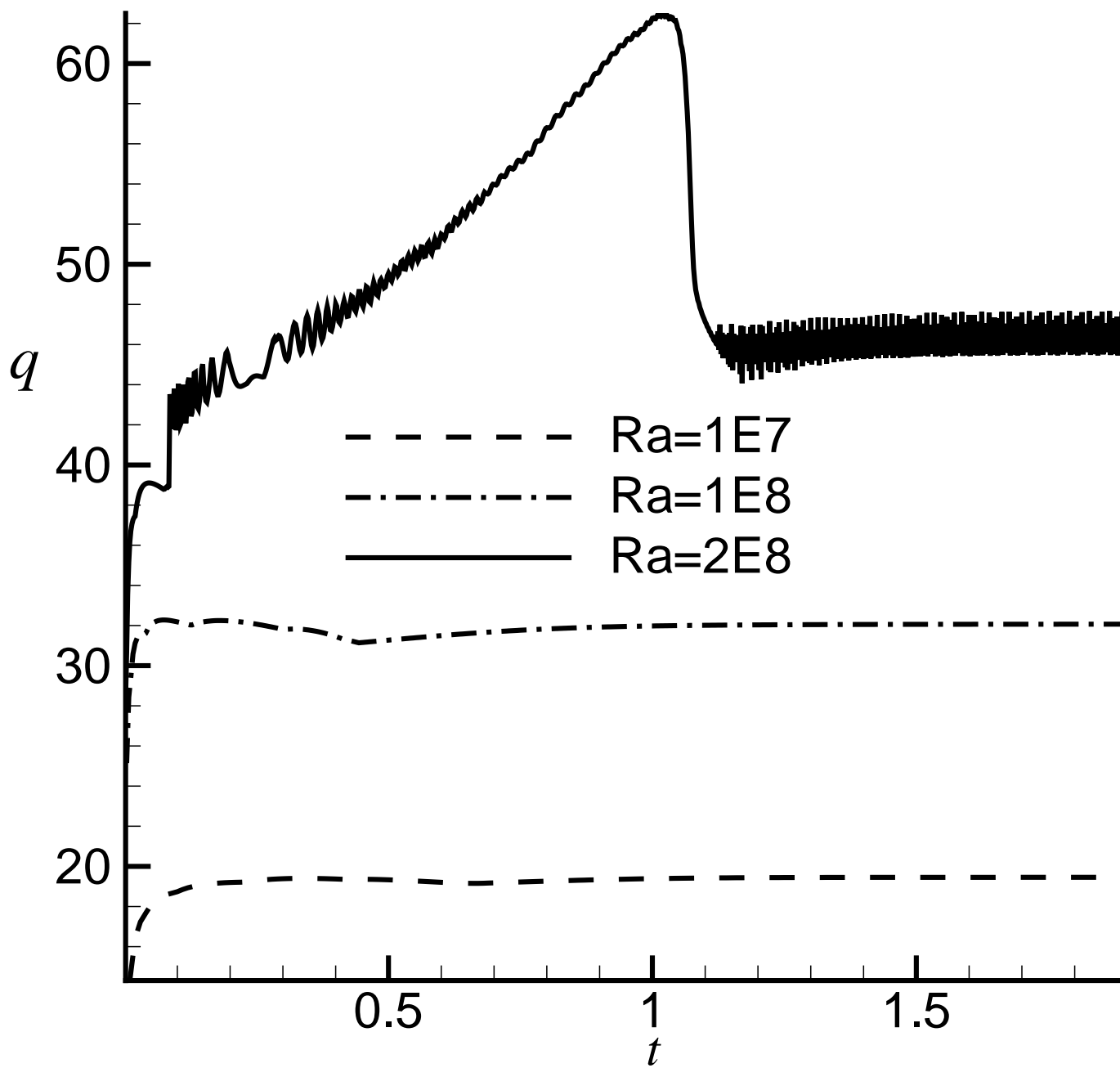


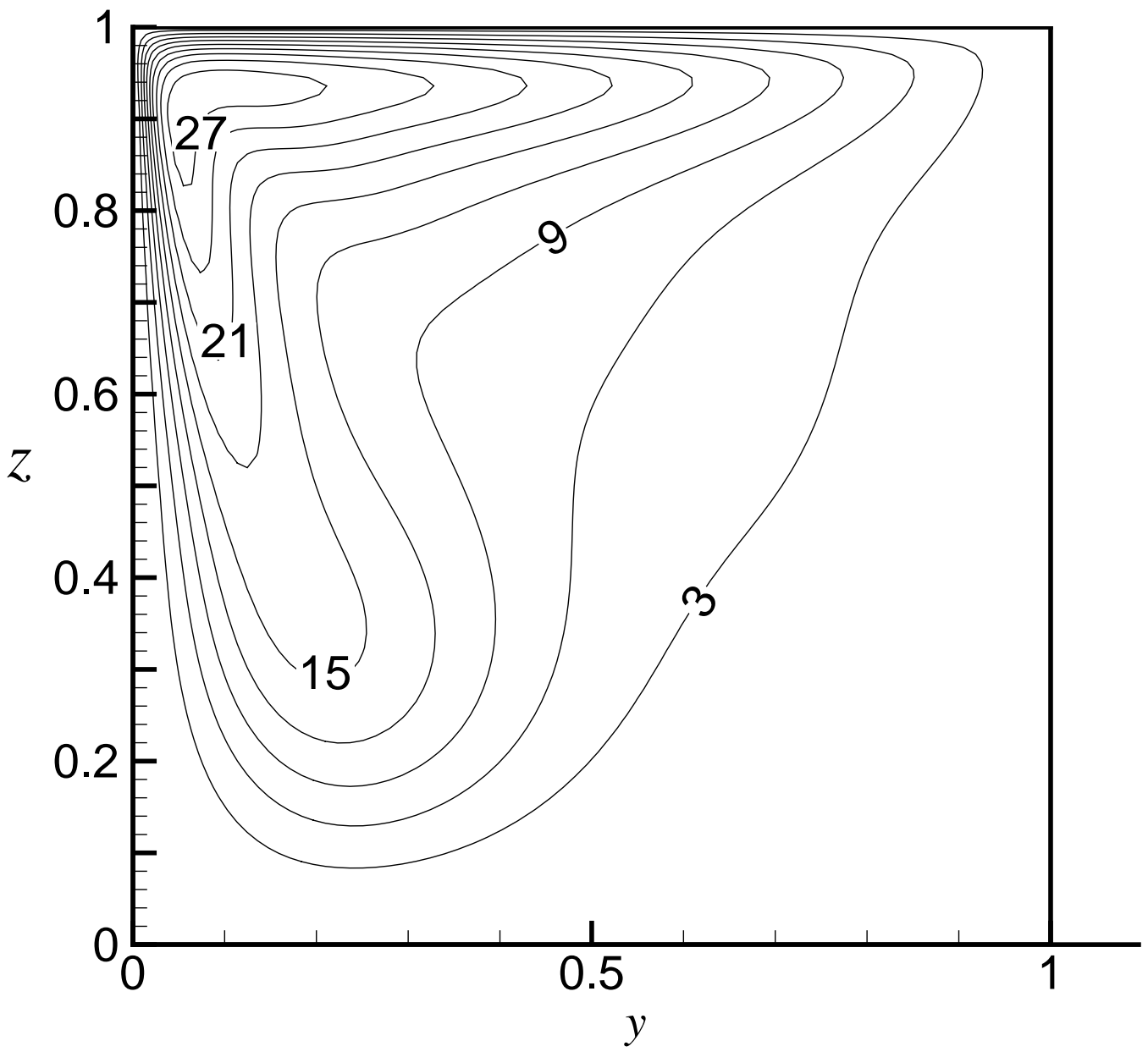


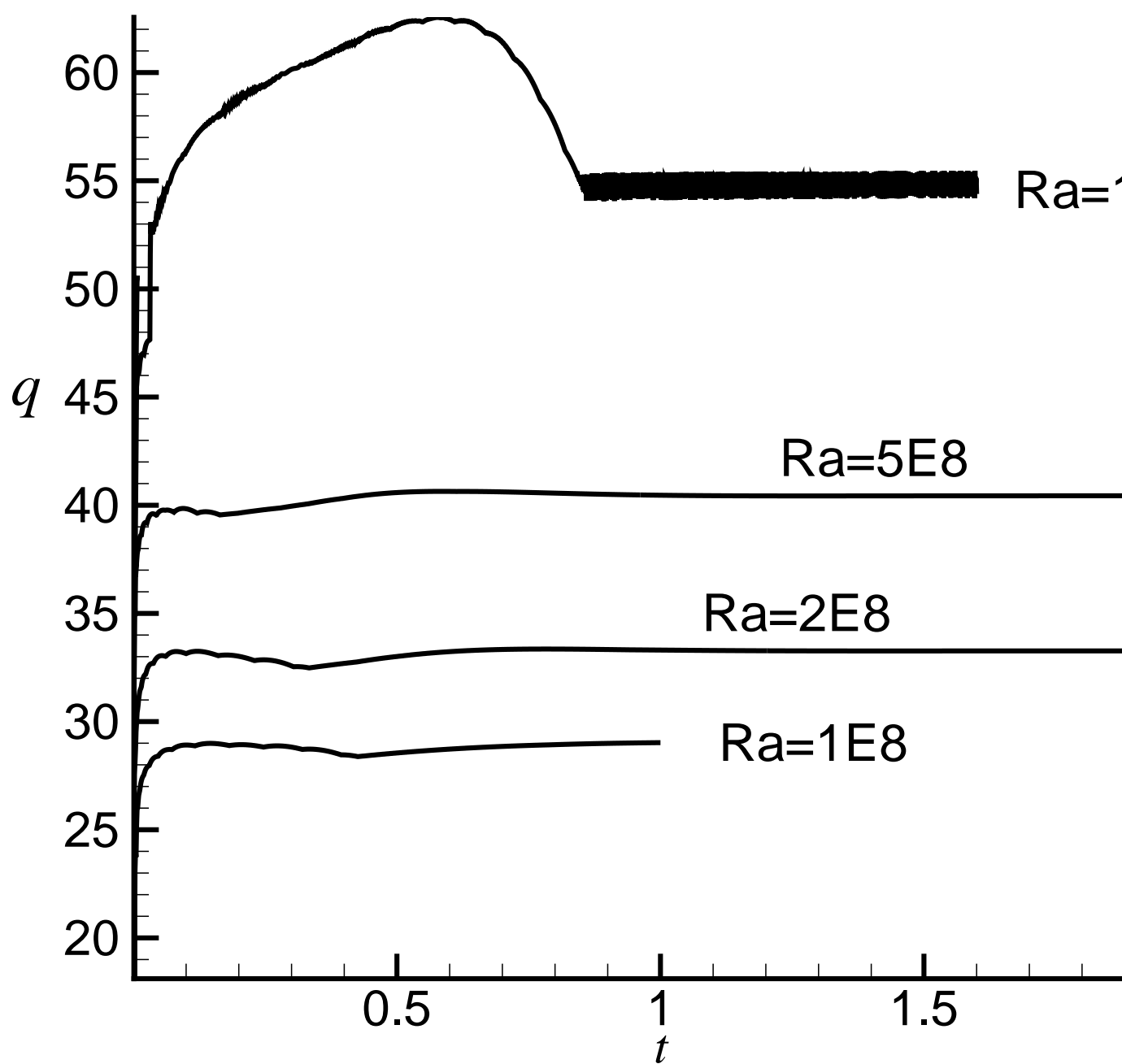


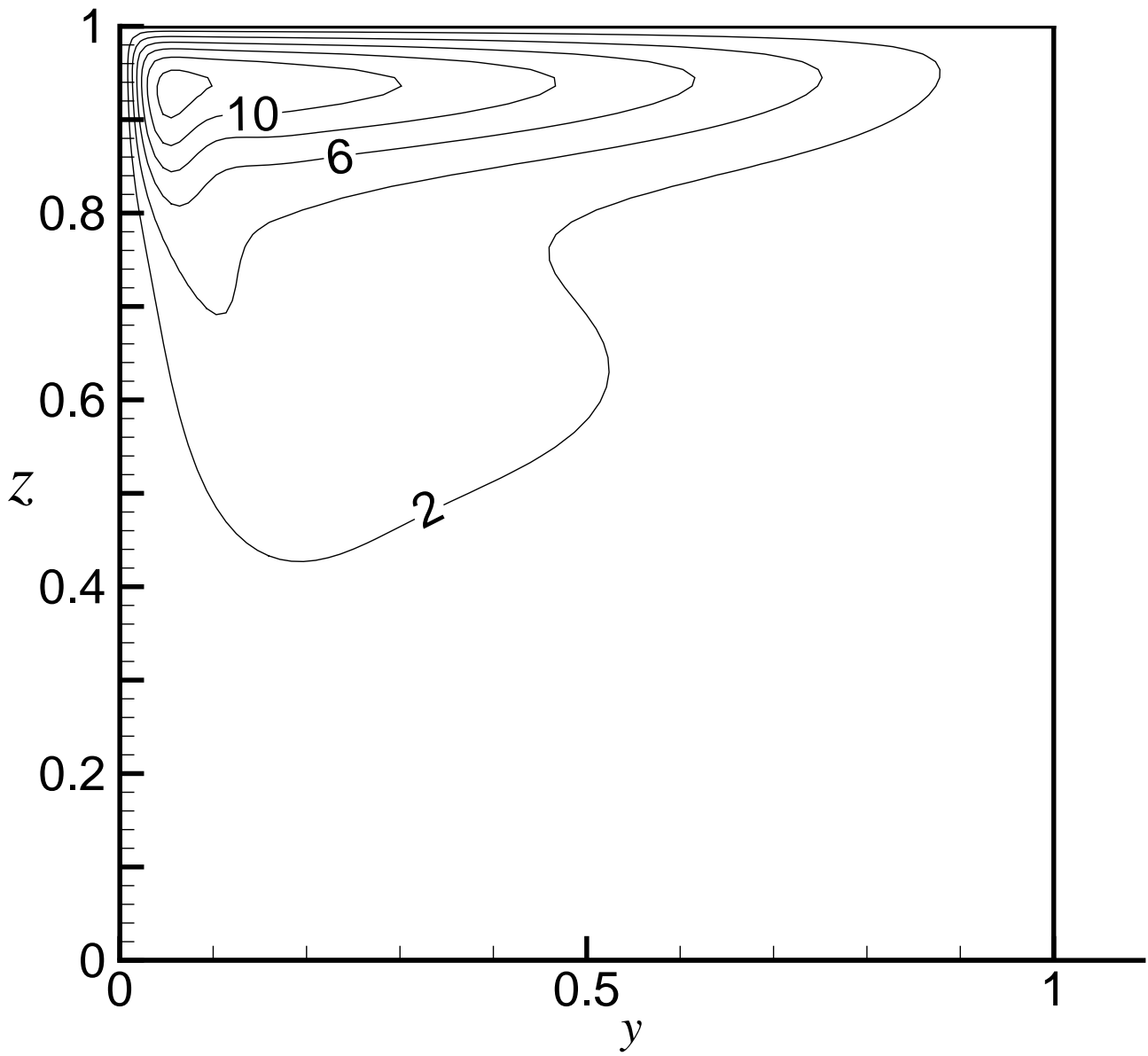




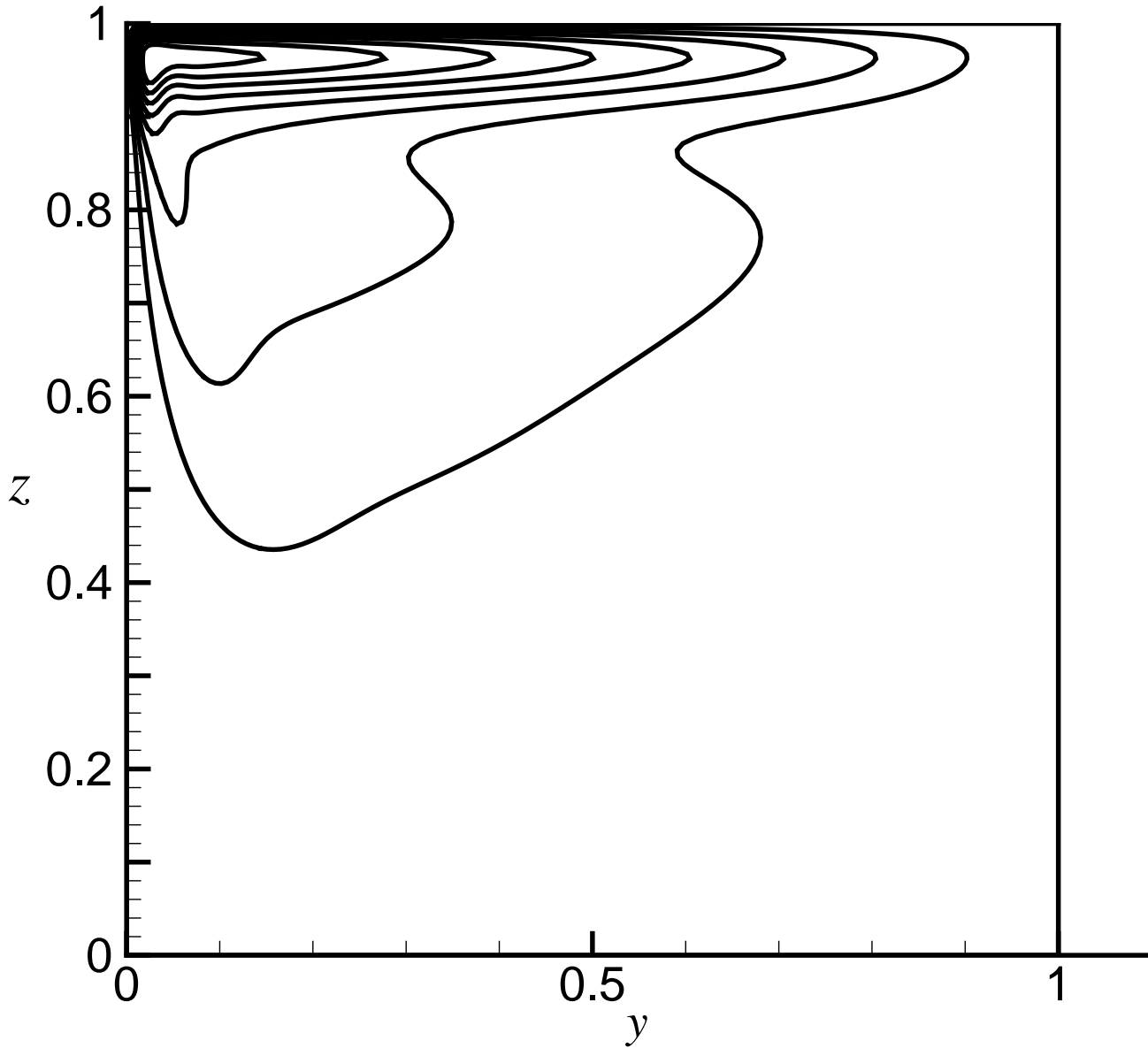




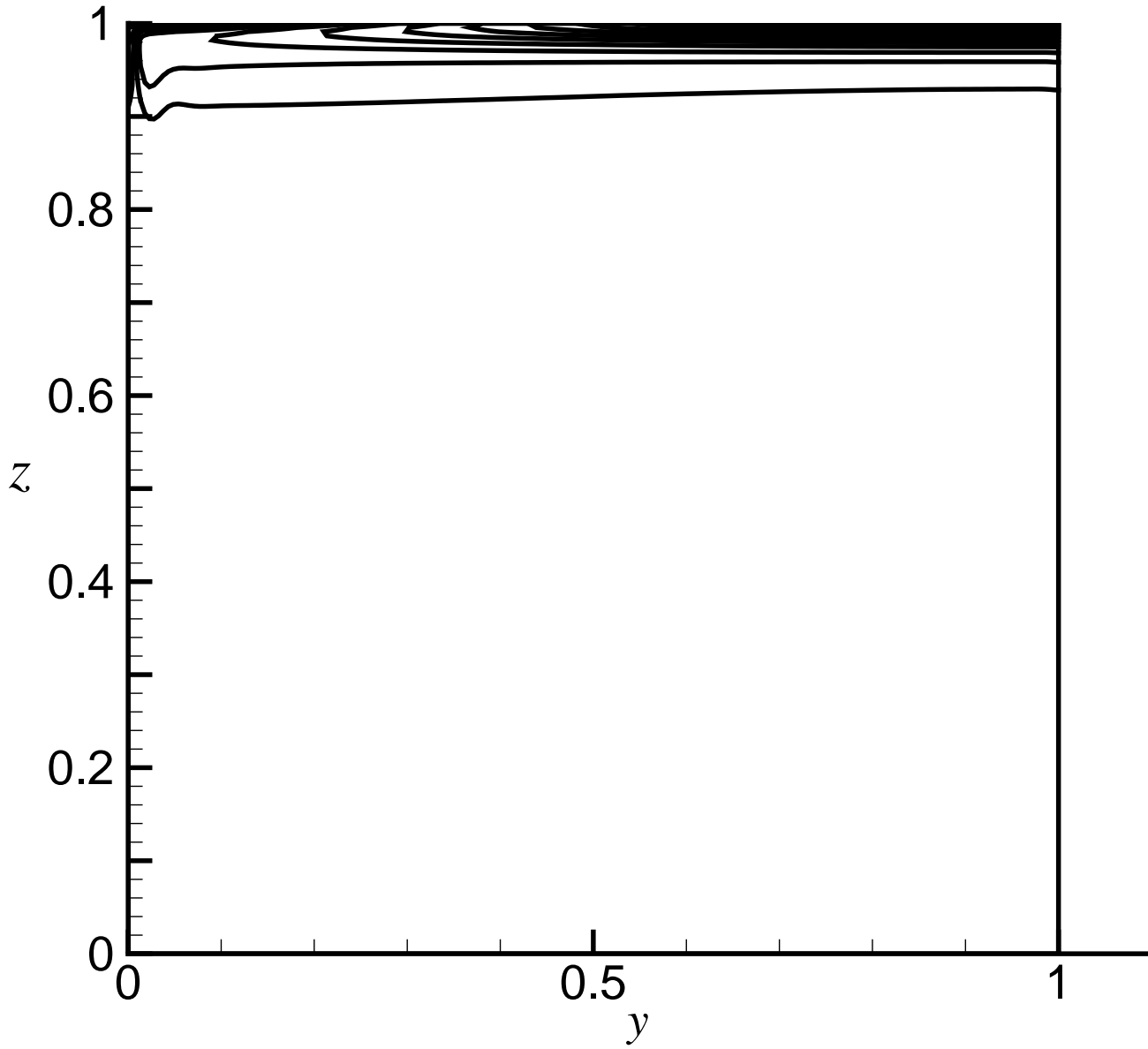




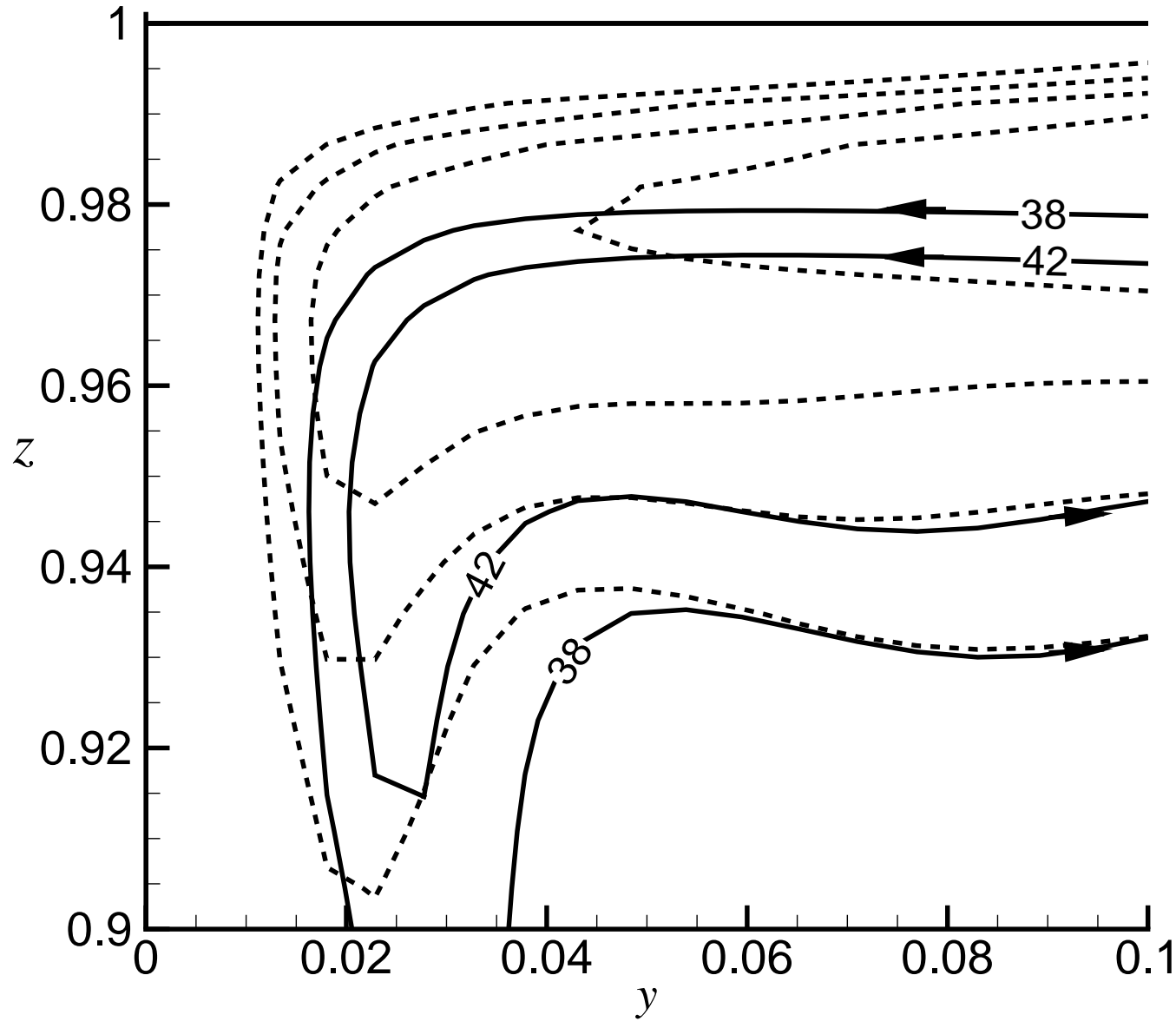
(a)



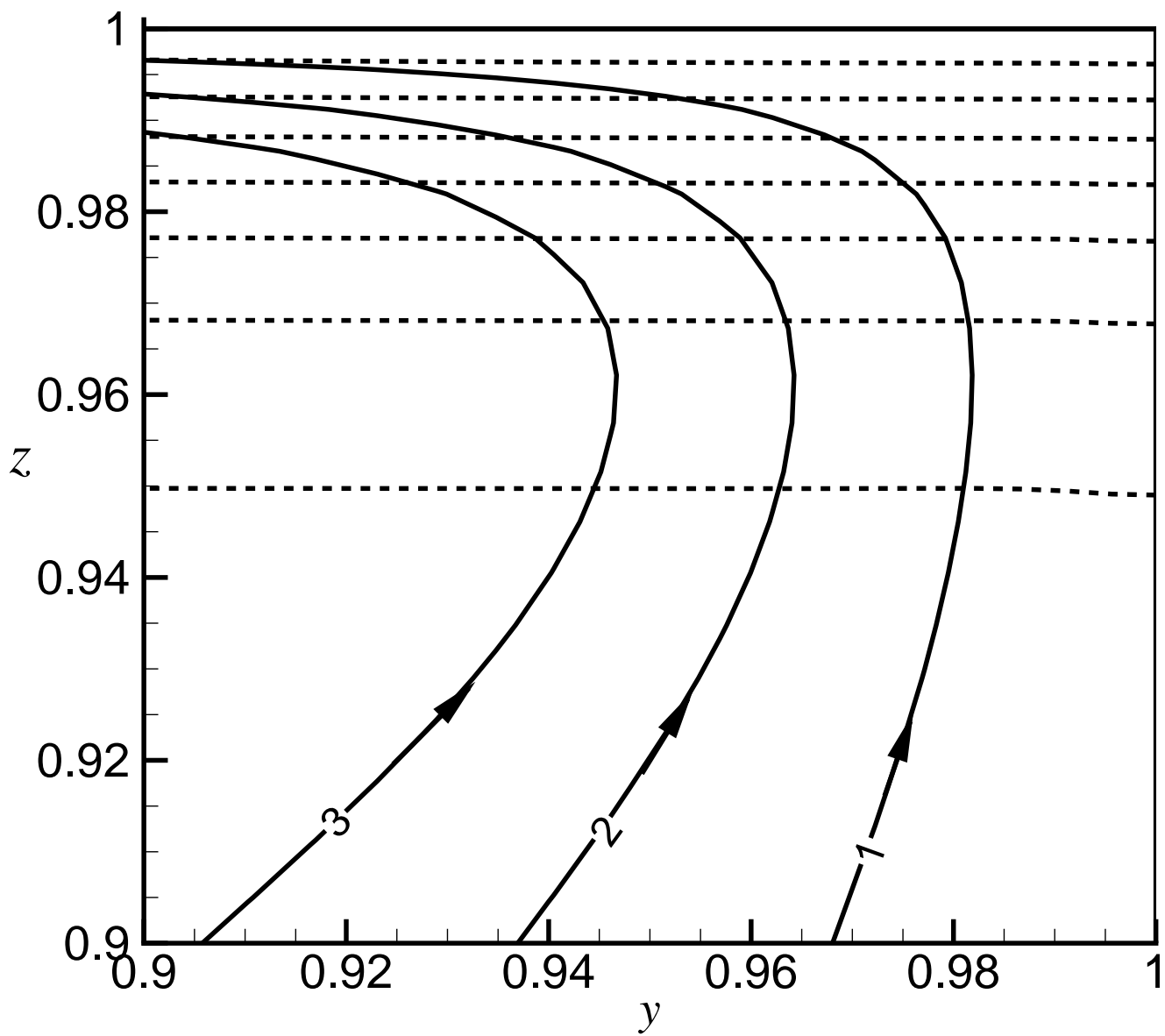
(b)



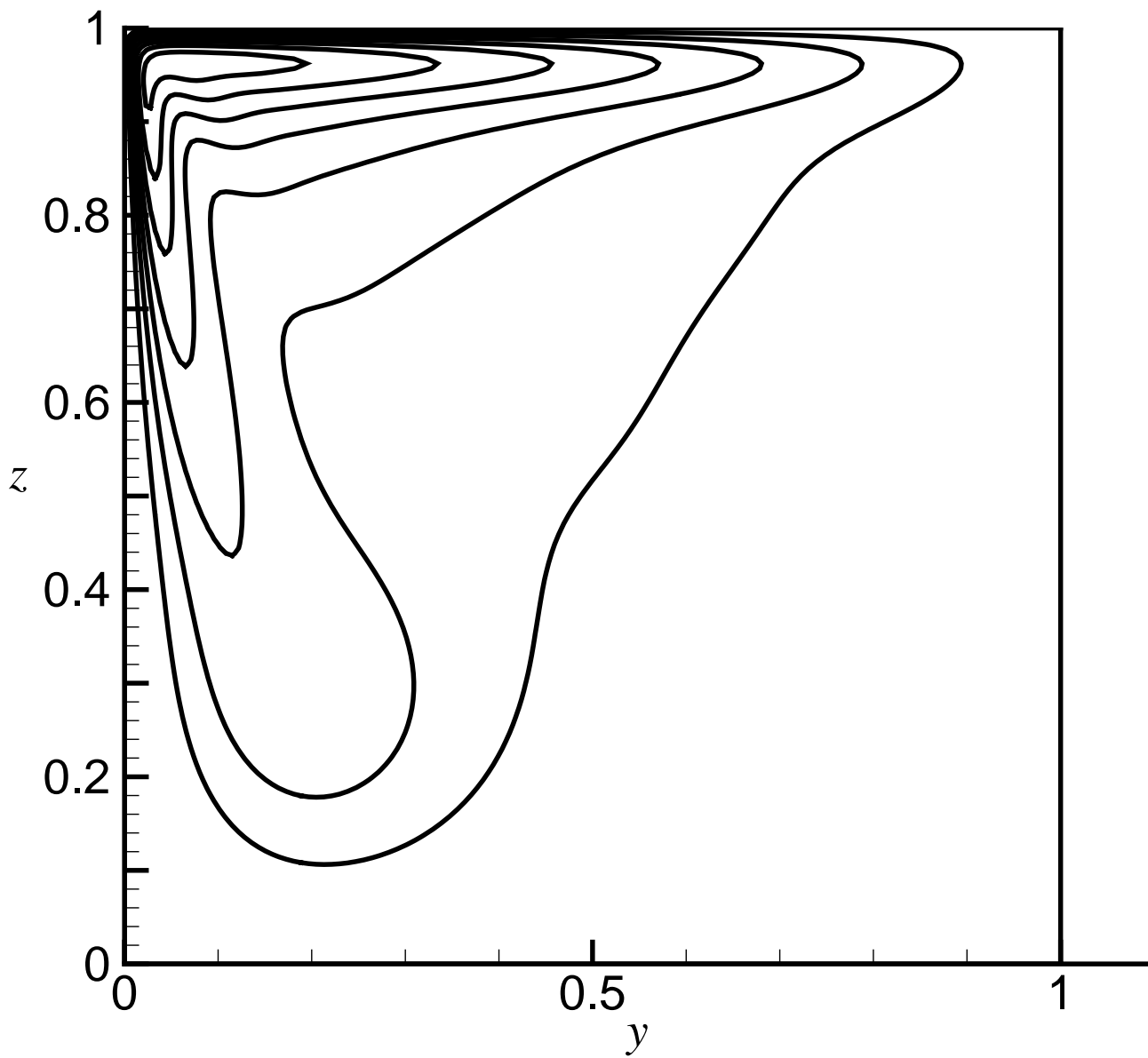
(a)

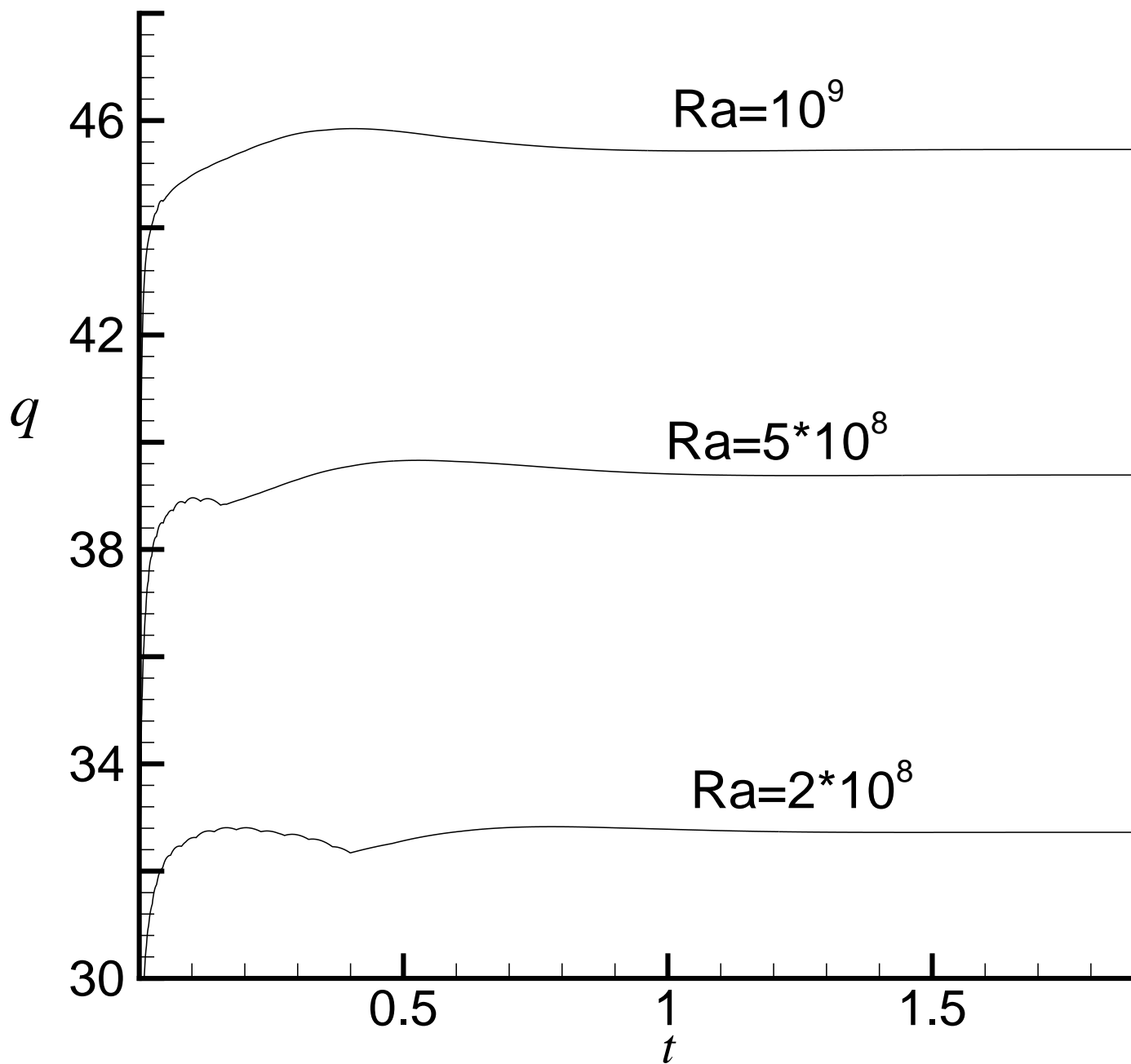


(b)

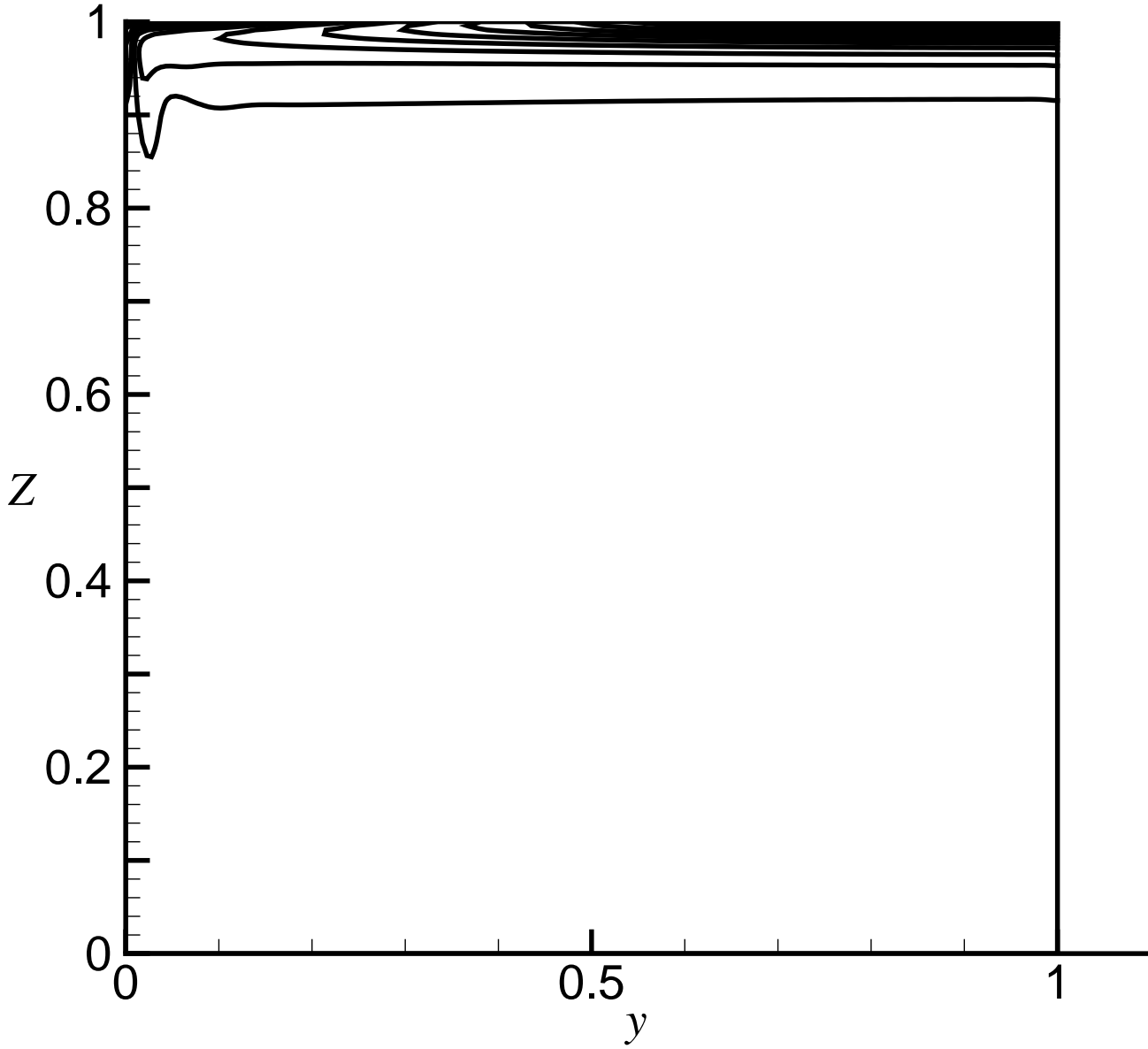


(a)

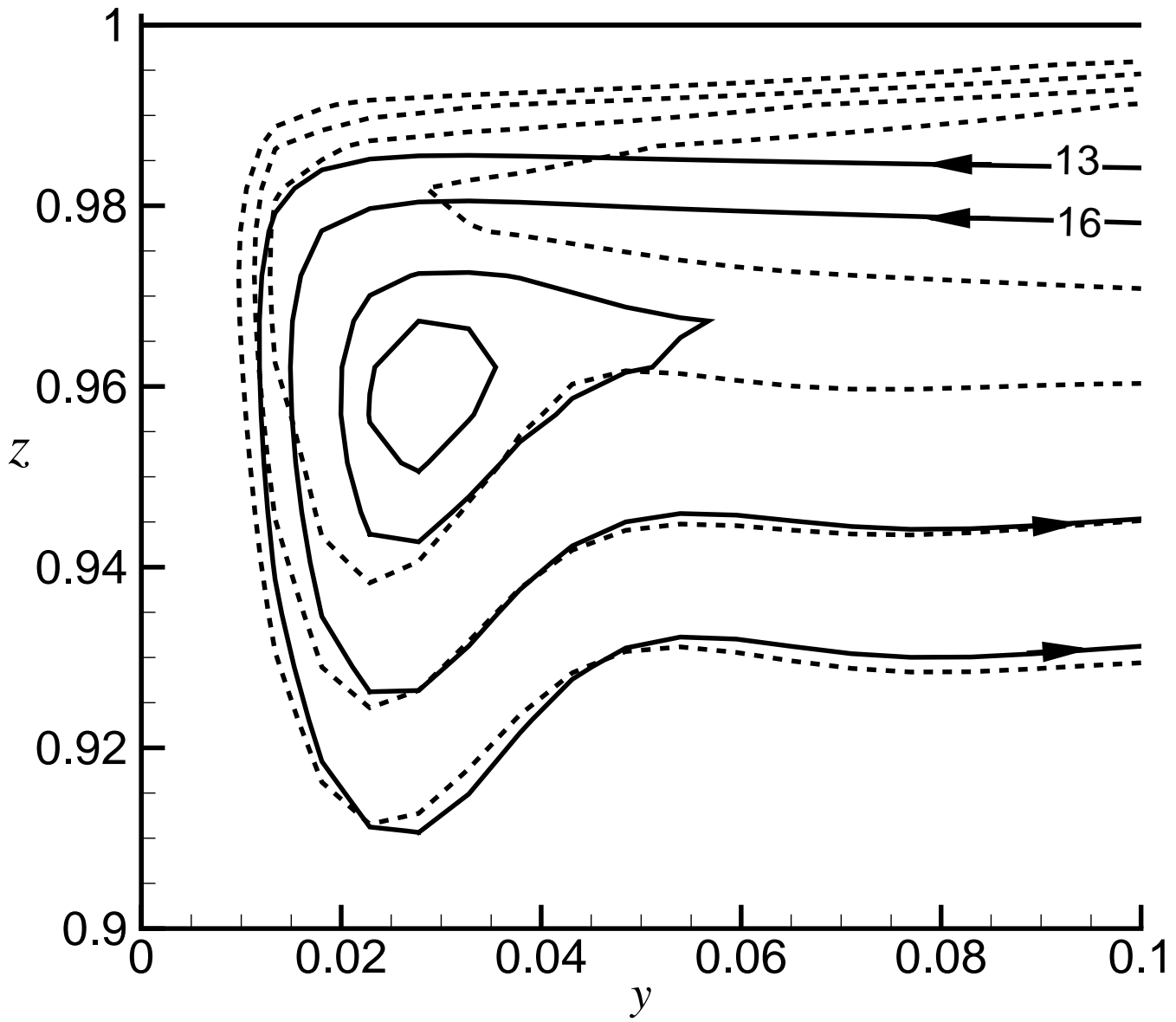




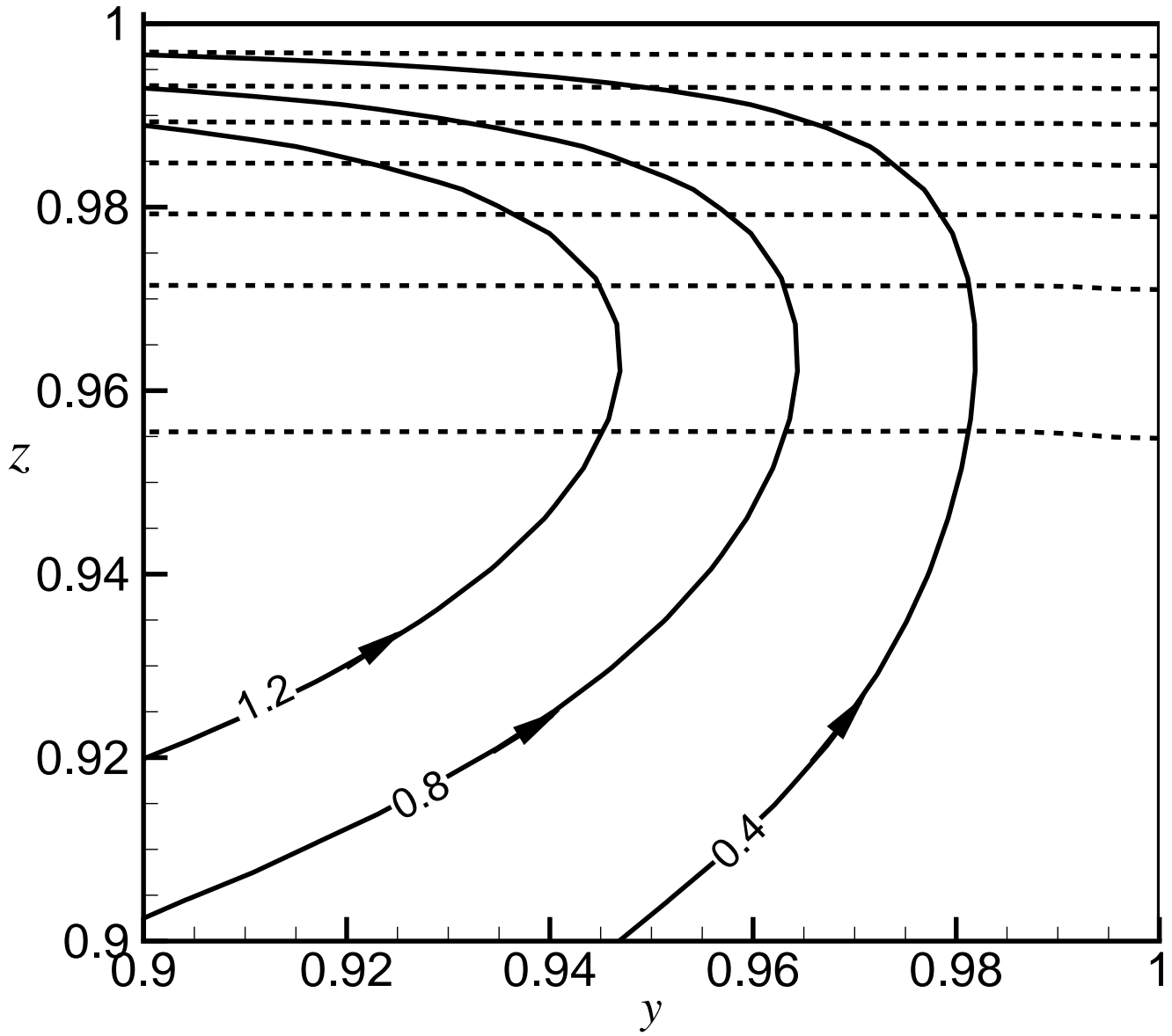
(b)



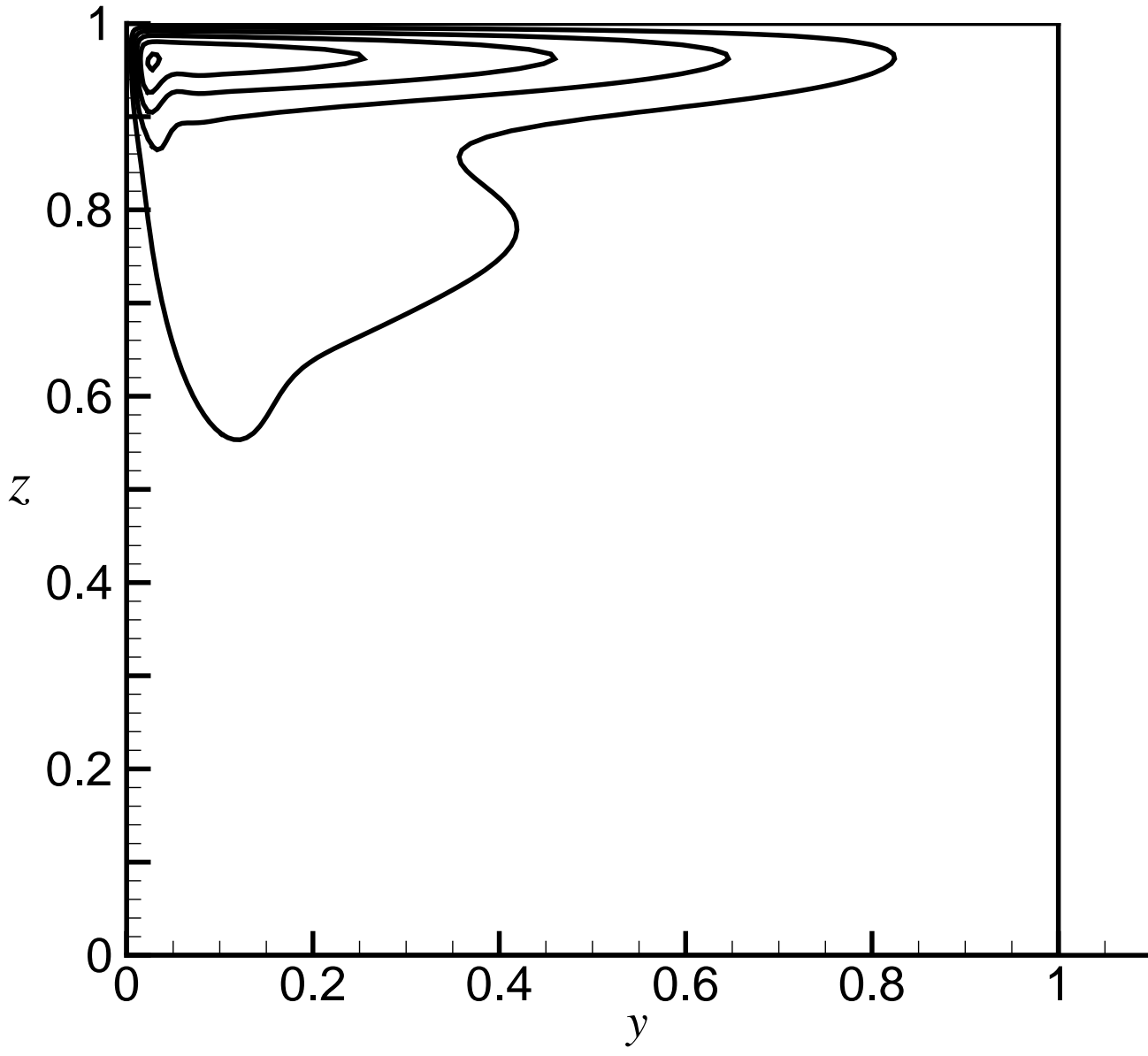
(a)



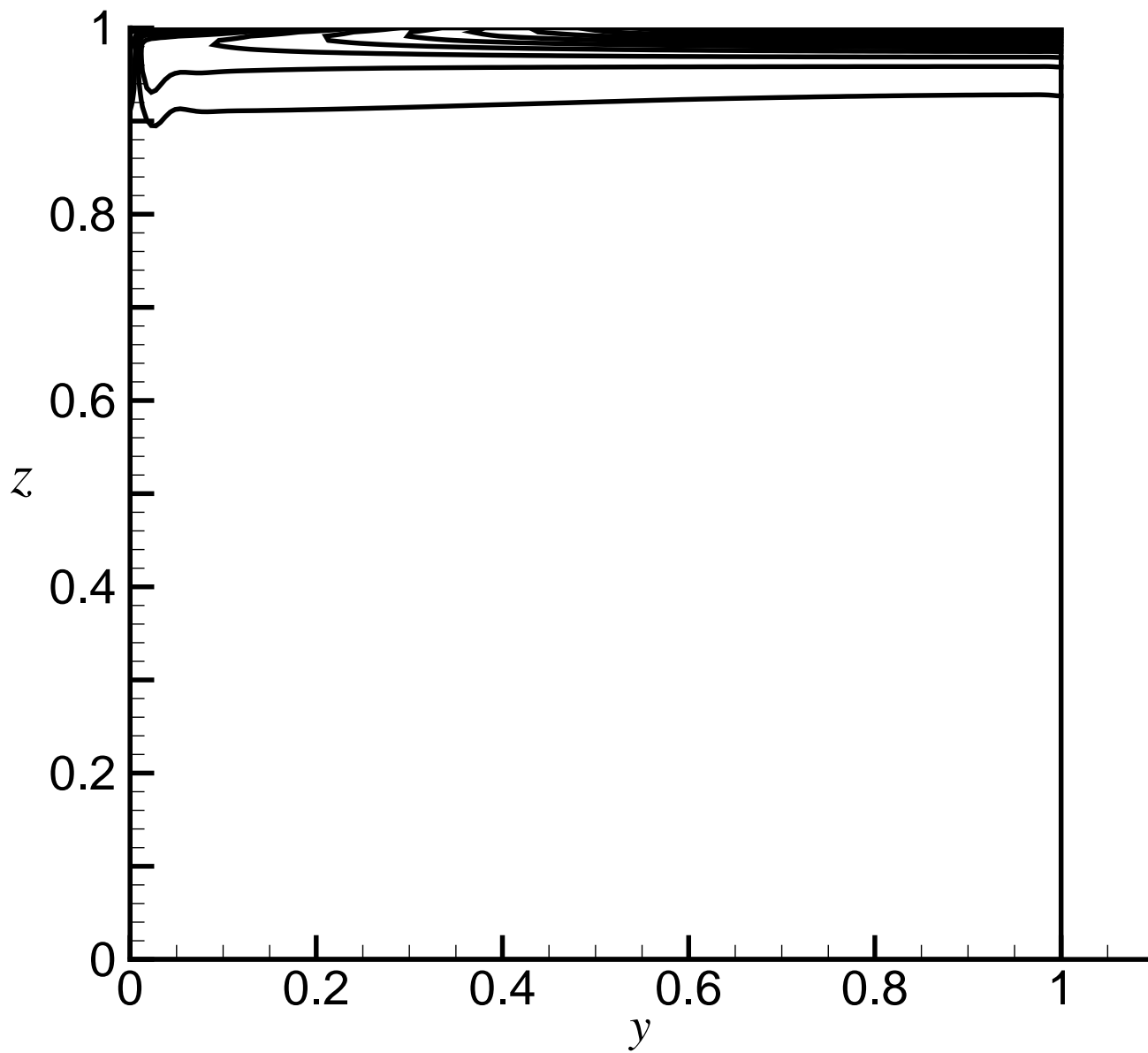
(b)

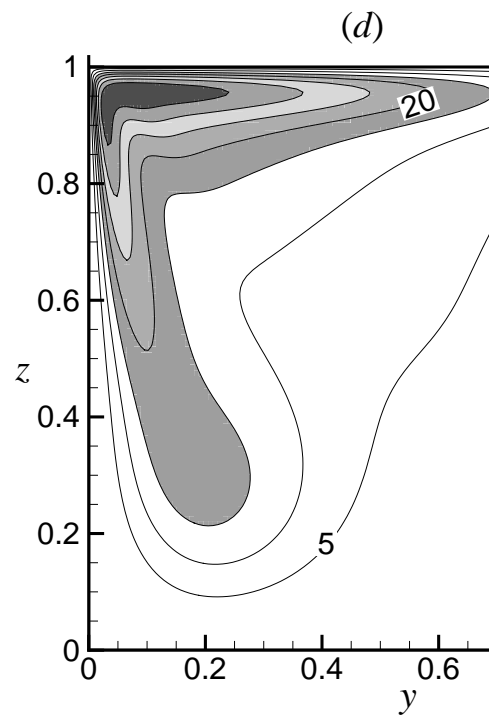
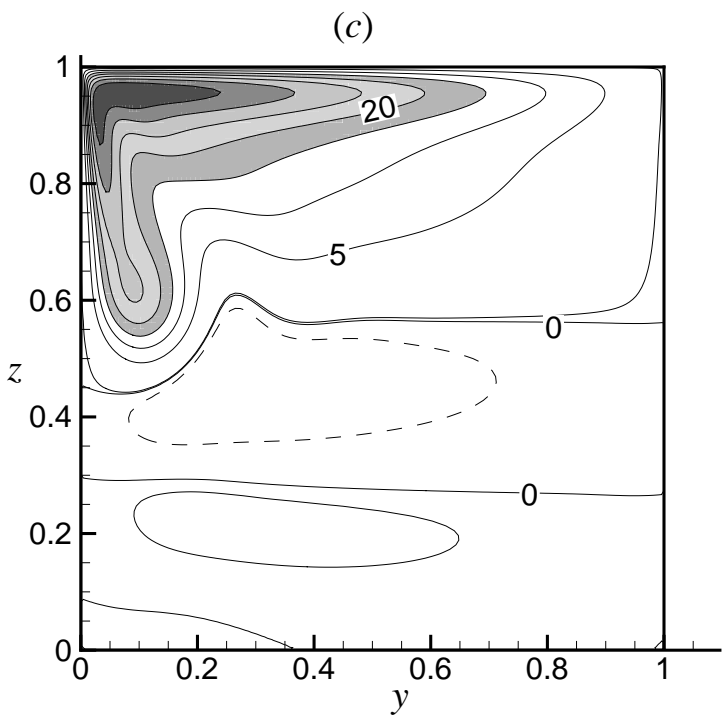
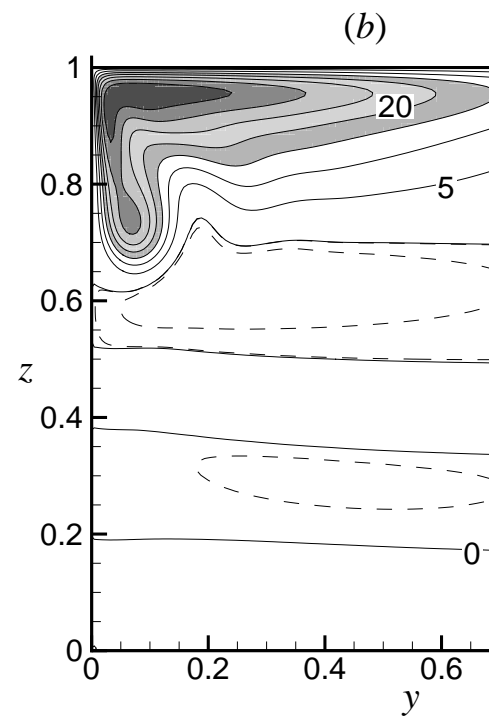
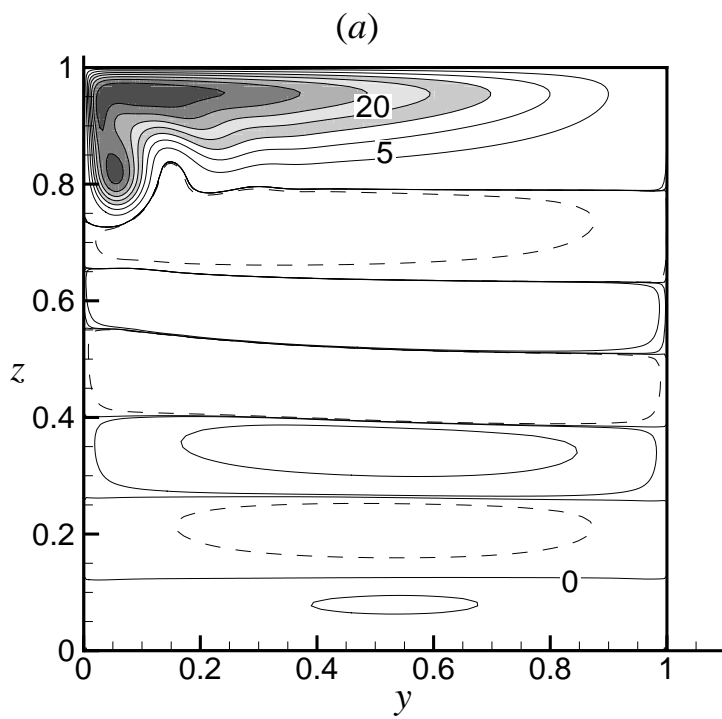


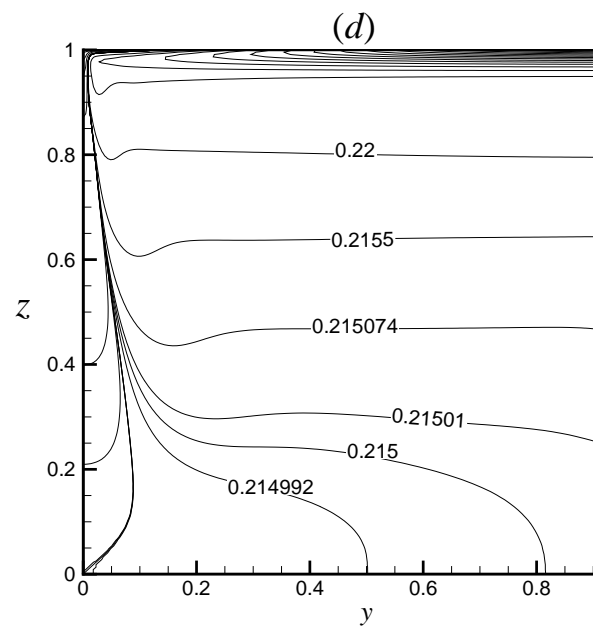
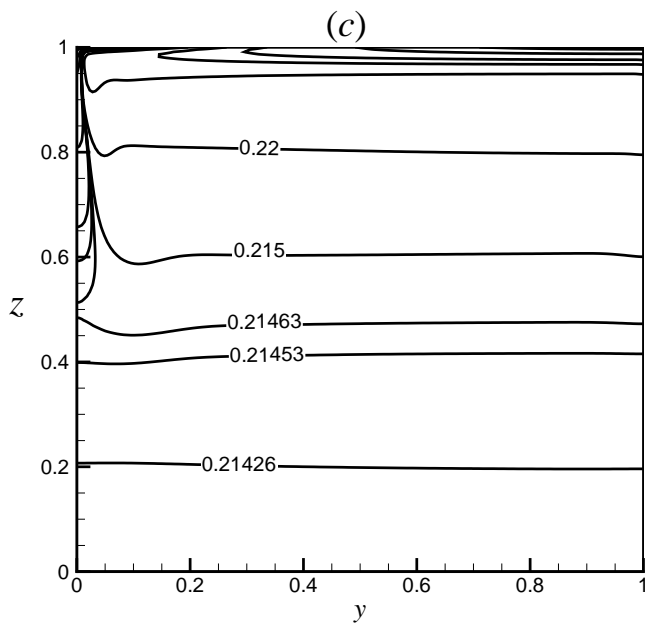
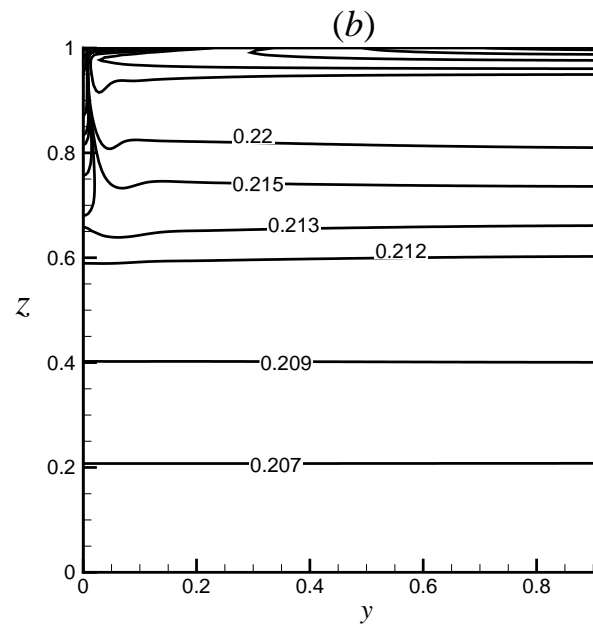
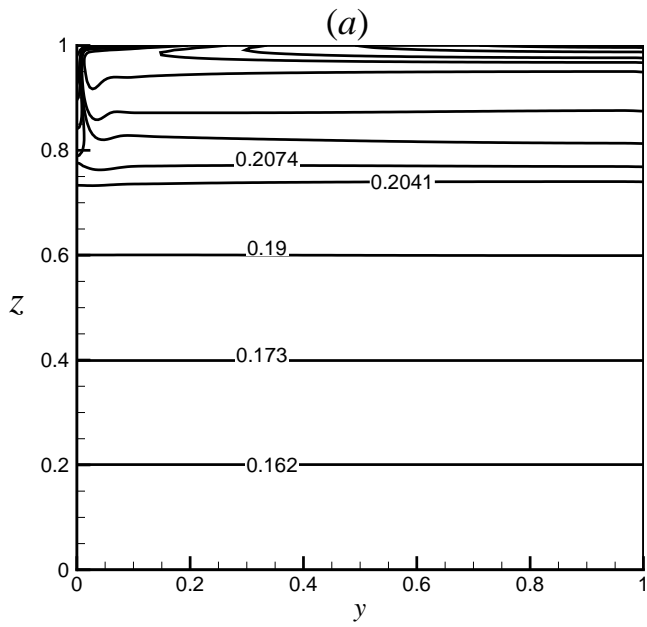
(a)

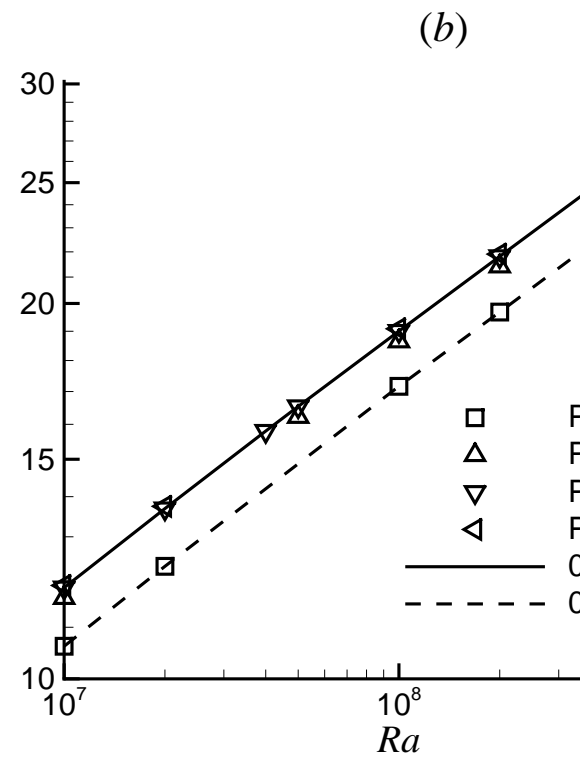
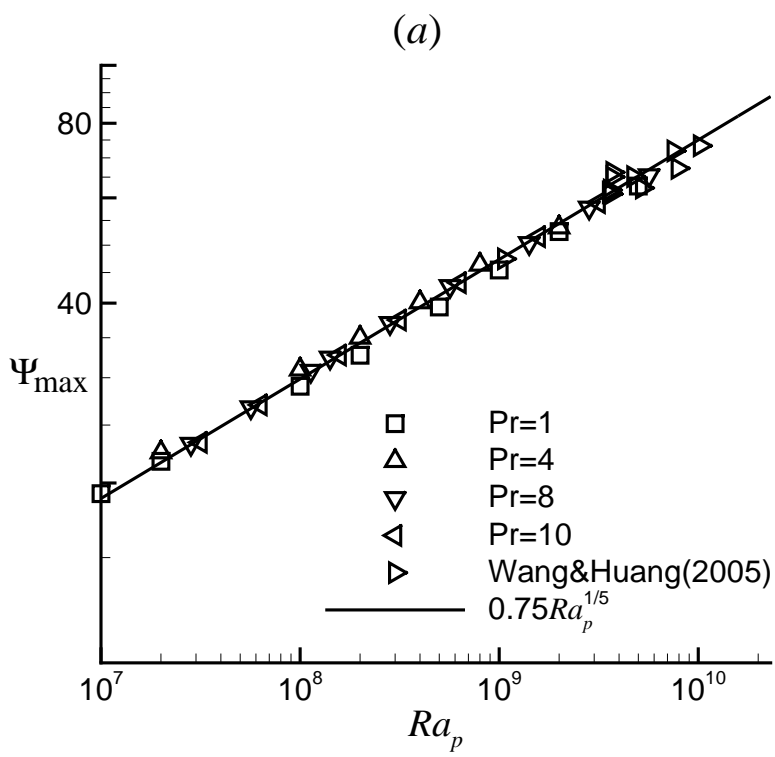


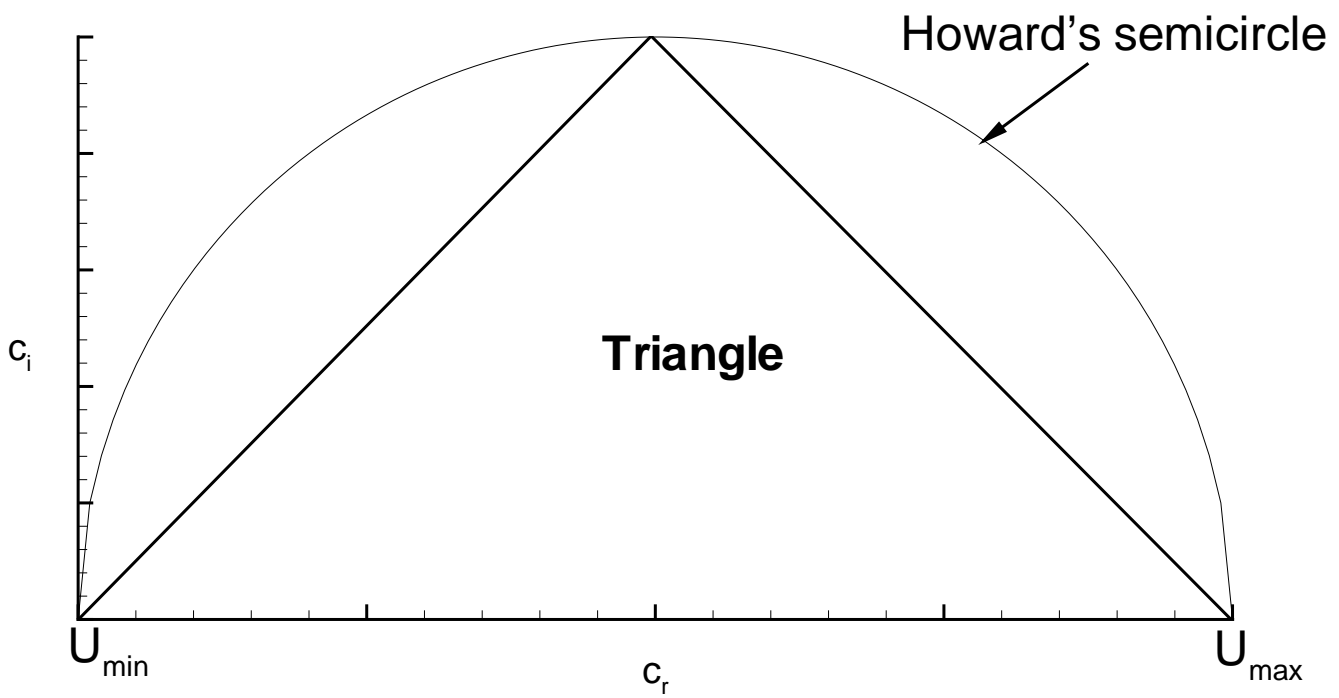
(b)

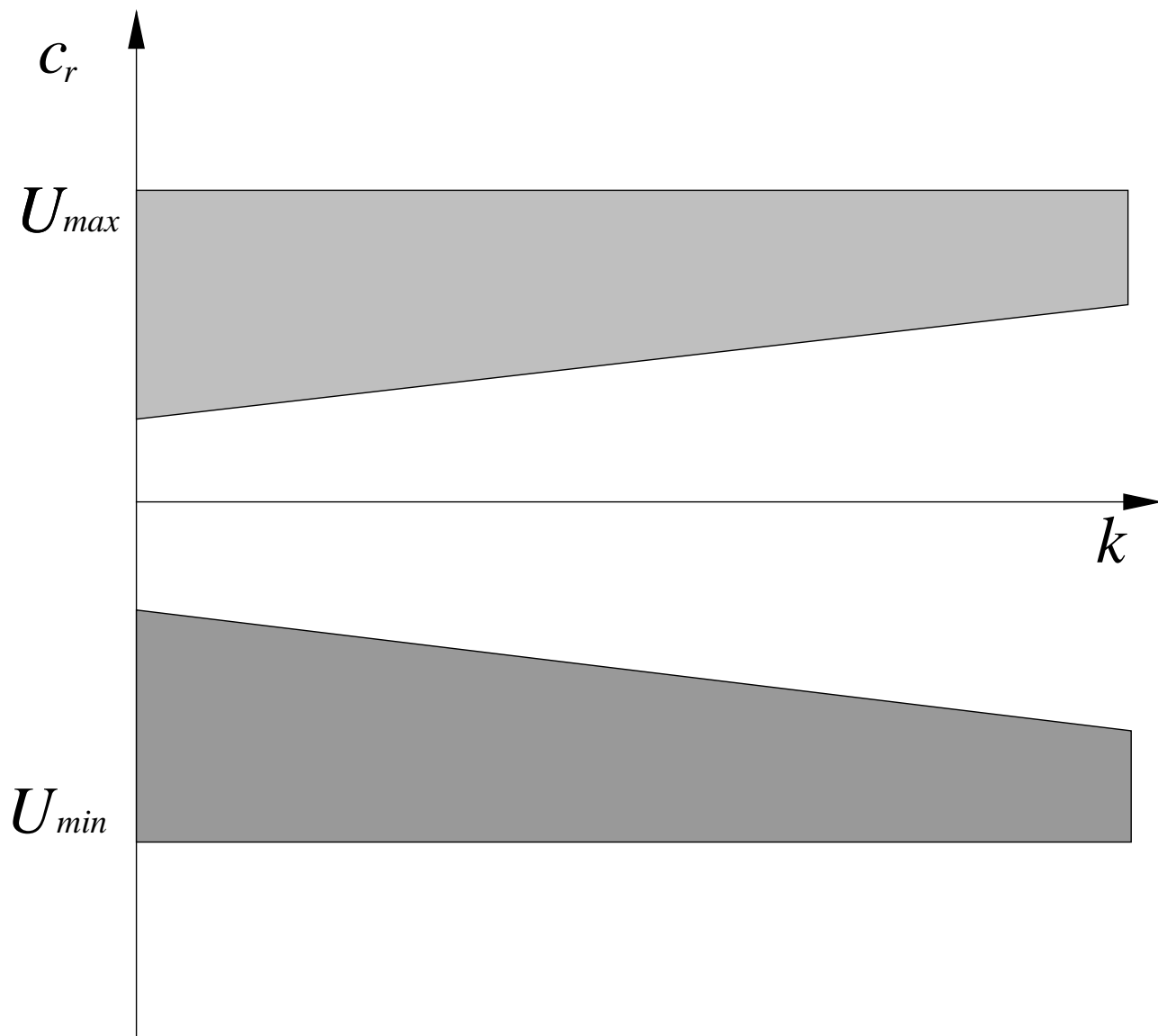




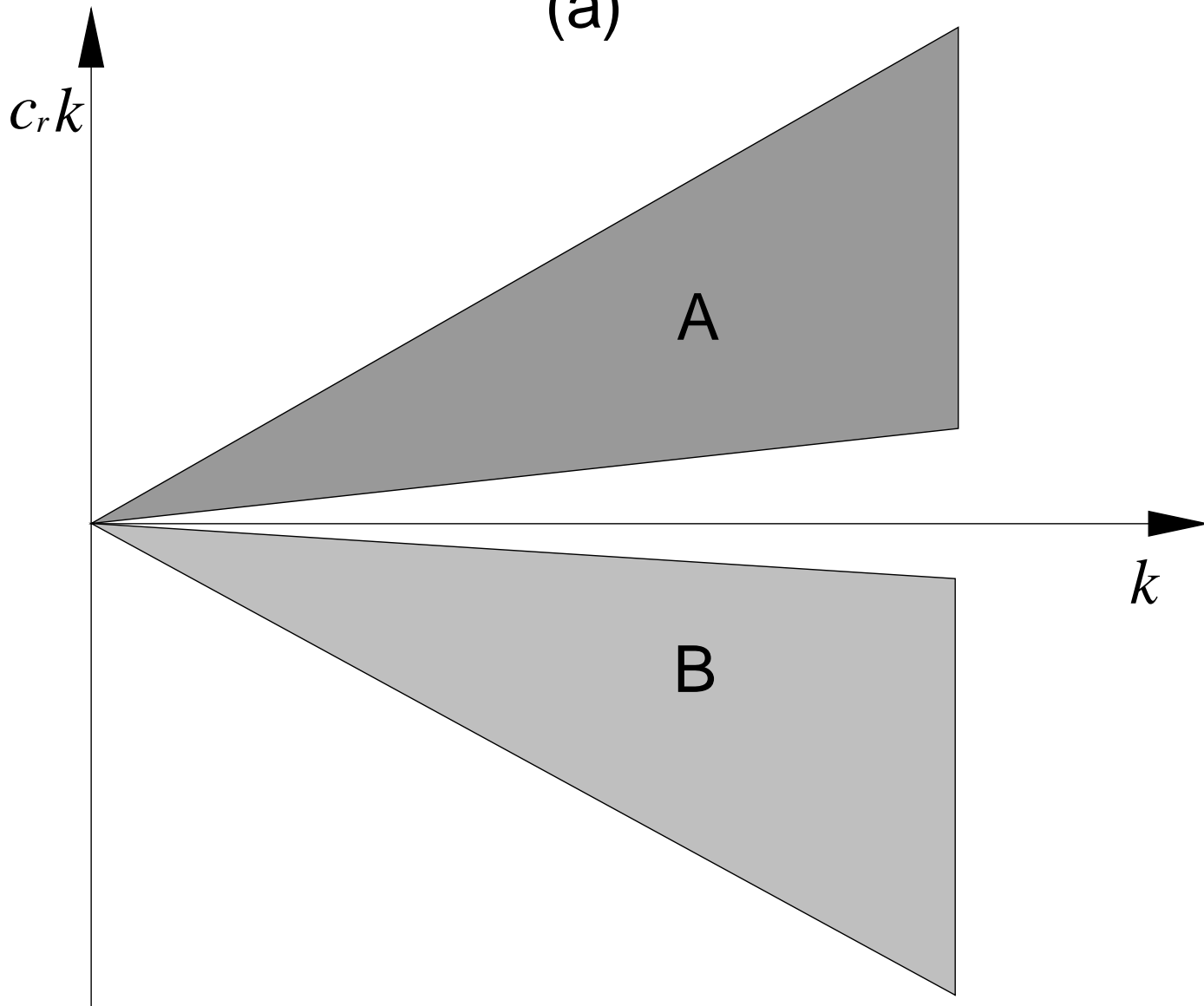








(a)



(b)

